Electrochemical Growth and Characterization of ZnO Nanowires

by

Lilei Hu

A thesis

presented to the University of Waterloo

in fulfillment of the

thesis requirement for the degree of

Master of Applied Science

in

Electrical and Computer Engineering

Waterloo, Ontario, Canada, 2014

© Lilei Hu 2014

AUTHOR'S DECLARATION

I thereby declare that I am the sole author of this thesis. This is a true copy of the thesis, including any required final revisions, as accepted by my examiners.

I understand that my thesis maybe made electronically available to the public.

____

Lilei Hu

ABSTRACT

ZnO semiconductor materials, especially nanostructured materials, have potential applications in large-area electronics, photonics and optoelectronics due to their unique electrical and optical properties. ZnO nanowires have advantages of high surface area to volume ratio, with the prospective for nanoscale control of doping the electrical properties for 1-D nanoelectronic devices. Many techniques have been tried to achieve high quality ZnO nanowires in large scale with low cost and simple fabrication. However, most of these techniques require high temperatures that exclude applications in flexible electronics. P-type conductivity is another impediment for fully realizing ZnO materials for electronic device application; and this limitation has prevented advances in optoelectronic and integrated circuit applications for ZnO.

To overcome the problems, this study investigated the synthesis and doping of ZnO nanowires at low temperature through a rapid electrochemical deposition growth technique. Material properties were studied using scanning electron microscopy (SEM), photoluminescence spectroscopy (PL), Raman spectroscopy, X-ray diffraction (XRD), ultraviolet to visible (UV-Vis) transmission spectroscopy, and electrical current-voltage measurements. ZnO nanowire doping was investigated using Al for n-type doping and for p-type doping, Ag/Al (co-doping) and Li. Al and Ag have significant influences on ZnO nanowire structures, while Li was found to improve the nanowire structure quality. The mechanisms for electrochemical deposition were studied through characterization of the chemical reactions, interface science and semiconductor/solution interface.

It was found that the low temperature grown nanowires had high oxygen vacancy condition induced donor defect states, while, incorporation of Li dopants contributed to trap states (deep acceptor states), rather than shallow acceptor states in the band gap. Shown by XRD and PL, oxygen assisted post-growth annealing was found to promote recrystallization of ZnO and elimination of oxygen vacancies for better crystal quality and photoluminescence emission. Cr, Al or Au metals were used as contacts to Li-doped ZnO nanowires to examine electrical properties of the doped nanowires, turning out high ideal factor were obtained because of the poor contact quality due to significant surface and interface states in ZnO nanowires. At last, mechanisms of surface states related tunneling current at the metal-semiconductor interface were discussed.

ACKNOWLEDGEMENTS

I would like to extend my appreciation to Professor Wong, for his support for this project and his guidance throughout the course of this research project. I am really grateful that he gave me the chance to start my study in the field of electrical engineering.

I would also like to extend my appreciation to other members in our research group past and present that have lent me their assistance and expertise: Dr. Czang-Ho Lee, Nicholas George Vardy, Minoli Pathirane, Bright Iheanacho, Alireza Tari, Melissa Chow, Maofeng Yang, Lina Voloshin and Dr. Nikolas Papadopoulos. I want to address my gratitude to Dr. Lee for his help with training me for using equipment, depositing contacts and seed layers, research discussion and revising this thesis, and to Nicholas George Vardy for his continuous help and suggestion for my courses, especially, in the beginning of this program.

I would like to thank Prof. Bo Cui and Prof. Irene Goldthorpe for reading this thesis and hope I have more opportunities to learn from them in the future.

I also want to thank Professor Zetian Mi and Dr. Qi Wang at McGill University for their assistance with photoluminescence characterization. Thanks Andrew for his help on making samples of Al/Ag co-doped of ZnO nanowires. I feel so lucky to have the chance to work at Giga-to-Nanoelectronics center with the other people: Richard Barber, Robert Mullins, Dr. Jian Zhang, Dr. Xiangcheng Sun, Bin Sun, Guocheng Liu, Qi Wang, Sibi Sutty, Ye Tian and Yoshitaka Kajiyama; thanks so much for your help and encouragement.

Finally, I would like to thank my family for all their love and support.

Table of Contents

AUTHOR'S DECLARATION i

ABSTRACT ii

ACKNOWLEDGEMENTS iv

Table of Contents v

List of Figures vii

List of Tables x

Chapter 1 Introduction 1

1.1. ZnO Semiconductor Nanomaterials 1

1.2. Scope of This Thesis 6

Chapter 2 Materials Fabrication and Characterization Techniques 7

2.1. Overview 7

2.2. Magnetron Sputtering Deposition System 7

2.3. Evaporation Deposition System 9

2.4. X-ray Diffraction 10

2.5. Raman Spectroscopy 11

2.6. Scanning Electron Microscopy 13

2.7. Photoluminescence Spectroscopy 15

Chapter 3 Electrochemical Deposition of ZnO Nanowires 21

3.1. Introduction to ZnO Nanowire Structures 21

3.2. Preliminary Research--Hydrothermal Growth 23

3.3. Electrochemical Deposition 28

3.3.1. Growth Parameters 28

3.3.2. Chemical Reactions and Mechanisms 29

3.3.2.1.Disadvantages of Hydrothermal Growth 29

3.3.2.2.Electrochemical Deposition Growth 30

3.3.3 Results of Electrochemical Deposition 36

3.4. Semiconductor/Solution Interface 38

3.4.1 Introduction to Helmholtz Layer 39

3.4.2. Substrate/Seed Layer Interface 41

3.4.3. Seed Layer/Solution Interface 42

3.5. Conclusions 45

Chapter 4 ZnO Nanowires Doping and Characterization 46

4.1. Introduction to Doping 46

4.2. Theory Overview of Doping 48
4.3. Experimental Discussion-Doping 51
4.3.1. Doping Conditions 51
4.3.2. Dopant Influences on The Nanowire Structure 52
4.4. Post-growth Annealing 56
4.4.1 Process Conditions 57
4.4.2 Characterization and Discussion 57
4.5. Photoluminescence of Li-doped ZnO nanowires 60
4.5.1. Emission Peaks 61
4.5.2. Band Energy Structure of Li-doped ZnO Nanowires 64
4.6. Electrical Characterization 65
4.6.1. Introduction to Contacts 66
4.6.2. Contact Fabrication Processes 68
4.6.3. I-V Characterization and Band Energy Structure 70
4.6.4. Model Fitting and Analysis 74
4.7. Conclusions 79
Chapter 5 Conclusions for Completed Studies 80
References 83

List of Figures

Figure 1.1 Histogram of the number of ZnO publication with the term “nanowires” and “nanostructures”……………………………………………………………….……………..…2

Figure 2.1 schematic representation of sputtering deposition, (a) without magnet and (b) magnetron sputtering with magnet……………………………………………….…….………….…8

Figure 2.2 schematic diagram of e-bema evaporation deposition…………………………….……...9

Figure 2.3 Schematic diagram of Bragg’s law……………………………………………….……11

Figure 2.4 a Raman transitional scheme, from left to right are Rayleigh scattering, stokes and anti-stokes, respectively……………………………………………………………………….13

Figure 2.5 Schematic diagram for interaction between electron beams with a sample…………14

Figure 2.6 Schematic diagram of curvature influences on topographical contrast. Red arrow represents escaped secondary electrons; tear drop shape is from the interaction between electrons and sample. Region (c) will be the brightest as more signals are collected by the detector…………………………....15

Figure 2.7 Energy level diagrams for fluorescence and phosphorescence…………...………….17

Figure 2.8 Energy diagram for emission under the presence of donor, acceptor and trap states..18

Figure 3.1 Schematic diagrams (a) of ZnO crystal structure. Yellow balls in the left diagram represent Zinc atoms and the grey balls stand for oxygen atoms. Diagram (b) shows different planes of ZnO crystal…………………………..……………………………………………22

Figure 3.2 a brief schematic diagram of equipment used for hydrothermal growth of ZnO nanowires……………..……………………………………………………………………….23

Figure 3.3 SEM images for ZnO nanowires grown at 80 ^{o}C (a) and 90 ^{o}C (b)………………….25

Figure 3.4 Density changes with the concentration of growth precursors……………………….26

Figure 3.5 Length and width (diameter) changes with growth time…………………………..….27

Figure 3.6 a schematic diagram of equipment used for electrochemical deposition of ZnO nanowires...……………………………………………………………………………………29

Figure 3.7 a schematic diagram for energy changes during electrochemical growth of Zn…..…35

Figure 3.8 SEM images of ZnO nanowires grown through electrochemical deposition method with potential -0.8 V……………………………………………………………………………..37

Figure 3.9 Diagram of growth rate of ZnO nanowires grown through electrochemical deposition method at different potential……………………………..…………………………………37

Figure 3.10 SEM images of ZnO nanowires grown through electrochemical deposition method with potential -1.2 V……………………………………………………….………………………37

Figure 3.11 an XRD diagram of ZnO nanowires grown through electrochemical deposition method with potential -0.9 V…………………………………………………………………38

Figure 3.12 a electronic scheme equal to electrochemical cell. R_s is substrate and solution interface caused resistance; R_{wire} is the resistance induced by connection wire; $R_{solution}$ is electrolyte solution resistance; C_d is the capacitance of double layer capacitor…………………40

Figure 3.13 General representation of the double layer formed at the ZnO-electrolyte interface……………………………………………………………………………………..40

Figure 3.14 energy band gap diagrams for p-type silicon and n-type thin film ZnO seed layer contact. (a) Before connecting and (b) after connecting……………………………...……42

Figure 3.15 the energy band gap diagram for an n-type semiconductor in contact with a solution…………………………………………………………………………………...43

Figure 3.16 energy band diagram for an n-type semiconductor in contact with a solution in the situation that (a) EF=EO/R and (b) EF>EO/R……………………………………………….……….………44

Figure 4.1 Schematic diagrams for the formation of ZnO hexagonal structure. Black ball represents electrons, grey ball the oxygen atom, yellow ball zinc atom…………………………….……………49

Figure 4.2.Real-space energy band diagram consisting the level of a donor electron. And the transition of electrons from donor level to the conduction band upon adding a small amount of energy……………………………………………………………………………………50

Figure 4.3.SEM images for (a) intrinsic ZnO nanowires, (b) 200 % Li doped, (c) 300 %Li doped, (d) 1 % Al doped, (e) 3 % Al doped, (f) 0.5 % Ag/Al co-doped, (g) 1 % Ag/Al co-doped, (h)3% Ag/Al co-doped ZnO nanowires…………………………………………………………... 55

Figure 4.4 X-ray diffraction diagrams for intrinsic and doped ZnO nanowires with Li, Al and Al/Ag, through hydrothermal (HT) or electrochemical deposition method (EC)……………….55

Figure 4.5 (a) Photoluminescence diagram for intrinsic ZnO nanowires with or without annealing processes at 500 °C for 30 minutes in the presence of O_2, measured at 300 K; (b) XRD diagram for intrinsic ZnO nanowires with or without annealing processes measured at room temperature…………...59

Figure 4.6 Raman diagram for intrinsic (a), 2 at % Al doped (b), and 200 at % Li doped ZnO nanowires before and after annealing……………...……………………………………………60

Figure 4.7 photoluminescence diagrams of Li doped and intrinsic ZnO nanowires measured at low and room temperature……………………………………………………………………………………63

Figure 4.8 photoluminescence diagrams for 200 % Li doped ZnO nanowires (a), and (b) is the magnification of (a) in the band edge emission region……………………………………..65

Figure 4.9 energy band diagram of Li doped ZnO nanowires. Arch figure represents the distribution of Li induced trap states; F_X is free exciton transition; D^OX is neutral donor-bound

exciton transition; F_A is free electron to acceptor (actually traps in this study) transition……………………………………………………………………………………65

Figure 4.10 a schematic diagram of metal/Li-doped ZnO nanowire contacts……………...……69

Figure 4.11 SEM images of the as-grown ZnO nanorods with the presence of electric field at an electrical potential of -0.8 V…………………………………………………………………..70

Figure 4.12 Current versus voltage diagram of contacts between Cr, Al and Au with Li-doped ZnO
nanowires……………..…………………………………………………………………72

Figurer 4.13 Schematic diagrams of energy band. Before contacting (a); (b) after contacting formed Al or Cr/Li-doped ZnO contacts, Possible Au/Li-doped ZnO contact diagram (c) and (d) formed when $\phi_M < \phi_S$ and $\phi_M > \phi_S$; (e) is Al, Cr or Au /Li-doped ZnO contact biased with electric field (metal is negative charged)…………………………………….....…………..………………………74

Figure 4.14 original and simulated I-V characteristics of Al (a), Cr (b) and Au (c)/Li-doped ZnO contacts…………………………..…………………………………………………...……77

Figure 4.15 a schematic diagram of possible tunneling conduction mechanisms responsible for Al and Cr/Li-doped ZnO contacts under low bias……………………………………………………………………………………………77

List of Tables

Table 3.1 E_{Θ} (V) and E (V) values for possible reductants…………………………………...33

Table 4.1 radius of different ions………………………………………………………….………..53

Table 4.2 fitting parameters for equations of temperature dependent band gap…………………61

Table 4.3 simulation parameters for I-V characteristics of different metal/Li-doped ZnO contacts…………………………………………………………………………………………...…77

Chapter 1

Introduction

1.1. ZnO Semiconductor Nanomaterials

Transparent thin-film materials have been widely used in various optoelectronic devices such as thin-film transistor, light-emitting devices, solar cells, and flat-panel displays due to their transparent properties in the visible and the near-infrared spectral region [1, 2]. Among them, transparent conducting oxide (TCO) thin films have attracted intensive attention for their excellent performances as electrodes in electronic devices, such as SnO_2 and In_2O_3 that have been used in industrial manufacturing. In 1980, metal-doped ZnO materials were first developed and, recently, have been regarded as alternatives to the ITO (Sn-doped In_2O_3), because of their high transparency in the visible region, high chemical stability and low resistivity. Some of the dopants for ZnO thin films are In (IZO), Ga (GZO), and Al (AZO) with high carrier densities of 10^{20}-10^{21} cm^{-3} and low electrical resistivity of 10^{-2}-10^{-4} Ω cm.

Zinc oxide has been prevalent in semiconductor research for more than 65 years since it was first mentioned in 1945 [3]. In the following 20 years from the 1950s to 1970s, ZnO was of interest in growth, and doping, however, this interest faded due to the difficulty of realizing n-type and p-type doping and attention altered to III-V class semiconductors [4]. In 2000s, the popularity of ZnO increased again for epitaxial layer growth, quantum wells, and nanostructures. As a widely investigated semiconductor material with a direct band gap of 3.37 eV in bulk and large exciton binding energy of 60 *meV* at room temperature [5, 6], ZnO has been reported to be used in many

applications in the field of electronic, optoelectronic, electrochemical, and electromechanical devices [7-12], solar cells [13-16], field emission devices [17-19], high-performance nanosensors [20-22], ultraviolet (UV) lasers [23, 24], light emitting diodes [25], piezoelectric nanogenerators [26-28], and nano-piezotronics [29-31]. Figure 1.1 shows a histogram plotted in 2012 that illustrates the number of ZnO nanostructure publications since 2000. In the mid 2000's, publications about ZnO nanowires have their highest increase, then the increase rate decreases due mostly to interests in other semiconductor nanomaterials such as carbon nanotubes and graphene [32-37], however, the popularity of ZnO nanostructure is still very high due to their vast amount of unique properties and potential applications. Attractive properties of ZnO include its ease of synthesizing crystalline material, the ability to obtain crystalline material on mismatched or amorphous substrate, and increased mechanical flexibility compared to the thin films, as well as capabilities of fabricating various nanoelectronics as 1-D nanomaterials.

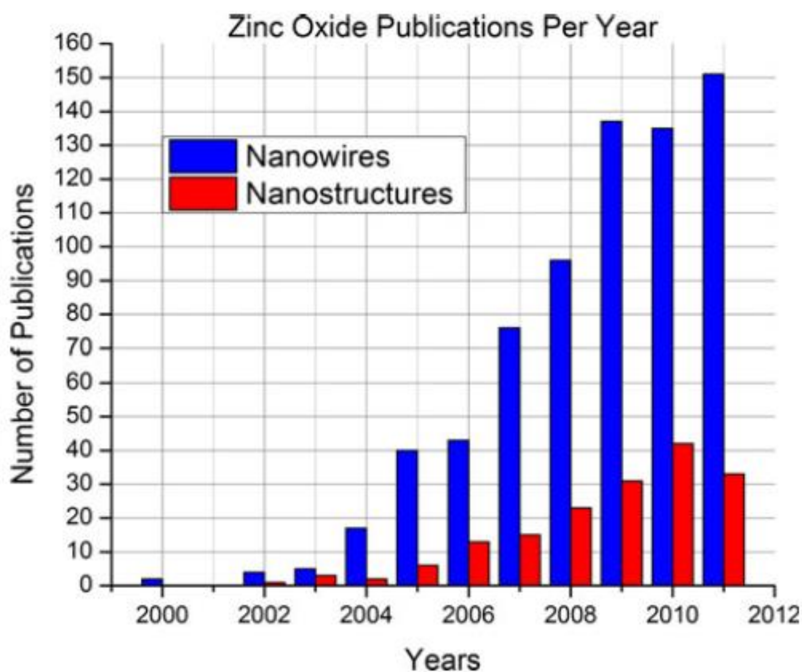

Figure 1.1 Histogram of the number of ZnO publication with the term "nanowires" and "nanostructures" [38].

Until now, various fabrication techniques have been developed to grow one-dimensioned ZnO nanomaterials, and those include wet chemical methods [39-41], molecular beam epitaxy (MBE) [42], sputtering [43], thermal decomposition methods [44], physical-vapor deposition [45-47], Metal-organic chemical vapor deposition (MOCVD) [48-50], Pulsed laser deposition [51, 52], Sputtering [53], Electrospinning [54-56], and even top-down approaches by etching [57]. These methods have their own advantages and disadvantages. Briefly speaking, pulsed laser deposition and top-down etching suffer from low productivity and controllability; Electrospinning will generate polycrystalline fibers instead of well aligned nanowires; physical-vapor deposition and flux methods have requirements such as high vacuum and high temperature, which lead to restrictions for flexible substrates so as for potential applications in foldable and wearable electronics, however, these methods typically result in the incorporation of impurities into the ZnO crystal during doping; MOCVD and MBE are the best techniques to fabricate high quality ZnO nanowire arrays, but they usually result in bad deposition uniformity, low product yields and high experimental cost, as well as limitations in substrate choice, therefore, they are less widely acceptable; In comparison, wet chemical methods at low temperature are more attractive. Firstly, potential substrates for wet chemical deposition of ZnO nanowires can be flexible organic substrates; secondly, they are always low-cost, less hazardous, and thus capable of easy scaling [58-59]. In addition, there is no needs for pre-coating metal crystals, thus it can be integrated with well-developed silicon technologies [60]. Furthermore, many adjustable parameters of these growth methods enable them to realize different desired ZnO nanostructures, and parameters such as the growth temperature, concentration of the growth precursors and the pH of the growth bath [61-62].

Although large-scale, dense, well oriented and homogeneous ZnO can be grown on arbitrary substrates through wet chemical methods. The growth rate is limited to several hundred nanometers per hour, which is quite low [63-65]. Furthermore, high nucleation density is not possible without a pre-coated seed layer on polished substrates [66]. To increase nucleation density, seed layers are generally used in the growth processes, however, seed layers will form interfaces between nanowires and substrate, and this leads to poor electrical properties, low thermal and electron transport, and significant light scattering in electronic devices. Although long nanowire length can be achieved through extending growth time, (001) planes were found to be etched and form ZnO nanotube structure if nanowires were exposed for too long time to a growth-solution bath [67]. Solving this problem, a negative electrical potential was reportedly applied in aqueous growth solution to get high growth rates and nucleation densities [68]. Compared with other techniques for ZnO fabrication, using strong external electric field as a driving force of the reaction, electrochemical deposition is a powerful technique to fabricate uniform and lager-area ZnO nanostructures [69]. For this method, growth can occur on a variety of substrates [70] as long as the substrate is conductive. The mechanical flexibility capability of this electrochemical deposition method is especially important for flexible electronics such as flexible LED and displays. The market for flexible, printed, and organic large-area electronics is rapidly growing, and for flexible electronics they have the properties of being lightweight, rugged, bendable, portable and potentially foldable. Electrochemical deposition, however, is able to grow nanowires on various flexible substrates to obtain all these properties of flexible electronics. In addition, in references [71] and this study, better nanowire alignment and stronger adhesion to the substrate has been observed. In this technique, ZnO nanowires can only be grown when the substrates are cathode materials biased with a DC power source [72]. Furthermore,

electrochemical deposition was found to be helpful in doping nanowires through simply adding dopants to the growth bath [73-75]. In comparison with other electrochemical deposition techniques, the equipment used is much simpler and lower cost, so as the the ease of processing. Generally, the deposition of ZnO is processed by reduction of an oxygen precursor including chloride, hydrogen peroxide, and nitrate and dissolved O_2. Therefore, for most electrochemical deposition, the bubbles of O_2 were required. The absence of bubbling oxygen and aqueous growth bath simplified fabrication processes in this study, however, well-aligned, well nanowire structure-defined, and dense nanowires with high length to diameter ratio were able to be grown at low temperature and high growth rate.

ZnO nanostructure can also be manipulated into different morphologies for various applications. These nanostructures include nano thin film, nanowires, nanobelts, nanotubes, nanorings, twinning structures, hierarchical structures, and many heterostructures with other materials. It is quite impressive that wet chemical methods can achieve all these nanostructure morphologies. Nanobelts can be grown in bulk solution or on a substrate in synthesis process [76-78]. Nanotubes and nanorings attract intensive attention as their good performances in applications of high-efficiency solar cells due to its high internal surface area compared with other structures, and in biomedical field, as well as gas sensors [79-84]. Reports of twinned structures can be found in references 85-89. In twinned ZnO structure, two joined hexagonal prisms are connected by a common basal plane generating a twinning growth relationship. By adding polymers such as poly (sodium 4 styrenesulfonate) (PSS), different hierarchical structures of ZnO can be obtained [90-91]. To extend functions of ZnO nanostructures, many different materials have been incorporated into ZnO nanomaterials to form heterostructures. For example, to passivate surface

dangling bonds of ZnO nanowires, different compound semiconductors, including CdSe [92-93], CdTe [94] by electrodeposition, CdS [95], SnO2 [96] and MgO [97, 98] through hydrothermal reaction, CoO4 [99] by photochemical reaction, ZnS [100,101] by sulfidation, and Al_2O_3 and TiO_2 by atomic layer deposition (ALD). In most cases, the as-formed shell layers are polycrystalline or amorphous in nature.

1.2. Scope of This Thesis

This thesis discusses ZnO nanowires from growth techniques, doping, and characterizations to their applications. The literature review in chapter 1 provides background to the properties of the ZnO semiconductor, its fabrication techniques and applications. Chapter 2 discusses basic principles of the main fabrication and characterization technologies used in this project. Chapter 3 focuses on the electrochemical deposition method, discussing growth mechanisms of the ZnO nanowires and a preliminary study of substrate/solution interface. Chapter 4 presents findings from studies of doping ZnO nanowires, including ZnO nanowire structure, energy band structure; defect states, post-growth annealing effects and electrical properties of Li doped ZnO nanowires. In Chapter 5, a conclusion of this project was made

Chapter 2

Material Fabrication and Characterization Techniques

2.1. Overview

In this section, the magnetron sputtering deposition system for depositing the growth seed layers, evaporation deposition for contact fabrication, and characterization techniques including scanning electron microscopy (SEM), X-ray diffraction (XRD), Raman spectroscopy and photoluminescence spectroscopy (PL), are introduced.

2.2. Magnetron Sputtering Deposition System

In this study, the magnetron sputter system was used for thin film deposition of Al doped ZnO (AZO), ZnO, Cr and Al. Therefore, this subsection will present an introduction to magnetron sputtering deposition technique.

In sputtering deposition system, gas ions (Argon, typically) are generated in a plasma and accelerated to collide with the target to remove atoms from target materials, which process is called sputtering. A substrate will be in the vicinity of the target and sputtered atoms will deposit on the substrate. Gas pressure is generally maintained at 3 – 50 mTorr (5 mTorr for ZnO deposition in this study) to ignite the plasma. In a DC-sputtering system, the target is negatively charged up to several hundred volts to accelerate positively charged ions to the target. Interactions between ions and target also create secondary electrons that cause further ionization of the gas. In the magnetron sputtering system, a ring of magnets is placed below the target to trap and circulate secondary electrons over the target. The application of the magnetic ring can significantly increase gas ionization rate and, therefore, the deposition rate. DC sputtering is used

whenever the target material is conductive. When materials are not conducive, bombardment of positive ions will soon build up on the target surface and repel further incoming ions, which results in the quenching of the ion current. Thus, RF-magnetron sputtering is used for insulating targets such as ZnO. Figure 2.1 shows schematic diagrams for sputtering deposition without (a) and with (b) a magnet. In magnetron sputtering the secondary electrons are confined in a region close to the target, and engage in collisions with gas atoms, which result in a very dense plasma in the ring-shaped drift path. The electric field as discussed before can be generated by either in DC or RF mode. Ions created in the drift region have a high probability of hitting the target. In addition, this drift region will contribute more secondary electrons hence create an extremely dense plasma. With the magnetron configuration, deposition rates can be up to 10 to 100 times higher than that without magnetron configuration, in addition, low pressure operation (0.5-30 mTorr) and lower voltage (300-700 V for DC and <500 V amplitude for RF) are possible.

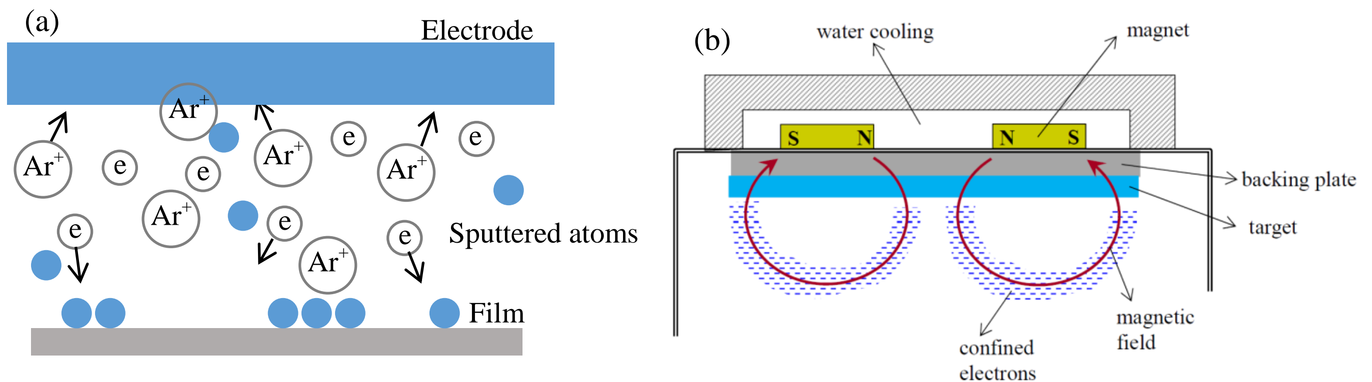

Figure 2.1 schematic representation of sputtering deposition, (a) without magnet and (b) magnetron sputtering with magnet. [102]

2.3. Evaporation Deposition System

An evaporation process is mainly used for deposition of thin metal films. The process is carried out in a vacuum chamber at the pressure well below 1 Torr. A target is placed in a crucible and heated by inductive coil (thermal evaporation) or by electron beams (e-beam evaporation). During the evaporation process, there is an equilibrium vapor pressure which depends on the temperature. With high equilibrium evaporation, a high deposition rate can be achieved. Common thin films deposited by evaporation include, for example, Al, Ag, Au, Ni, Cr, Pt, Ti, Ta_2O_5, TiO_2, ZnS and MgF_2. Figure 2.2 shows a schematic diagram for e-beam evaporation deposition system, in which the electron gun with a tungsten (W) gun filament is located below the crucible to avoid contamination of the source. Magnetic field is used to bent electron beam by about 270 ^{o} and manipulates the e-beam to precisely hit the surface of the target and melt a fraction of it. Material will evaporate and deposit onto the substrate.

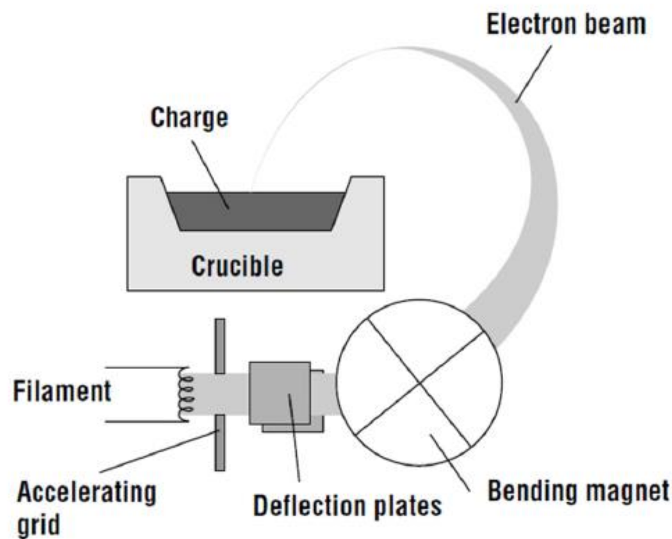

Figure 2.2 schematic diagram of e-bema evaporation deposition system [102].

2.4. X-ray Diffraction

X-ray diffraction is a widely used characterization tool for analyzing the materials structure. Generally, information including sample composition, phase, particle size and strain can be obtained from typical intensity versus 2θ. When the X-ray beam is directed onto the sample, as illustrated in Fig. 2.3, the incident X-ray beam 1 is scattered by atoms in the upper atomic plane and X-ray beam 2 is scattered by atoms in the lower atom plane of the sample. The distance between the two planes is d_{hkl}. As calculated, the path difference between two X-ray beams is $2d_{hkl} \sin\theta$, if constructive interference between diffracted occurs, a peak appears as in the typical XRD diagram. Equation (1) is the Bragg condition for x-ray diffraction:

$$2d_{hkl}\sin\theta = \lambda \quad (1)$$

Where h, k and l are the Miller indices for the planes reflecting the x-ray beam. Particle or grain size can be calculated from the application of Scherrer equation as shown below in equation (2),

$$D = \frac{0.9\lambda}{B\cos\theta} \quad (2)$$

Where D is the mean size of ordered (crystalline) domains; 0.9 is a constant for a spherical crystal particle in cubic system. λ is the wavelength of X-ray; B is the broadening width from sample characteristics determined by crystallite size, but influenced by crystal imperfections such as lattice strain, defects, and θ is the measured peak position. B can be calculated by the following equation (3):

$$B = B_{obs.} - B_{std.} \quad (3)$$

Where $B_{obs.}$ is the full width at half maximum (FWHM) of the measured peaks, and $B_{std.}$ is the broadening caused by instrument such as beam divergence, and it is different from each

equipment due to different targets. Scherrer equation is accurate when the particle size is less than 100 nm.

Therefore, from peak position we can calculate the d-spacing of atom planes as well as the lattice parameters. The peak width and peak shape can provide information about crystallite size, strains and defects.

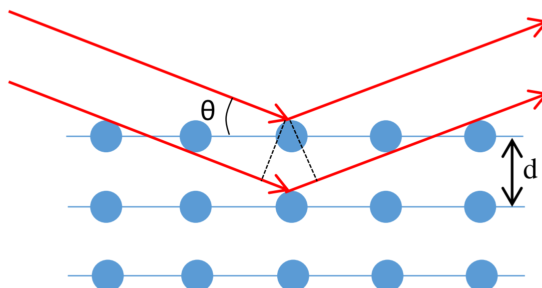

Figure 2.3 Schematic diagram of Bragg's law.

2.5. Raman Spectroscopy

Raman spectroscopy is used to determine molecular motions, especially vibrations due to chemical bonds. In this study, Raman spectroscopy was used to verify chemical bond changes before and after post-growth annealing of Li doped ZnO nanowires. Raman spectroscopy is based on inelastic scattering, i.e. frequency of photons from monochromatic light changes upon interacting with a sample. Photons from a laser source will be absorbed by samples then reemitted. The reemitted photons have a frequency shifted up and down compared with the original monochromatic frequency, and this shift is referred to as the Raman effect. Raman shifts provide information about vibrational, rotational and other low frequency transitions in molecules.

Raman Effects are caused by molecular deformation in electric field *E* determined by molecular polarization. Incoming laser beams can be considered as an oscillating electromagnetic wave with electrical vector *E*, which induces electric dipole moments so as to deform molecules when the light interacts with the sample. Because of the deformation, molecules will start to vibrate with a characteristic frequency, ν_m. Therefore, the incoming laser beam with frequency ν_0 will excite molecules and transforms them into oscillating dipoles. Such oscillating dipoles will emit light of three different frequencies as depicted in Fig. 2.4. Firstly, the molecule with no Raman-active modes absorbs photons with the frequency ν_0, when this molecule returns back to the original vibrational state, it will emit the photon with the same frequency ν_0 as the excitation source. This type of interaction is called elastic Rayleigh scattering. Secondly, if a photon with frequency ν_0 is interacting with a Raman-active molecule, at which time the molecule is at the basic vibrational state. The photon transfer part of its energy to the molecules to have vibration frequency ν_m, and the resulting scattered photon will have frequency reduced to ν_0- ν_m. This Raman frequency is called the Stokes frequency. Thirdly, a photon interacts with a Raman-active molecule, at this moment, the molecules have already been at the excited vibrational state. Excessive energy of the excited Raman-active molecule will be released and the molecule goes back to the basic vibrational state and the resulting frequency of scattered light goes up to ν_0+ ν_m. This Raman frequency is called Anti-Stokes frequency.

About 99.999% of all incident photons in spontaneous Raman undergo elastic Rayleigh scattering, which is not useful for identifying molecules in Raman spectroscopy. Therefore, only 0.001% of the incident light produces inelastic Raman signal with information of the molecular structure. In addition, spontaneous scattering is very weak and special measures should be taken to distinguish it from the predominant Rayleigh scattering. Instruments such as notch filters,

tunable filters, laser stop apertures, double and triple spectrometric systems are used to reduce Rayleigh scattering and obtain a high-quality Raman spectra.

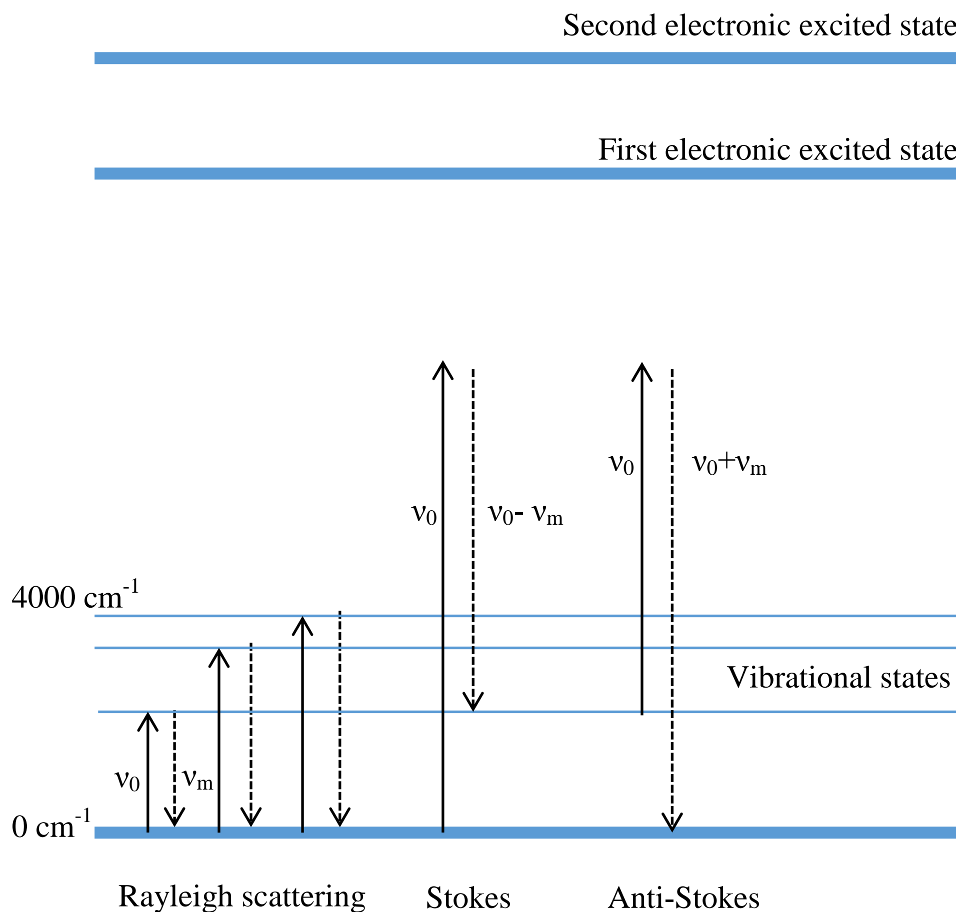

Figure 2.4 a Raman transitional scheme, from left to right, they are Rayleigh scattering, stokes and anti-stokes, respectively.

2.6. Scanning Electron Microscopy

Scanning electron microscopy (SEM) is widely used for characterizing morphology of and topography of samples in the field of materials science, biological science, chemistry and physics. Compared with optical microscopy, electrons used in SEM have much shorter wavelength. Electrons are accelerated through a potential drop V in a high vacuum tube and that gives

electrons kinetic energy equal to eV. Generally, electrons are accelerated at voltages from approximately 1 to 15 kV. In this study of characterizing ZnO nanowires, an applied voltage is 5 or 10 kV depending on the substrate used

After going through lenses, electrons will interact with the sample; Fig. 2.5 shows the interactions between electrons and the sample. The SEM collects secondary electrons to characterize sample topography and morphology.

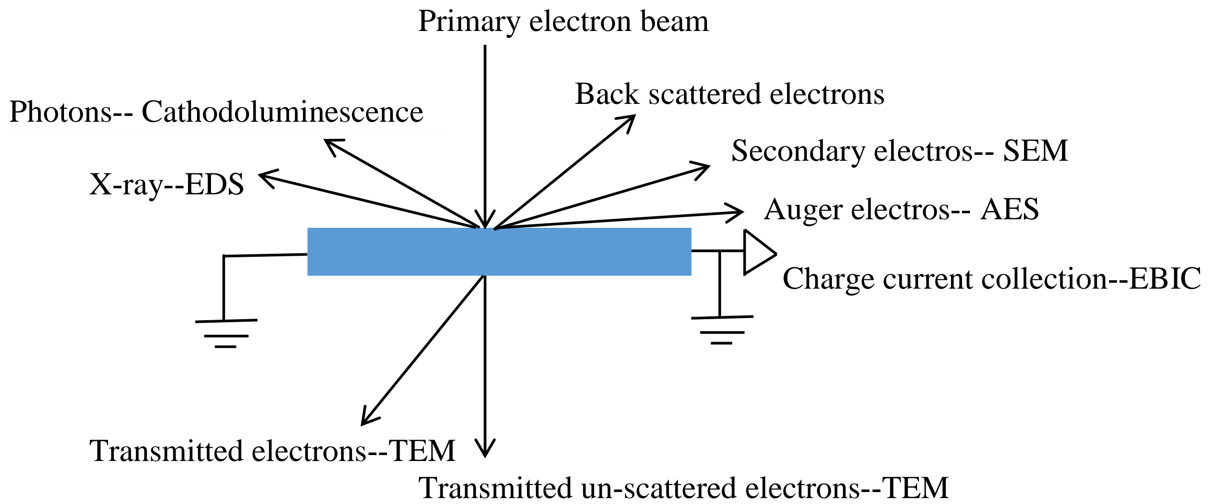

Figure 2.5 Schematic diagram for interaction between electron beams with a sample.

During the interaction between primary electrons and sample, secondary electrons will be generated on the surface about 5 to 10 nm at low energy, and deeper secondary electrons generated are not able to escape from the sample. They are the most used signal in the SEM since they originate from a small volume so as to achieve high resolution.

Topographical contrast is a very important aspect to get high-quality SEM images. Generally, the more secondary electrons the detector can collect the clearer the images will be. Local curvature

will affect how many secondary electrons can escape and its orientation with respect to the detector is also an influence, as shown in figure 2.6. Secondary electrons from region (a) and (b) can be partly blocked by bumps in the sample. For (c), signals generated in deeper region can also survive at the corner region, thus (c) is the brightest part is the SEM images followed by (d).

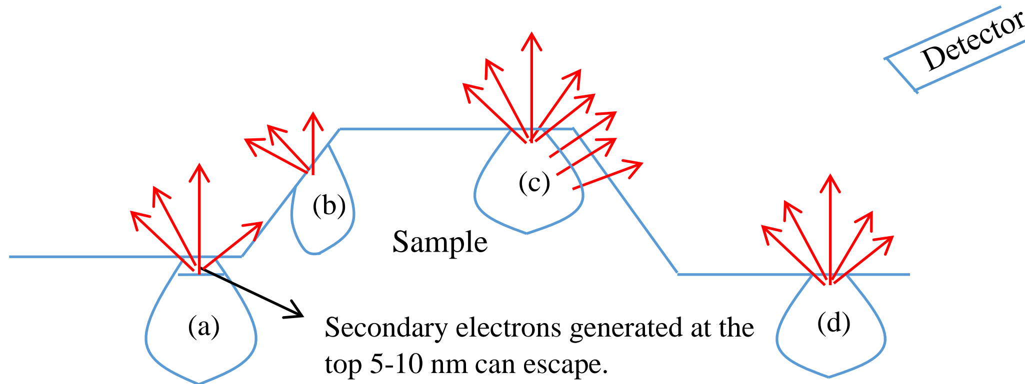

Figure 2.6 Schematic diagram of curvature influences on topographical contrast. Red arrow represents escaped secondary electrons; tear drop shape is from the interaction between electrons and sample. Region (c) will be the brightest as more signals are collected by the detector.

In this project, when glass or plastic substrates were used, they are not conductive, so electrons will be accumulated on sample surface making the sample negatively charged. Negative charged sample surface will repel incoming electron beams which results in shift caused image distortion. Generally, a gold coating or conductive paint is applied to remove this problem.

2.7. Photoluminescence Spectroscopy

Photoluminescence (PL) is the spontaneous emission of light from a sample under optical excitation. PL spectroscopy is widely used to study electrical properties of materials and very

sensitive to discrete electronic states. From the emission spectrum, information about surface, interface, impurity levels, alloy disorder and interface roughness can be obtained. The intensity of the PL peaks is able to provide information related to the surface and interface quality. PL spectroscopy is a nondestructive characterization method requiring minimal manipulation or environmental control. However, the limitation of the PL analysis is its high requirements for irradiative efficiency, for example, which is enhanced in direct band gap semiconductor. In this study, ZnO is a direct band gap so as it has high efficiency of luminescence.

PL spectroscopy measures emitted photons. There are three types of luminescence: Cathodoluminescence using cathode rays; photoluminescence through photon excitation; and electroluminescence by electrical injection. Figure 2.7 shows the interaction between photons with energy larger than the semiconductor band gap E_g. Electrons in the valence band at singlet ground states are excited by absorbing energy from incident photons to the excited singlet excited band in the conduction band. If photon energy is smaller than semiconductor band gap then this semiconductor material is transparent to these photons. In the conduction band, excited electrons with energy higher than the bottom energy level of the conduction band will relax through releasing energy to the lattice by vibration relaxation such as scattering. This process is nonradiative relaxation. Meeting required conditions, electrons may transfer to states with lower energy through internal conversion. These electrons will relax to the bottom of the conduction band and go back to combine with holes in the valence band by emitting photons. This photon emission process is so called fluorescence. Or electrons will fall back to valence band through nonradiative internal and external conversions. It is also possible for electrons in excited singlet states to transfer to triplet excited states through intersystem crossing. After relaxation through

lattice vibration, electrons go to the bottom of triplet state band, and can recombine with holes in the valence band meanwhile emission of photons will occur and this process is called phosphorescence. Similarly, through internal and external conversion, nonradiative combinations are possible. For fluorescence emission, emission lasts for 10^{-8} s after turning off the excitation, and several seconds or even minutes for phosphorescence.

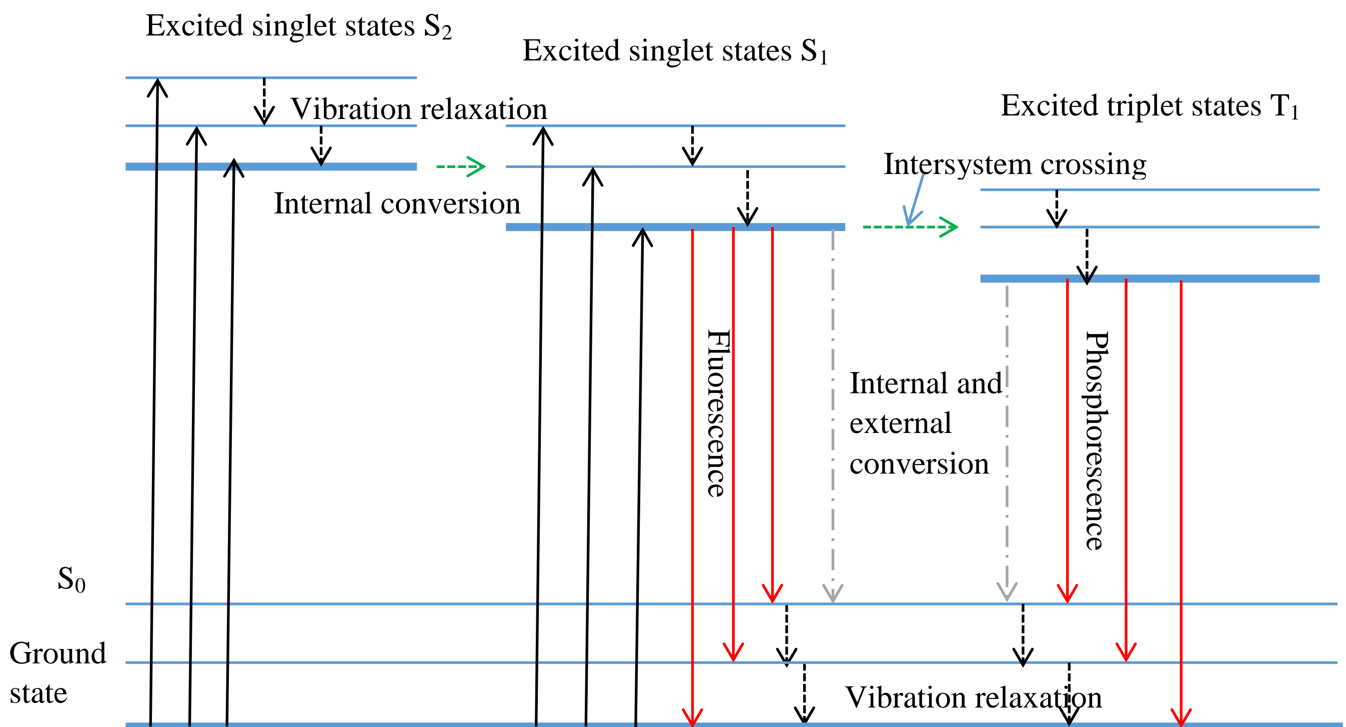

Figure 2.7 Energy level diagrams for fluorescence and phosphorescence.

Figure 2.8 shows energy diagram for absorption and emission of photons in a semiconductor material with mid-gap trap and donor and acceptor states. Electrons are excited to the conduction band and release energy to the environment via lattice vibration relaxation. Electrons at the bottom of the conduction band can combine with holes in the valence band and emit photons, or

they can combine with holes in donor states to emit light. States of acceptor are almost filled at room temperature so the probability is quite low. If there are trap states such as surface, interface or defects states, electrons can also get trapped in these states before recombining with holes in the valance band along with the corresponding emitted photons. Electrons in donor states can also absorb incident photons and be excited deep into the conduction band. Recombination between electrons in the conduction and holes in the valence band will generate photons of highest energy, when detected by PL spectroscopy, and energy band gap of semiconductor can be obtained. Nonradiative recombination may also occur through intermediate states of semiconductor materials. Therefore we can see, even though emissions through traps add complication to PL spectrum, the relatively high density of states of band still provides accurate probe of the overall band structure of a semiconductor system.

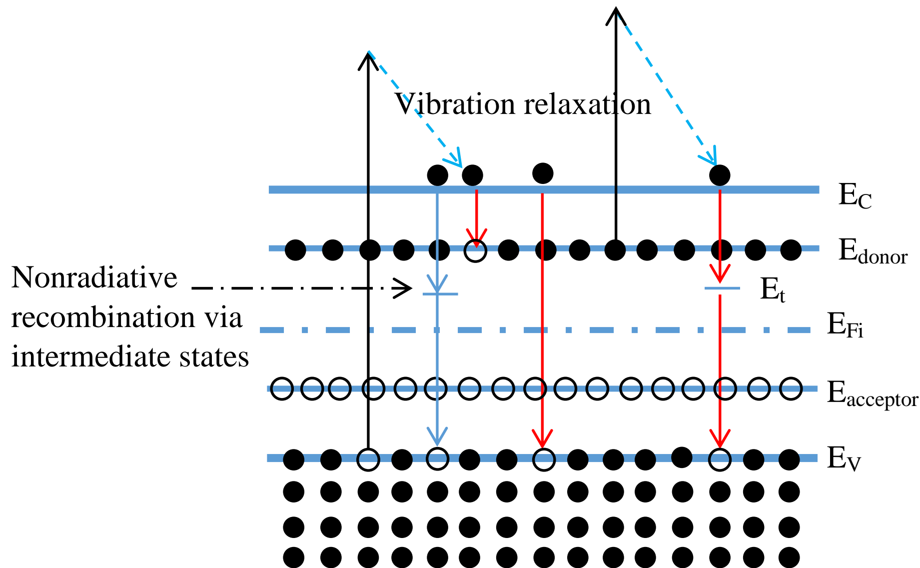

Figure 2.8 Energy diagram for emission under the presence of donor, acceptor and trap states.

The unique sensitivity of PL to discrete electronic states provides a means to characterize surfaces and interfaces. PL signals are often generated near the surface of a material, if a material

that is irradiated with a light source close to its E_g. Under these conditions, it is a suitable characterization instrument for investigation of nanomaterials surface such as ZnO nanowires in this study.

The PL signal can be easily affected by the following parameters. Photoluminescence excitation energy and intensity have profound effects on PL signals. Absorption of most materials depends on the selected exciting photon energy, and penetration depth of the incident light is determined by the excitation wavelength. Hence, different excitation energies probe different regions of the sample [103]. Intensity of excitation determines the density of photoexcited electrons and holes, which governs behavior of these carriers.

Surfaces and interfaces usually contain a high concentration of impurity and defect states. If the testing temperature is sufficiently low that thermal energy cannot de-trap electrons from the trap states, carriers can be trapped in these states. If these electrons recombine radiatively with holes, information about impurities and defects can be detected. If these impurity and defect states locate near the conduction or valance band, which is called shallow level, they are more likely to participate in radiative recombination when the temperature used is very low. In contrast, if these states locate far away from the valence or conduction band, we call them deep level states. Deep level states tend to facilitate nonradiative recombination by providing a stop-over for electrons, making their way between the conduction and valence bands. For example, dangling bonds on the surface contribute significantly to nonradiative recombination of electron-hole pairs. Intensity of PL signal depends on the rate of radiative and nonradiative events, which in turn depends on the density of nonradiative interface states. Broad, deep PL emission is a common

characteristic of low-quality semiconductors, also detected in this study [103]. Thus photoluminescence line width can be used to analyze disorder and surface roughness.

In summary, applications of PL analysis range from simple spatial scans to epitaxial wafers to exhaustive investigations of excitation-intensity-dependent PL in novel materials. PL is expected to play more important roles in the future.

Chapter 3

Electrochemical Deposition of ZnO Nanowires

This chapter focuses on experimental growths of ZnO nanowires through electrochemical deposition method, while preliminary research of hydrothermal growth of nanowires was processed to optimize growth parameters for desired materials. Applying optimized growth conditions, electrochemical deposition methods were used for nanowire fabrication, for which chemical reactions, advantages, disadvantages, growth mechanism and influence factors were analyzed. For a better understanding of electrochemical deposition, we investigated semiconductor/solution contacts through introducing a Helmholtz layer.

In this chapter, for hydrothermal grown ZnO nanowires, the two SEM images and some measurements include nanowire density, nanowire diameters and lengths were contributed by Minoli Pathirane.

3.1. Introduction to ZnO Nanowire Structure

In nature, most ZnO crystals have the hexagonal wurtzite structure, consisting of alternating planes. Figure 3.1 shows the typical hexagonal crystal structure of ZnO. One plane is composed of tetrahedral coordinated O^{2-} which is negatively charged, and the following plane is consisted of Zn^{2+} atoms that are positively charged. These planes are indexed as (0001) plane and are polar planes. Polar planes consisting of different elements stack one after another along the c-axis of ZnO crystal. From diagram 3.1 (b) also shows other planes of ZnO hexagonal wurtzite structure such as (0001), $(01\bar{1}0)$, $(\bar{1}2\bar{1}0)$, $(10\bar{1}0)$ and $(2\bar{1}\bar{1}0)$. Different growth parameters result in different growth directions which lead to different structures including nanowire, nanorod,

nanobelt, and nanoplate structures. Without external influence, growth of ZnO is along (0001) direction, however, growth along neutral planes such as $(01\bar{1}0)$, $(\bar{1}2\bar{1}0)$ and $(10\bar{1}0)$ are also significant at some levels.

Formation of ZnO nanorods and nanowires follows the following steps. As mentioned, ZnO prefers to grow along (0001) direction. Pre-coated substrates were covered with a ZnO thin film with (0001) plane exposed. For example, when sub-planes with O^{2-} ions are exposed to the growth solution, these polar planes are composed of many unsaturated chemical bonds; in addition, oxygen has relatively larger electronegativity. All of these properties will help O^{2-} to attract Zn^{2+} ions in the growth solution. After some chemical reactions that will be discussed later, O-Zn bonds will be formed and result in the formation of polar planes composed of Zn^{2+} ions. Following the same principles, Zn^{2+} ions attract O^{2-} ions in the growth solution and form polar planes of O atoms. Because of the relatively higher growth rate along (001) planes compared with others, nanowires or nanorods are possible to be fabricated.

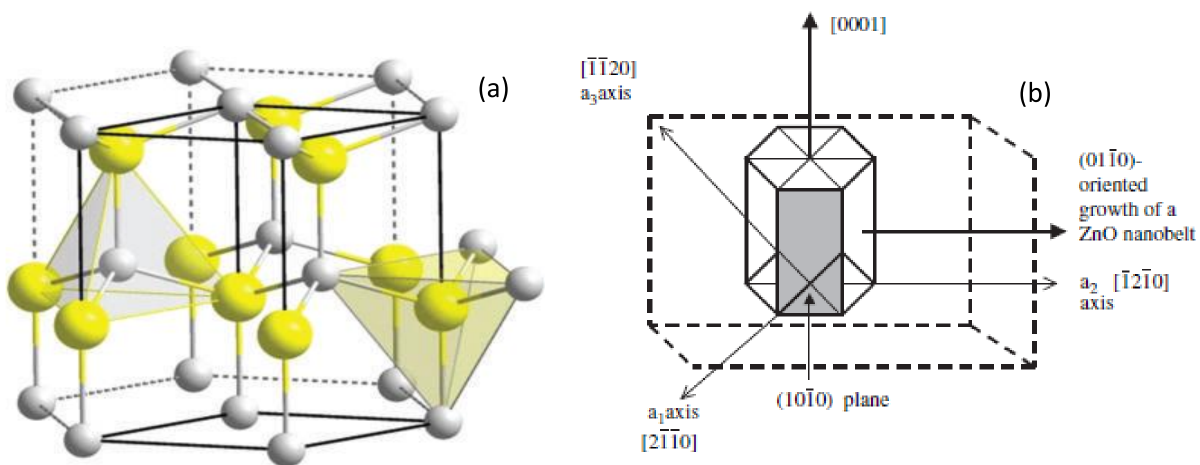

Figure 3.1 Schematic diagrams of (a) ZnO crystal structure. Yellow balls represent Zinc atoms and grey balls for oxygen atoms. Diagram (b) shows different planes of ZnO crystal [104].

3.2. Preliminary Research--Hydrothermal growth

3.2.1 Growth Conditions

Growth of ZnO nanomaterials is a very sensitive process. ZnO nanowire growth using wet chemical (i.e. hydrothermal) method without electric field was investigated before the study of electrochemical deposition. Figure 3.2 is a schematic diagram of hydrothermal growth of ZnO nanowires without electric field. Used silicon substrate is boron highly doped p-type conductive semiconductor with orientation <100>. Before nanowire growth, 50 nm ZnO or Al doped ZnO (AZO) thin films were deposited at room temperature and 250°C, respectively, in a high vacuum environment through magnetron sputtering deposition techniques. This pre-coated thin film acts as seed layer for ZnO nanowire growth. Growth solution consists of 12.5 mM zinc nitrate and hexamethylenetetramine (HMTA) in a 320 ml water bath. Substrates were mounted onto a homemade sample holder and the side coated with seed layer faced down, which can effectively reduce contamination of ZnO clusters formed in the growth solution. The solution bath was heated on a hotplate to 90 °C, and the growth time varied from half an hour to several hours. As-grown nanowires were cleaned with DI water gun and dried with air gun.

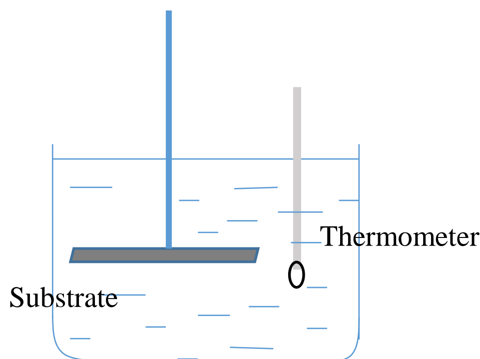

Figure 3.2 a brief schematic diagram of equipment used for hydrothermal growth of ZnO nanowires.

3.2.2 Influences of Growth Parameters

To optimize structure and morphology of as-grown nanowires, the following will discuss growth parameters including temperature, concentration and growth time and possible growth mechanisms.

Temperature Influences on Nanowire Density

Figure 3.3 shows SEM images of ZnO nanowires grown at different temperature. Figure 3.3 (a) is a SEM image for nanowires grown at 80 ^{o}C for 2 hours; the resulting nanowire length is around 900 nm with a diameter about 130 nm. And (b) shows nanowires grown at 90 ^{o}C for 2 hours; the length is about 1000 nm with diameter approximate 65 nm. We found the density of nanowires increase with the increase of temperature. According to kinetic theories, ions at low temperature have low mobility and short diffusion length, which means ions can only move in a relatively small area. Instead of forming many small nucleation sites, those ions spend more time together and react to form large nucleation sites, which results in a low density of nanowires. In comparison, at high temperature, mobility of ions is much higher so ions can move all over the substrate surface and form abundant small nucleation sites. It is also observed that, at high temperature, tops of nanowires are tapered. This can be explained that as HMTA a weak alkali, it will slowly decompose and provide OH^- ions to react with Zn^{2+} ions. While at high temperature, HMTA will decompose very fast and get exhausted soon, and then the formed OH^- will quickly deplete Zn^{2+} ions. As a result, approaching to the end of the growth process, there are not enough zinc ions forming the tapered shape of the NWs.

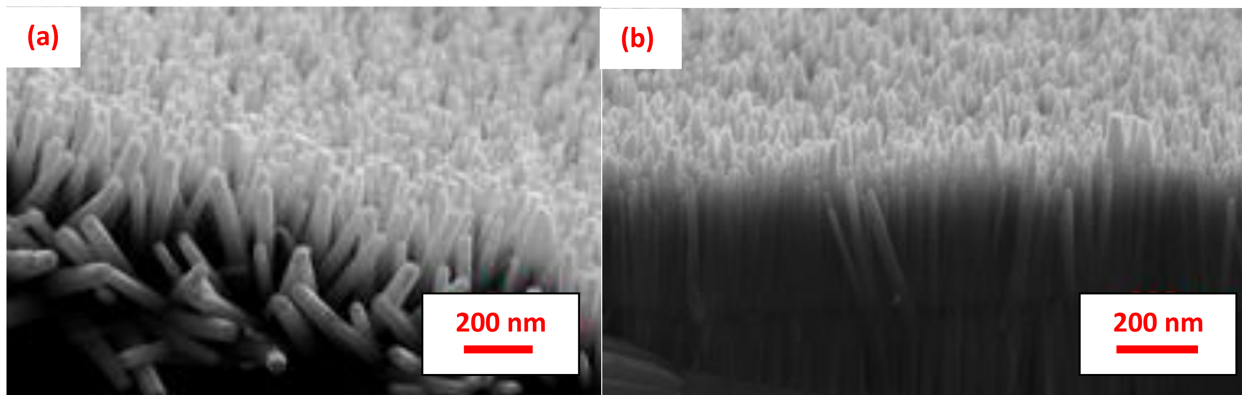

Figure 3.3 SEM images for ZnO nanowires grown at 80 ^{o}C (a) and 90 ^{o}C (b) through hydrothermal method without electric field.

Precursor Concentration Influences on Nanowire Density

Figure 3.4 shows an average density of as-grown nanowires as a function of concentration. It was found that in a relative low concentration range from 1 mM to 3 mM of HMTA and zinc nitrate, density increases with the increase of concentration. However, continuous increase of growth concentration leads to the slightly decrease of nanowires and stay stable at about 90 nanowires per 100 μm^2. At low growth concentration region, the increase of concentration will turn out more nucleation sites on the substrate surface therefor raise the density. To compare, in the high concentration region, nucleation sites get saturated and it is an option for ions to form new nucleation sites on the substrate or combine with already existed ones to contribute nanowire growth. Because the relatively low energy required, precursors will be depleted for the growth of nanowires, which turns to be a much more stable density. When the density increases to certain point that no enough space left to for new nucleation formation, so two small nucleation sites will merge each other and form a bigger one, this slightly decreasing nanowire density but leading to nanowires with bigger diameter.

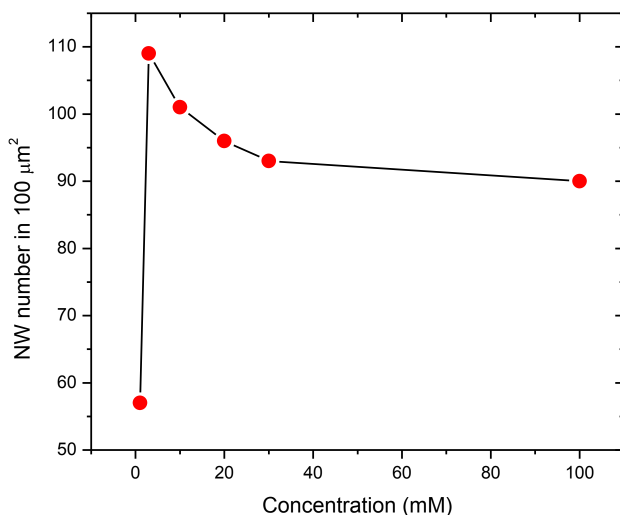

Figure 3.4 Density changes with the concentration of growth precursors.

Growth Time Influences on Nanowire Aspect Ratio

Figure 3.5 is a histogram showing the relationship between nanowire length and width. Obviously, nanowires grown for 5 hours are much longer with bigger diameter those of nanowires grown for only 1 hour. Length of nanowires depends on growth along polar planes (or axial growth), and the diameter, however, is determined by growth along non-polar planes (or lateral growth). Through the investigation of aspect ratio, we found that in the beginning, lateral growth speed is higher than axial growth. However, from 0.5 hour to 6 hours axial growth speed exceeds the speed of lateral growth. After 6 hours' growth, two growth speeds are almost equal. This is related to the relative surface area changes, as when nanowires get longer the lateral surface is significantly large enough to increase reactions on the sides of nanowires, comparable with polar growth.

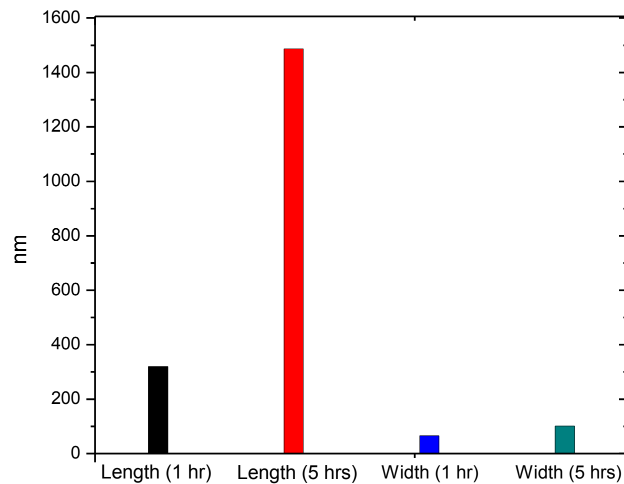

Figure 3.5 Histogram for nanowire length and width (diameter) changing with growth time.

Optimized Growth Condition

In conclusion, nanowire density can be optimized by changing growth temperature and concentration of precursors. To get nanowires with high aspect ratio, growth time cannot be too short or too long. For present growth experiments, we find desired nanowires can be obtained by growth at 90 ^{o}C, for 3 hours with zinc nitrate and HMTA concentration 12.5 mM.

One of the advantages of hydrothermal growth of ZnO is that is has low requirements for substrate. Nanowires were also found to be able to be grown on silicon, glass and plastic substrates.

3.3. Electrochemical Deposition

3.3.1. Growth Parameters

Electrochemical deposition is an upgraded hydrothermal growth of ZnO nanowires with the application of electric field. Therefore, a rectangle stainless steel sheet was used as the ground electrode, pre-coated substrate is the working electrode, and Ag/AgCl reference electrode was applied to monitor the relative potential. Electric field was realized by the application of a DC power supply; in addition, modified multimeters are used to monitor reaction current and the electric field potential with respect to Ag/AgCl reference electrode. After growth processes, samples were cleaned using deionized water and dried with an air gun. If necessary, post-growth annealing was arranged at 500 ^{o}C in a high vacuum ambient for half an hour to decrease concentration of crystal defects. Relative potential used for electrochemical deposition ranges from 0.8 V to 1.2 V. The higher the potential is the faster the growth rate will be. And the corresponding current is from 6 mA to 12 mA, respectively.

Figure 3.6 shows the schematic diagram of equipment used for electrochemical deposition of ZnO nanowires. Through this homemade deposition system we can control nanowire growth through monitoring the current and potential with respect to the Ag/AgCl reference electrode. Current and voltage were measured with the assistances of two commercial mulitimeters and a 100 Ω resistor. The substrate, with a seed layer, faces down to avoid undesired deposition onto the sample from suspended particles in the bath. Through changing supplied voltage, potential and current can be adjusted as necessary.

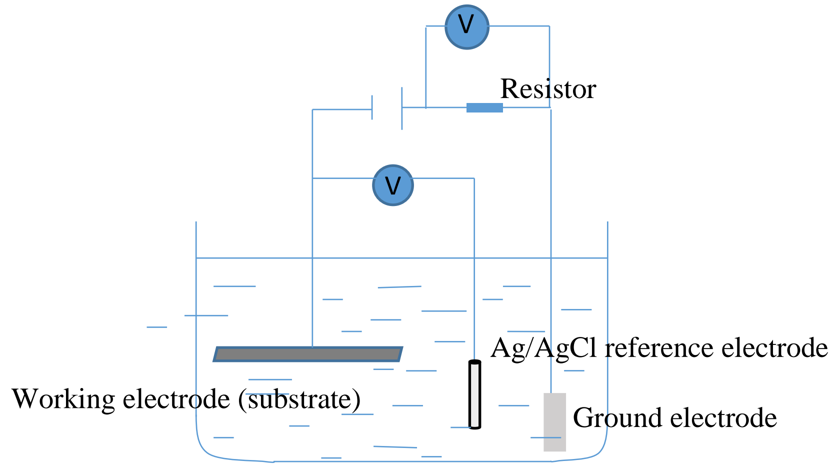

Figure 3.6 a schematic diagram of equipment used for electrochemical deposition of ZnO nanowires.

3.3.2. Chemical Reactions and Mechanisms

Chemical reactions and growth mechanism of ZnO nanowires using electrochemical deposition are similar with that of hydrothermal growth without electric potential, while electric field mainly influences the fabrication of nanowire kinetically. This section will compare the chemical reactions and mechanisms of these two growth methods.

3.3.2.1. Disadvantages of Hydrothermal Growth

In the absence of electric field, HMTA ($(CH_2)_6N_4$) and $Zn(NO_3)_2$ will experience the following reactions:

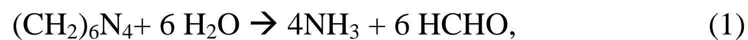

$$(CH_2)_6N_4 + 6\,H_2O \rightarrow 4NH_3 + 6\,HCHO, \qquad (1)$$

$$NH_3 + H_2O \rightarrow NH_3 \cdot H_2O, \qquad (2)$$

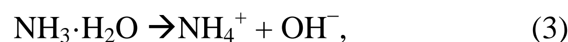

$$NH_3 \cdot H_2O \rightarrow NH_4^+ + OH^-, \qquad (3)$$

$$Zn^{2+} + 2OH^- \rightarrow Zn(OH)_2, \qquad (4)$$

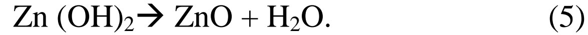

$$Zn(OH)_2 \rightarrow ZnO + H_2O. \quad (5)$$

Firstly, weak alkali HMTA will react with water and decompose to even weaker basic material NH_3. As for the high electronegative property of N atom, it will snatch H atom from water molecules and produce OH^- ions. Due to columbic force between Zn^{2+} and OH^-, unsolvable $Zn(OH)_2$ is formed, however, as the extremely unstable property of $Zn(OH)_2$ will immediately degrade to ZnO and H_2O. During the growth of ZnO nanowires, zinc and oxygen atoms exist on the surface of ZnO, interacting with water and OH^- ions, therefore to fabricate ZnO nanowires.

Disadvantages of hydrothermal growth method without electric field include the following several points. First, HMTA is the only source of OH^-, OH^- is not enough at the end of long growth process. Second, Zn^{2+} and OH^- ions uniformly distribute in the entire growth solution, significant amount of the formation of ZnO occur in solution instead of on the substrate that contributes to nanowire growth. This can be demonstrated by the observation of abundant white depositions suspended in the growth solution or sat at the bottom of the reactor, which leads to a waste of precursors. Thirdly, low efficiency of doping, also results from the significant depletion of materials in the solution. These two main defects lead to the slow growth rate of ZnO nanowires.

3.3.2.2. Electrochemical Deposition Growth

Theory Overview of Electrochemical Deposition

By applying an electric field, disadvantages of hydrothermal growth can be overcome. Electrochemical deposition is based on the principle of redox reaction at two electrodes by

connected to a DC power supply. Applied electric field will destroy the uniform distribution of the ions, and the cathode will attract cation ions in the growth solution. These positive ions will be reduced through getting electrons from the cathode and being deposited onto the cathode substrate if the formed materials are insoluble. In contrast, for positively charged anode, materials rich with electron will be oxidized and loss electrons to the anode. So the solution connects the anode and cathode by redox reactions. Without an external electric field, the redox reaction is in equilibrium and each redox reaction has its own potential, furthermore anode and cathode have their own potential parallel to a half battery. This is called primary cell. With the application of DC power the primary cell changes to an electrolytic cell.

Positive ions from electrolyte solution migrate to the cathode and then receive electrons to get reduced, then part or all of their positive charge will be lost and positive ions will become new lower charged ions or neutral atoms or molecules. This process is known as reduction. Meanwhile, negatively charged electrons will migrate to the anode and transfer electrons to it, through which it becomes new lower negatively charged ions or neutral atoms or molecules. This process is so called oxidation. The Nernst equation is used to relate the formal potential of an electrode to the equilibrium potential in the presence of a solution of its ions. Firstly, without a DC power supply, potential can be calculated by the following equation (6):

$$E = E^{\ominus} - \frac{RT}{zF} ln \frac{a_G^g a_H^h}{a_C^c a_D^d} \quad (6)$$

This equation is derived from the reaction equation (7) below,

$$cC + dD \rightarrow gG + hH \quad (7)$$

where $E^{\ominus}$ is the formal potential; n is the number of electrons needed for the reduction of one ion; F is the Faraday constant; R is the gas constant; T is the absolute temperature, and α is the active concentration.

When electrode potential is made more cathodic than the equilibrium value by imposing an external applied potential on it such as a DC power supply, electrochemical deposition occurs until the positive ion concentration is lowered to the value in equilibrium. Through making the electrode sufficiently negative (cathodic), the positive ion remaining in the solution will reduce to a negligible concentration.

Chemical Reactions and Mechanisms

If we investigate the solution we will find it includes H^+, Zn^{2+}, NO^{3-}, NH_3, H_2O, OH^-, NH_4^+, $(CH_2)_6N_4$, ZnO and $Zn(OH)_2$. Some of them are potential elements that will get oxidized or reduced to transfer charges. So the reaction in the electrochemical deposition can be quite complex partly by the changing concentration of each ion or molecule. Nanowires grown on the cathode substrate, so in the following part of this section, reduction reactions will be discussed. Ions or molecules will get charges from the cathode; if they want to get reduced at the cathode they need space in orbits to accept new electrons (i.e. valence of active elements should not be lowest). For example, N in NH_3 and NH_4^+ has the valance of -3, which is the lowest valence for N elements, so N in NH_3 and NH_4^+ in this case do not have enough space in the electron orbits to accept another electron. Element ions in growth solution that can be reduced at cathodes are H^+, Zn^{2+} and N in NO^{3-}. In order to find which one will be reduced, we need to find out what they will become if they are reduced. To make the calculation easier, the following hypothesis are

made: firstly, the density of solution is 1g/L (the same as that of water); secondly, concentration of salt are extremely low. Thirdly, activity coefficient is 1. If all reductions are possible we can get the following equations.

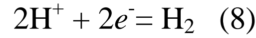

$$2H^+ + 2e^- = H_2 \quad (8)$$

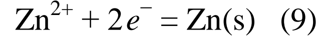

$$Zn^{2+} + 2e^- = Zn(s) \quad (9)$$

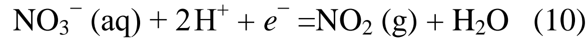

$$NO_3^- (aq) + 2H^+ + e^- = NO_2 (g) + H_2O \quad (10)$$

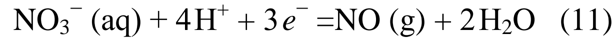

$$NO_3^- (aq) + 4H^+ + 3e^- = NO (g) + 2H_2O \quad (11)$$

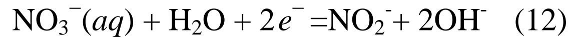

$$NO_3^-(aq) + H_2O + 2e^- = NO_2^- + 2OH^- \quad (12)$$

For 160 ml solution with concentrations of $Zn(NO_3)_2$ and HMTA are 12.5 mM, the measured pH is 6.8, using equation (6) we can calculated E at equilibrium.

Table 3.1 E^{Θ} *(V)* and E *(V)* values for possible reductants.

	H^+	Zn^{2+}	NO_3^-	NO_3^-
Product	H_2	Zn(s)	NO_2 (g)	NO (g)
E^{Θ} *(V)*	0	−0.7618	+0.80	+0.80
E *(V)*	-0.17544	-0.818	-0.117	-4.7

Potentials in the table are reduction potentials. If the value is positive that means the reactions as written is spontaneous, otherwise it is not spontaneous. Therefore, for our situation, the less negative the E value is the easier for the reaction to occur. So the order for those ions to get discharged is NO_3^- (to produce NO_2), H^+, Zn^{2+} and then NO_3^- (to produce NO), actually because the existence of hydrogen overpotential H^+ may be the last one to be reduced. The potential we

applied is from -0.8 V to -1.2 V, which is much more negative than -0.117 V, this is due to the potential drop caused by resistance and electrode polarization effect. In a practical experiment, when the potential increases to more than -1.2 V, metallic substance was deposited that should be the reduction of Zn^{2+} to form Zn.

The reduction of NO_3^- is involved in the depletion of H^+, and this is a way to decompose H_2O. Decomposition of water will increase the relative concentration of OH^-, so local pH value of growth solution is increased and this process consistently provides OH^- for the formation of $Zn(OH)_2$ that will decompose immediately to ZnO. This is one way that electric field helps the growth of ZnO nanowires through providing more precursors. The other way is through the increase of local concentration of Zn^{2+}, although Zn^{2+} will not be reduced at the low potential range, but it still will migrate to the cathode due to applied electric field, resulting in a higher local concentration of Zn^{2+} near the cathode so as to reduce the waste of precursors in growth solution. In conclusion, electric field applied indirectly improves ZnO nanowire growth.

Thermodynamic and Kinetic Analysis

Crystal growth is determined by thermodynamic and kinetic mechanisms. Specifically, thermodynamics determines the driving force for the overall growth process and kinetics defines the rates at which various processes occur. Figure 3.7 shows the energy changes during electrochemical reactions. Electric field is not directly involved in the reaction so activation E_1 is the same as that in the absence of electric field. E_2 is energy barrier for reaction from $Zn(OH)_2$ to ZnO, which reaction is immediately so it is not the rate control step or rate control energy barrier. The total energy difference is ΔE_2 as shown in the figure 3.7. Therefore thermodynamically the

reaction is possible. Temperature (90 °C) applied to the growth process was used to overcome energy barrier E_1 and E_2.

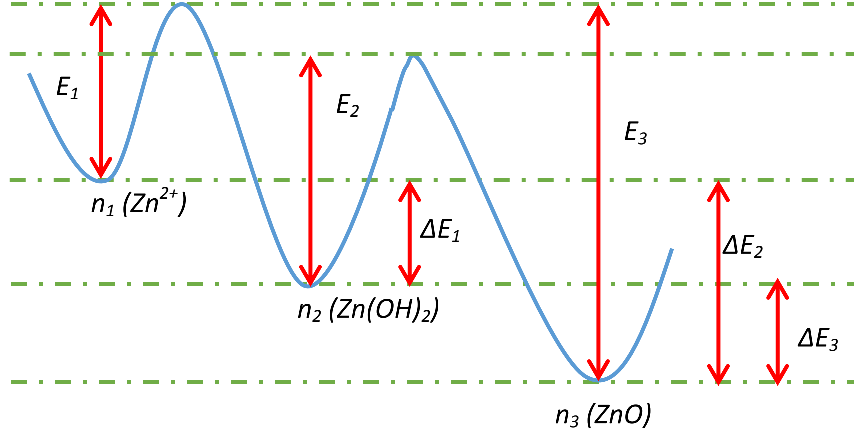

Figure 3.7 a schematic diagram for energy changes during electrochemical growth of ZnO.

Growth rate of ZnO nanowires follows the following relationship.

$$Rate \sim nAe^{-\frac{E}{KT}} \quad (13)$$

Where A is the attempt frequency with the unit (1/s), and E is the activation energy with the unit (eV). In the case of ZnO nanowire growth, transition from Zn^{2+} to $Zn(OH)_2$ is the speed control step , so E is equal to E_1 here. By drawing plot of *ln(Rate)* versus temperature T, we can get the value of E_1. From equation (1), we can get that growth rate increases with the increase of precursor concentration and the increase of temperature T.

At the very beginning of the reaction, assuming a moment that the reaction is infinitely slow, so we can obtain the following relationship in the situation of thermodynamic equilibrium.

$$\frac{n_1}{n_2} = e^{-\frac{\Delta E}{KT}} \quad (14)$$

Where n_1 and n_2 is the concentration of Zn^{2+} and $Zn(OH)_2$, respectively. And ΔE is the energy difference between E_1 and E_2.

3.3.3 Results of Electrochemical Deposition

Figure 3.8 shows SEM images of ZnO nanowires grown through electrochemical deposition method at the potential of -0.8 V. Nanowires grown from electrochemical deposition are uniform, well oriented with high quality. Figure 3.9 illustrates the growth rate versus potential of electric field. Obviously, the growth rate increases with the increase of negative potential and is much higher than that without electric potential. Growth rate is from 2 to 4μm/h when the potential is from -0.8 V to -1.0 V, which are potentials used throughout this study. When the potential of electric field was too high (over -1.2 V), nanowire quality (such as the uniformity) decreased as shown in Figure 3.10. Figure 3.11 shows the XRD diagram of ZnO nanowires grown by electrochemical deposition at -0.9 V. The sharp peak of (002) plane reflects the dominant growth direction along polar planes (or axial planes) and good orientation property of as-grown ZnO nanowires. In comparison, other peaks are not high enough to be observable.

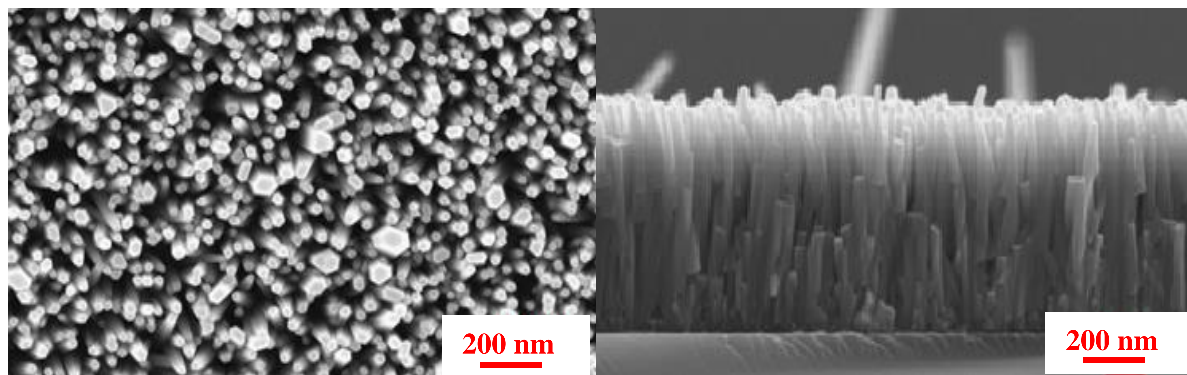

Figure 3.8 SEM images of ZnO nanowires grown through electrochemical deposition method at potential of -0.8 V.

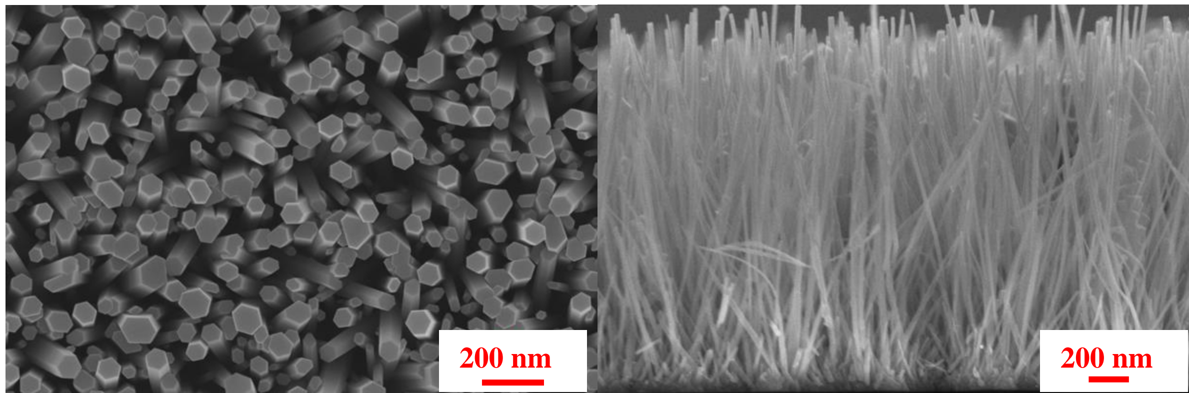

Continued: Figure 3.8 SEM images of ZnO nanowires grown through electrochemical deposition method at potential of -0.8 V.

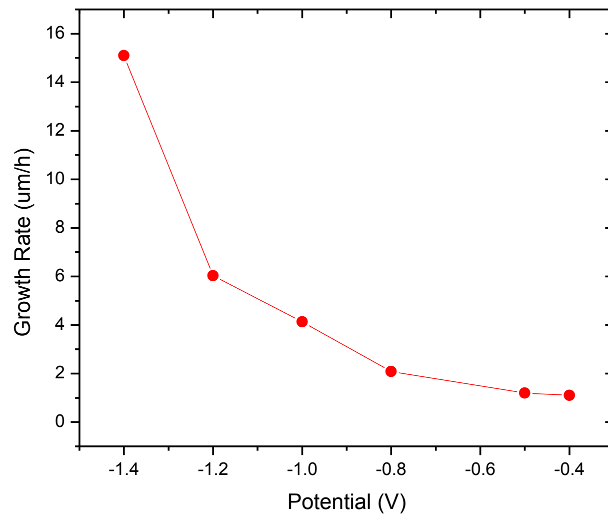

Figure 3.9 Diagram of growth rate of ZnO nanowires grown through electrochemical deposition method at different potential.

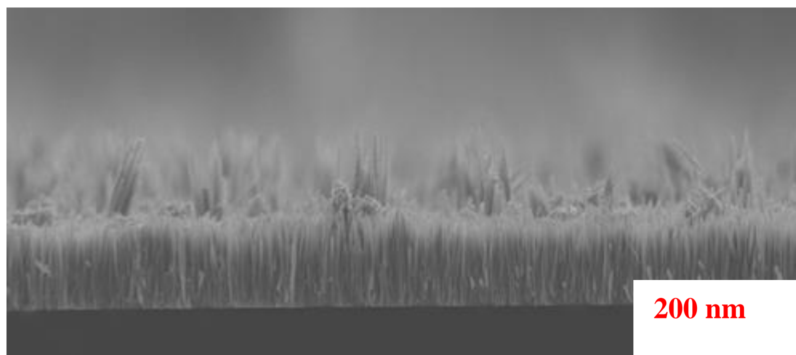

Figure 3.10 SEM images of ZnO nanowires grown through electrochemical deposition method with potential -1.2 V.

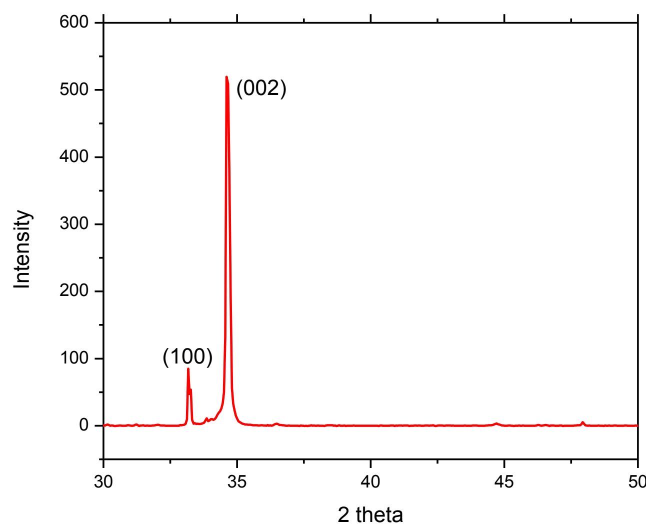

Figure 3.11 an XRD diagram of ZnO nanowires grown through electrochemical deposition method at potential of -0.9 V.

3.4. Semiconductor/Solution Interface

Electrochemical deposition of metal and alloys onto metallic substrates is very important in modern technologies. In the electronic industry, electrochemical deposition is of great interest used for applications such as copper boards, multilayer read/write heads, thin film magnetic recording media and through-hole plating. However, there are few reports about deposition semiconductor materials to semiconductor substrate. While substrate/solution interface has significant influences on ZnO nanowire deposition through affecting potential distribution, charge carrier transfer and chemical reactions, and these parameters determine ZnO nanowire structure, electrical and optical properties. Therefore, this subsection will study the substrate/solution to have better understanding of ZnO nanowire growth through electrochemical deposition.

3.4.1 Introduction to Helmholtz Layer

In 1879, Helmholtz developed the concept of double layer at the surface of a metal being in contact with an electrolyte. A specific interfacial region formed whenever we immerse an electrode in an electrolyte solution. This region is called Helmholtz layer or double layer. This Helmholtz layer can significantly influence electrochemical deposition, so it is worth discussing its electrical properties. An electrical model of electrochemical deposition was depicted below, in which double layer is viewed as a capacitor. Refer to Fig. 3.6; Fig. 3.12 depicts a schematic diagram of electrochemical cell, where it is represented by an electrical circuit. A capacitor represents the double layer. Resistances in the circuit are also included, and they are substrate/solution interface resistance R_s, connection wire resistance R_{wire} as well as resistance $R_{soultion}$ caused by electrolyte solution. When the circuit is charged, double-layer capacitor will be charged firstly, but this capacitor current is not related to the reduction or oxidation of the substrates. The capacitive current will interfere in the electrochemical investigations. There is no general model for double layer applicable to all experimental situations, as its capacity depends on several parameters such as: electrode material (metal, carbons, semiconductors, electrode porosity, the presence of layer of either oxides or polymeric films or other solid materials at the surface), type of solvent, type of supporting electrolyte, extent of specific adsorption of ions and molecules, and temperature.

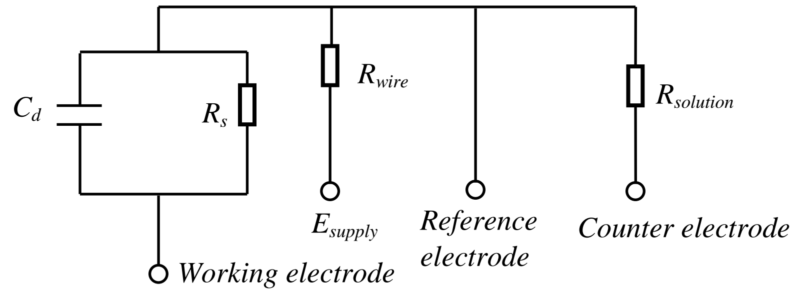

Figure 3.12 an electronic scheme equal to electrochemical cell. R_s is substrate and solution interface caused resistance; R_{wire} is the resistance induced by connection wire; $R_{solution}$ is electrolyte solution resistance; C_d is the capacitance of double layer capacitor.

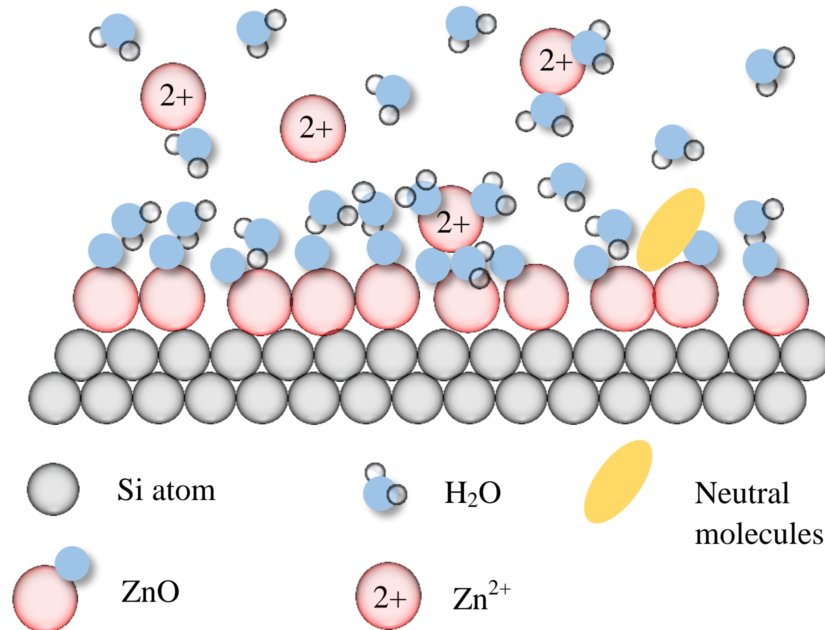

Figure 3.13 General representation of the double layer formed at the ZnO-electrolyte interface.

The formation of double layer is caused by natural properties of negative or positive charged substrate surface. As shown in Fig. 3.13, for ZnO coated silicon substrate the surface material is ZnO. In the presence of water, ZnO will hydrolyze to form hydroxide layer at the surface (≡Zn-O···H-O-H). Water molecules can be absorbed chemically by hydrogen bonds or physically.

Polar hydroxyl (-OH) groups may cause the surface to attract and physically adsorb a single or several additional layers of polar water molecules. The experimental pH of growth solution is 6.8, so ZnO surface can also react with H^+ ions and become positively charged. Large neutral molecules like HMTA can also be absorbed and will remove some water molecules from the surface.

3.4.2. Substrate/Seed Layer Interface

In electrochemical deposition processes, electrons travel along the whole circuit, so electrons transfer to the solution may through the conduction band, valance band or surface states and trap states of the semiconductor. If the semiconductor is n-type, during electrochemical deposition electrons are transferred through conduction band, this process is usually preferred as the nucleation and growth can be controlled externally through adjusting applied potential or current [105]. Because of the low density of surface electrons, compared with deposition on metal, deposition on semiconductor surface is slower, which will significantly affect properties such as adhesion and texture of the deposits.

For the case of depositing ZnO onto ZnO pre-coated silicon substrate. Seed layer of ZnO is about 50 nm and silicon substrate used is boron doped highly conductive semiconductor.

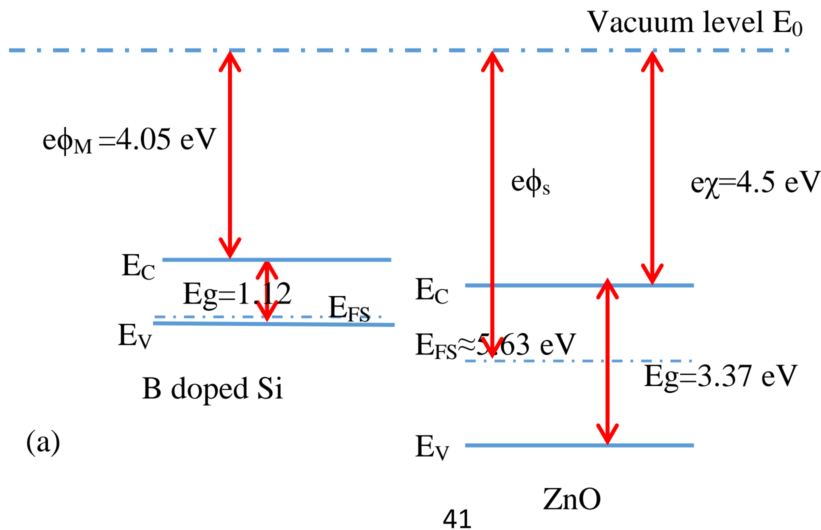

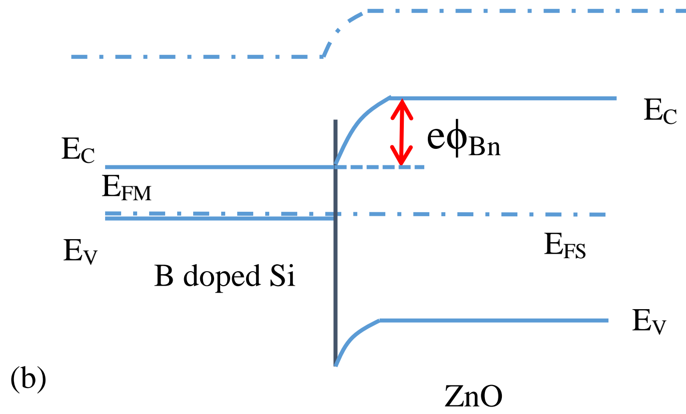

Figure 3.14 energy band gap diagrams for p-type silicon and n-type thin film ZnO seed layer contact. (a) Before connecting and (b) after connecting.

Figure 3.14 shows the diagram of energy band gap of boron doped silicon substrate and ZnO seed layer thin film. During deposition processes, electrons are provided by DC power supply and transfer from Si substrate through conduction band to the ZnO seed layer, however, from figure 3.14, there is an energy barrier at the interface between Si and ZnO thin film, which equal to $(E_{FS(ZnO)}$- $E_{FS(Si)})$-($E_{FS(ZnO)}$- $E_{FS(Si)})$. Assuming as-deposited ZnO thin film is intrinsic semiconductor, then Fermi level can be calculated using the following equation (15):

$$E_{Fi} - E_{midgap} = \frac{3}{4} kTln(\frac{m_p^*}{m_n^*}) \quad (15)$$

Where E_{midgap} is 3.37 eV, the middle energy level of the band gap of ZnO, k Boltzmann's constant, m_p^* and m_n^* are effective mass of holes and electrons, T the temperature. As calculated, E_{Fi} is approximately equal to 3.37 eV. However, as discussed in the above section, intrinsic ZnO shows n-type property because of defects formed such as oxygen vacancies during the growth. So in this study as deposited intrinsic ZnO is regarded as n-type semiconductor.

3.4.3. Seed Layer/Solution Interface

As depicted in figure 3.15 the energy band diagram for n-type semiconductor and growth

solution. In growth solution, reducing agents couples including OH^-, NO_2^- and NO_3^- ions are considered as donors, and oxidizing agents are including H^+, Zn^{2+} and NH_4^+ ions are regarded as acceptors. Both donor and acceptor state have a Gaussian distribution of its energy level. In energy level diagram there must be a point at which donors and acceptors are equal. This is the equilibrium energy E_{OR}, as shown in figure 3.15. Under equilibrium, Fermi level is aligned with equilibrium energy of the solution, which results in the formation of space charge layer at the semiconductor surface and a Helmholtz layer (i.e. double layer) in the solution. In this way, a built-up charge on both side of the interface leads to the potential drop over the space charge layer on the ZnO thin film side and the Helmholtz layer on the solution side. Parallel to the Schottky contact or p-n junction, space charge is equivalent to the built-in potential and a depleted layer is formed in the semiconductor side

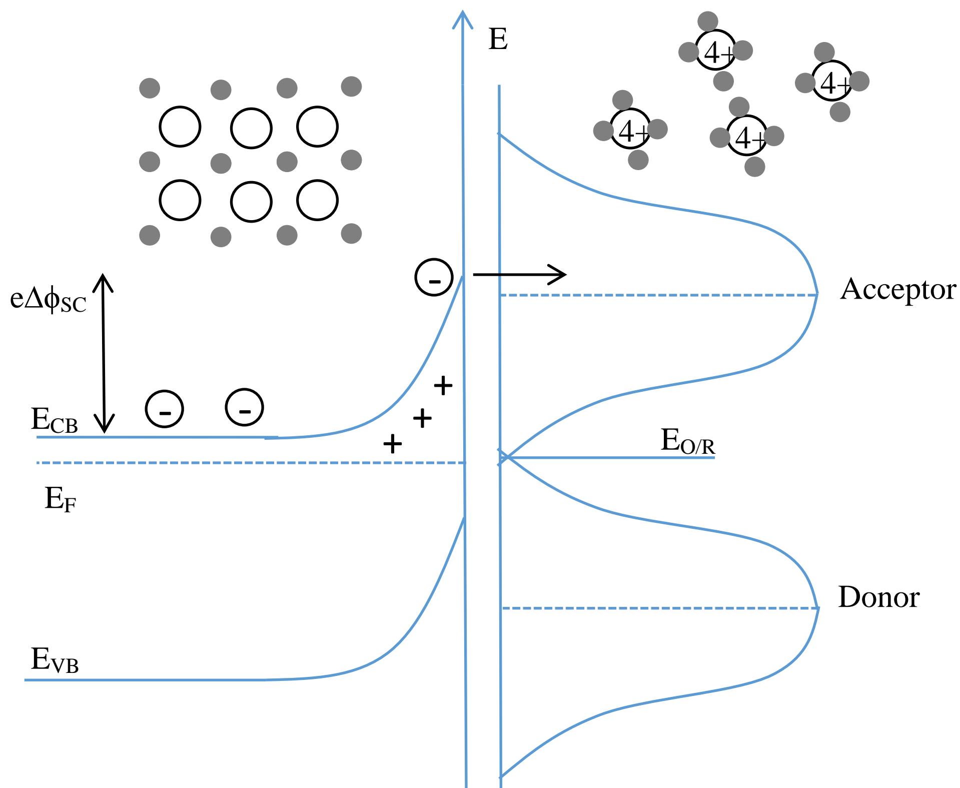

Figure 3.15 an energy band gap diagram for an n-type semiconductor in contact with solution.

Theory of metal deposited onto metal has been well established [106-111]. Situation shown in figure 3.15 is one of the three possibilities. Depending on categories and concentrations of ions in the growth solution, energy level position of $E_{O/R}$ is variable. When $E_F < E_{O/R}$, energy band diagram is shown in figure 3.15, ZnO semiconductor is depleted near the interface and energy barrier is formed when electrons flow from semiconductor to electrolyte solution, in this case extra potential is needed to overcome this barrier. Figure 3.16 (a) shows energy diagram for the case of $E_F = E_{O/R}$ and (b) for the case of $E_F > E_{O/R}$. In both situations, no barriers are formed for electrons to flow from ZnO to solution, they are partly Ohmic contacts. Therefore, with the changes of concentrations of ions such as H^+ singed by pH, electric potential needed for deposition is expected to change, correspondingly. Potential distribution at the semiconductor/solution interface is complicated since the applied potential is partitioned between the space charge layer of the semiconductor and the Helmholtz layer in solution.

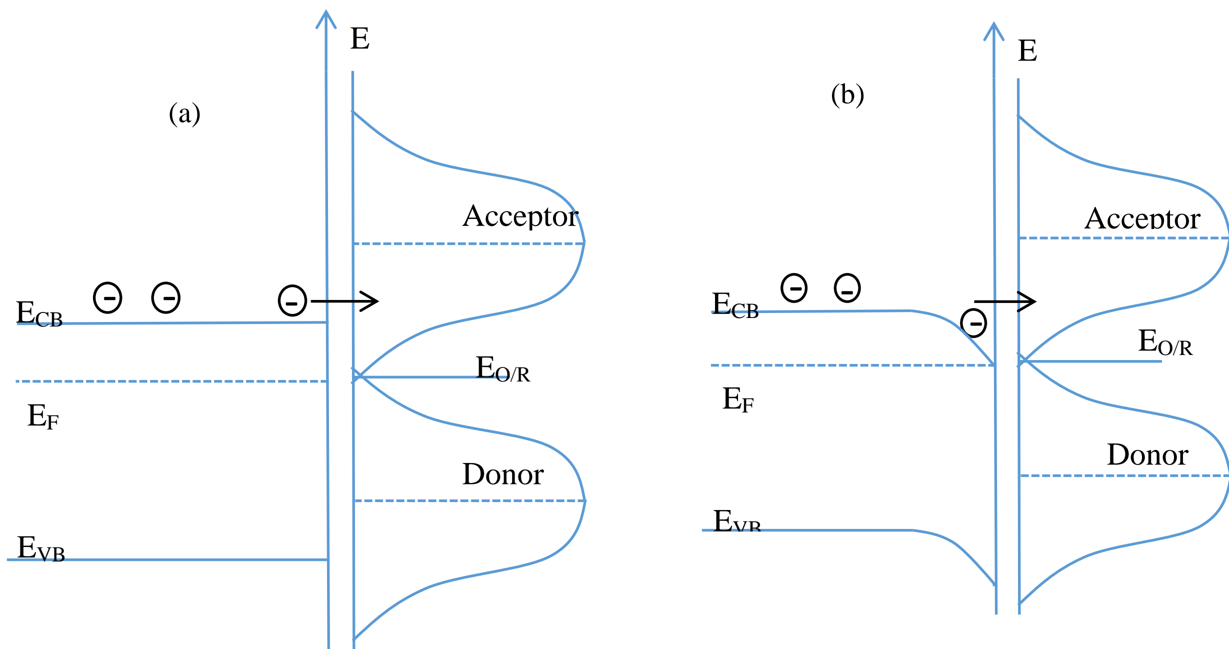

Figure 3.16 energy band diagrams for an n-type semiconductor in contact with solution in the situation that (a) $E_F = E_{O/R}$ and (b) $E_F > E_{O/R}$.

3.5. Conclusion

In this chapter, for hydrothermal growth of ZnO nanowires without electric field, influences of different growth parameters such as temperature, growth time and concentration, on nanowire morphology have been discussed, therefore, according to the analysis, through adjusting growth parameters, desired nanowires can be achieved. Electrochemical deposition was found helpful to improve the nanowire quality and increase growth rate; explanations and mechanisms of electrochemical deposition was proposed. In addition, an investigation of interface between semiconductor and solution was studied as well as the three possible band energy diagrams for semiconductor / solution contact.

Chapter 4

ZnO Nanowires Doping and Characterization

4.1. Introduction to Doping

A wide energy band gap of 3.37 eV and large exciton binding energy of 60 meV make ZnO an increasingly promising candidate as a building block material for optoelectronic devices, such as light-emitting diodes, photo detector/sensor and laser diodes [112]. Specifically, one-dimensional nanostructure nanowires due to its unique properties such as high carrier mobility as a single crystal in a single nanowire has attracted wide attention for the application of next generation nano-optoelectronic devices [113-114]. However, applications of ZnO nanowires are hindered by their intrinsic n-type conduction property of intrinsic ZnO nanowire optoelectronics caused by defects such as oxygen vacancies and Zn interstitials. Although significant efforts have been dedicated, including this study, accomplishments of p–type ZnO nanowires have not been easily reached, where most demonstrations have limited performance. Therefore, in this study, n-type and p-type doping of ZnO nanowires were tried and doped nanowire materials were characterized and analyzed.

Different methods and dopants have been investigated to get p-type ZnO nanomaterials. As reported, many groups have successfully used group V and group I elements as p-type dopants, some of them are reported in the following references [115-117]. However, the large atomic radius difference between group V elements and oxygen leads to large lattice mismatch that result in the deformation of ZnO nanostructures. Therefore, researchers have moved to the focus to doping p-type ZnO nanowire with group I elements, for instance, Li, Na, and Ag. It is also been shown by computational analysis that these group I elements will form shallow level states

[118-122]. Different doping methods have been studied for doping p-type ZnO nanowires. Sang Hyo Lee, et al. used a hydrothermal method with group I element Li [123]; Y.J. Zeng, et al. investigated Li doped ZnO thin film using dc reactive magnetron sputtering methods [124]; M.A.Thomas and J.B. Cui applied electrochemical route for the study of p-type ZnO nanowires using the Group I element Ag as dopant [125]; and Tzu-Hsuan Kao, et.al. have realized p-type properties of ZnO nanowires via doping Sb using a chemical evaporation method [126].

However, the realization of p-type ZnO by doping with a single dopant is rather difficult due to the strong n-type conductivity of ZnO (induced by oxygen vacancies and zinc interstitials) and its asymmetric doping limitation [127]. It was stated that most materials exhibit an asymmetry in their ability to be doped n type or p-type and ZnO is a paradigm system in this respect ZnO can be easily doped n type via intrinsic [128-134] or extrinsic [135] doping for high conductivity, whereas it cannot be made p-type via intrinsic doping. Due to these problems, several reports have tried to realize p-type doping through co-doping, which is supposed to enhance the solubility of acceptors in ZnO and to raise the shallow acceptor levels in the band gap [136-138], Lu et al. have tried to dope ZnO with nitrogen and aluminum [138], in which study, Al was found to facilitate the solubility of N in ZnO and the co-doped ZnO thin film showed good p-type conduction at room temperature.

Even though intrinsic ZnO nanowires are n-type materials, their conductivity is not sufficiently high for most nanoelectronic devices. Thus, many groups have investigated to achieve more conductive n-type ZnO nanowires via doping with extrinsic dopants such as Ga, In [139-143], Mn[144], Mg[145], Bi[146] and Al[147-150]. Methods used, for example, are thermal

evaporation method [151], and vapor-liquid-solid (VLS) method [152], but all of these methods are involved sophisticated equipment and high temperature.

This study will focus on fabricating p-type ZnO nanowires through doping with Li. P-type co-doping of Al/Ag, and n-type doping with Al, are also investigated. All results are characterized by scanning electron microscopy, X-ray diffraction, photoluminescence spectroscopy and Raman spectroscopy. Conductivity of Li doped ZnO was also tested and discussed in is chapter.

4.2. Theory Overview of Doping

At room temperature, intrinsic semiconductors have very low concentration of charge carriers, because thermal energy is much lower than energy band gap of the semiconductors. To compare, electron concentration for an intrinsic Si semiconductor at room temperature is about 1.5×10^{10} cm^{-3}, while copper has on the order of 10^{22} cm^{-3} electrons. Therefore the carrier concentration of semiconductor is modified by adding extrinsic dopants.

This section will discuss how impurities can be chosen to increase charge carrier concentration. Figure 3.1 in chapter 3 has shown the hexagonal lattice cell of ZnO nanowires. In the hexagonal structure, each lattice cell consists of several tetrahedral structures centered with an oxygen or zinc atom. This tetrahedral structure comes from the tetrahedral hybrid orbitals of oxygen and zinc atoms. Outer electron orbits of oxygen can be written as $1s^2\,2s^2\,2p^4$, and orbitals 2s and 2p hybrid to form sp^3, which has 4 orbits that can contain 8 electrons. Sp^3 orbits have tetrahedral structure and already have 6 electrons filled, so it still needs 2 electrons to get the most stable condition with the lowest energy system. For zinc atom, its electron orbits can be written as $1s^2\,2s^2\,2p^6\,3s^2\,3p^6\,4s^2\,3d^{10}$, they are 4s and 4p orbitals to hybridize to form sp^3 orbitals, which

has been filled with 2 electrons. As shown in Fig. 4.1. To form a stable structure, zinc still needs 6 electrons shared from oxygen and the oxygen gets 2 electrons shared from zinc. In this way, hexagonal structure of ZnO consisting of smaller tetrahedral structures is obtained. If we introduce group IB and group I elements such as Ag, Cu and Li, there is only 1 electron in the outer shell, which means the formed tetrahedral orbits are only filled with 1 electron.

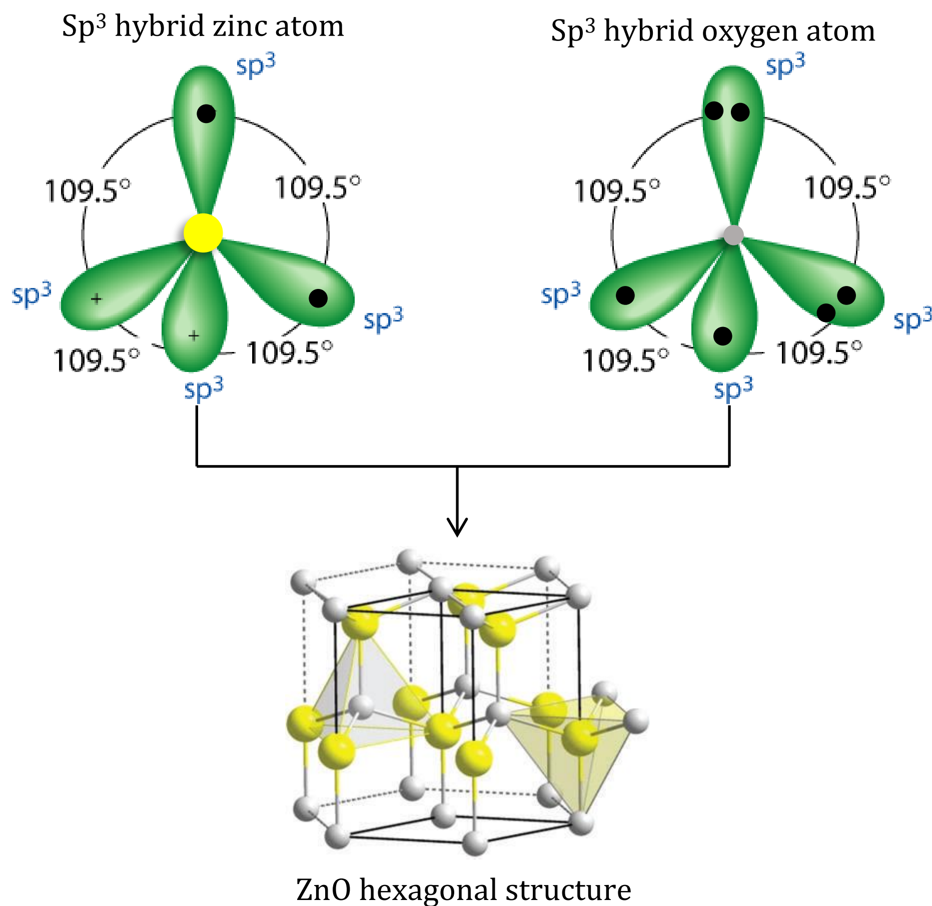

Figure 4.1 Schematic diagrams for the formation of ZnO hexagonal structure. Black ball represents electrons, grey ball the oxygen atom, yellow ball zinc atom.

In p-type material, a dopant is bonded to oxygen, resulting in a tetrahedral structure that only has 7 electrons filling eight available states; therefore there is a hole left. These holes act as charge carriers for conduction. If the impurity elements come from group V such as N, P As and Sb, which have 5 electron in the outer shell. Because of the similarity atomic volume, they will substitute an O atom and, only 5 electrons fill the sp^3 orbitals and when bonded with neighboring zinc atoms, a hole will be left to contribute to the conduction of ZnO semiconductor. These processes are for p-type doping and the impurities are called acceptors. For n-type doping, an extra electron will be left to transfer charges. This is n-type doping and impurities are called donors. The electrons and holes are weakly bonded to nucleus and only need small amount of energy (typically, on the order of 0.05 eV) to liberate the electrons and move them to the conduction band. ZnO is a semiconductor consisting of elements from two groups in the periodic table; therefore it has many potential dopants from different groups. As shown in figure 4.2 for the energy band diagram as the electron being at the donor level, E_d, lying just below the conduction band. Only a small amount of thermal energy is able to excite electrons in the donor level over the energy gap E_V-E_d to the conduction band.

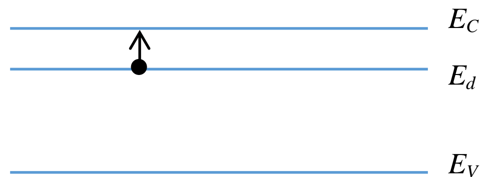

Figure 4.2.Real-space energy band diagram consisting the level of a donor electron. And the transition of electrons from donor level to the conduction band upon adding a small amount of energy.

In order to calculate the ionization energy of donors and holes, we can do an approximation by using hydrogen model, in which a two particle system is proposed (electron and the nuclei). The system of donors or acceptors immerged into the semiconductor can be considered as the

electron and everything else system. As acceptors and donors are not in real space, effective masses of electron and hole are used for the calculation. So we use effective mass to substitute m_e or m_h, and substitute vacuum permittivity with the permittivity of semiconductor, then we get equation (1) (for electrons).

$$E_n = -\frac{m_e^* q_e^4}{8\varepsilon_r^2 \varepsilon_0^2 h^2 n^2} \qquad (1)$$

If this dopant atom is ionized, the transition is from n=1 to n=∞, if we calculate the energy difference of E_1 and E_∞, we get the donor ionization energy as shown in equation (2):

$$\Delta E_d = \frac{m_e^* q_e^4}{8\varepsilon_r^2 \varepsilon_0^2 h^2} \qquad (2)$$

For ZnO,$m_e^* = 0.29\ m_e$ and ε_r =9.9 [153], we obtain ΔE_d=0.0389 eV (0.025 eV for silicon, for comparison). For holes, as $m_h^* = 1.21\ m_e$, ΔE_d=0.162 eV.

4.3. Experimental Discussion-Doping

4.3.1. Doping Conditions

First, Li doped ZnO nanowires were fabricated by electrochemical deposition method as discussed in the previous chapter. $LiNO_3$ is dissolved in 320 ml deionized water with the concentration of Li 50%, 100%, 200% and 300 % of that of zinc source ($Zn(NO_3)_2$). HMTA and $Zn(NO_3)_2$ has the concentration of 12.5 mM. Secondly, Al doped ZnO nanowires are fabricated by replacing $LiNO_3$ with $Al(NO_3)_3$ and the concentration was controlled to the 0.1 , 0.5 %, 0.6 %, 1% , 3 % and 6% of that of the zinc source. Thirdly, Al and Ag co-doped ZnO nanowires were also investigated by adding Al and Ag together in the HMTA and $Zn(NO_3)_2$ growth bath (same as the previous two except the dopant.), and the concentration of Al and Ag ions are the same: 0.5 %, 1% and 3% of the concentration of zinc source. A silicon substrate was pre-coated with

Al doped ZnO, a highly conductive thin film that was used for all growth processes. The growth temperature was controlled at 90 ^{o}C for all experiments. The electric field, at a potential of -0.9 V with respect to Ag/AgCl reference electrode, was used and the corresponding current ranges from 0.5 mA to 13 mA. The duration for each growth was from 1 hour to 12 hours. After the growth processes, samples were cleaned using a deionized water gun and dried with an air gun. If necessary, annealing was performed in a high vacuum chamber (5 mtorr) with at a flow of oxygen at the speed of 20 sccm for 30 minutes at 500 ^{o}C. To characterize the morphology and topography of ZnO nanowires, SEM was used. XRD was used to examine the growth direction of ZnO crystal and information about defects and mechanical strains in the crystal. Both room temperature and low temperature Photoluminescence spectroscopy was used to measure the band energy properties of ZnO nanowires, Finally, Raman spectroscopy was used to characterize the incorporation of Li in ZnO nanowires and to characterize the effect of annealing or the nanowire quality.

4.3.2. Dopant Influences on The Nanowire Structure

Because of the ion radius difference, incorporation of extrinsic elements in ZnO nanowire crystal will cause a lattice mismatch, decreasing nanowire quality or, through interrupting the growth processes, destroying nanowire structure. Table 4.1 shows the radii of different ions, from which we can see that to substitute Zn atom for doping, Li has the radius closest to that of Zn atom, and this means fewest influences on the structure of the ZnO nanowires. In contrast, the radius difference between Zn and Ag or Al is very large, also proved by experimental observations. The ZnO nanowire structure is significantly affected and the growth of nanoplates resulted when the dopants are too large to fit in the lattice.

Table 4.1 radius of different ions

Ions	Zn^{2+}	Li^{+}	Na^{+}	Ag^{+}	Al^{3+}	O^{2-}	N^{3-}
Radius(pm)	74	76	116	129	67	140	146

Figure 4.3 shows SEM images of intrinsic, 200 % and 300 % Li doped ZnO nanowires, and Al, Ag doped ZnO nanowires. It was found that with the increase of the dopant amount, the deformation of ZnO nanowires becomes more pronounced. Al and Ag are more likely to destroy the nanowire structure of ZnO even at very low doping concentrations. As shown in Fig. 4.3, proper amount of Li incorporation can improve ZnO nanowire quality. Figure 4.3 (b) shows nanowires, grown by electrochemical deposition at 0.9 V electric potential, having better hexagonal shape of ZnO crystal on the top of nanowires, compared with (a) intrinsic nanowires. However, when the amount of impurity Li in the growth bath increases to 300 % of that of zinc ions, the nanowire structure of ZnO was disturbed, forming unshaped clusters. It was found in Figs. 4(d) and (e), due to the large radii difference between Al and Zn atoms, even when concentration of Al is 1 % of Zn in the growth solution, the nanowire structure of ZnO was influenced. In addition, some plates about 1 μm in diameter were formed resulting from the significant influence of Al in the fabrication of ZnO nanowires. As for co-doping with Al and Ag shown in Figs. 4.3 (f), (g) and (h), both Al and Ag will influence the nanowire growth of ZnO which make the deformation of nanowire structure even more significant. When both Al and Ag concentrations are 3 % of Zn in the growth solution, micrometer plates in micrometer are generated.

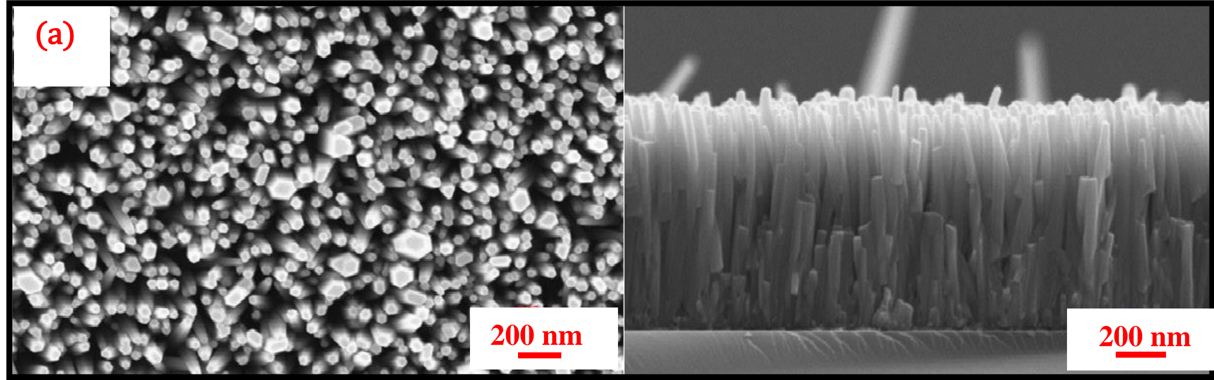
(a)
200 nm
200 nm

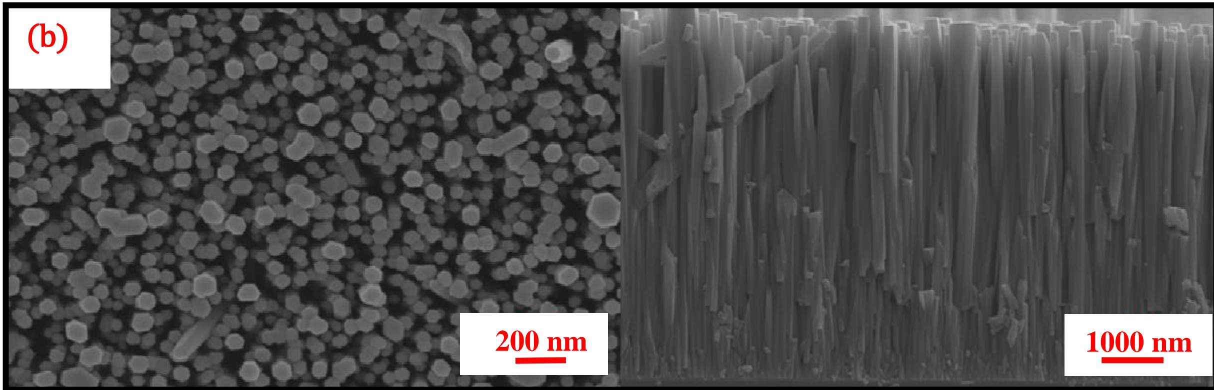
(b)
200 nm
1000 nm

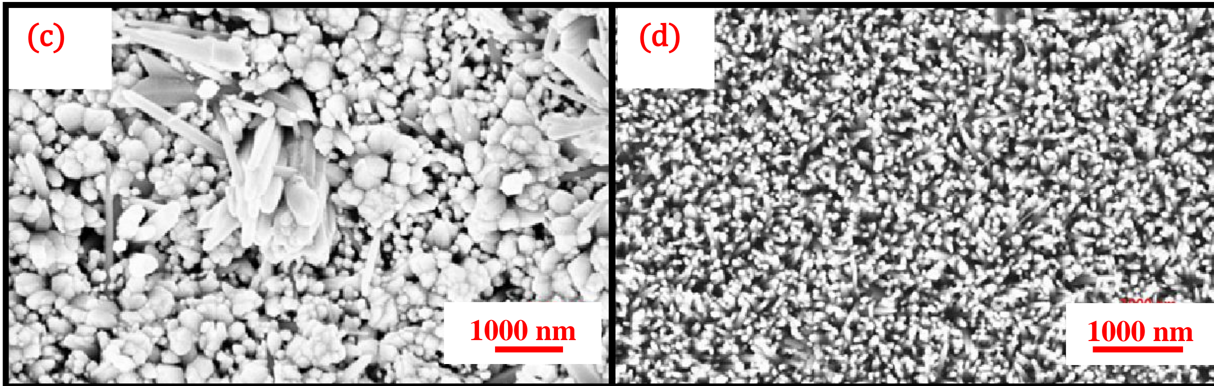
(c)
1000 nm
(d)
1000 nm

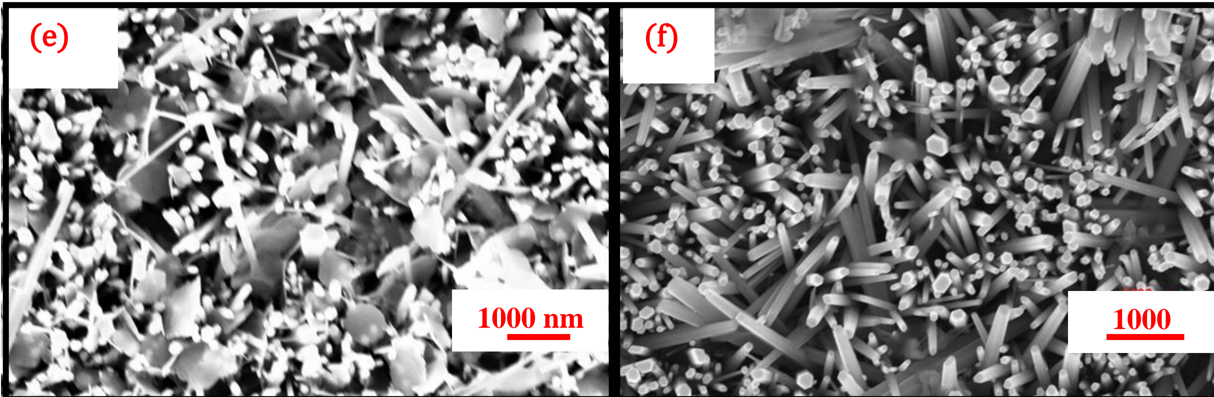
(e)
1000 nm
(f)
1000

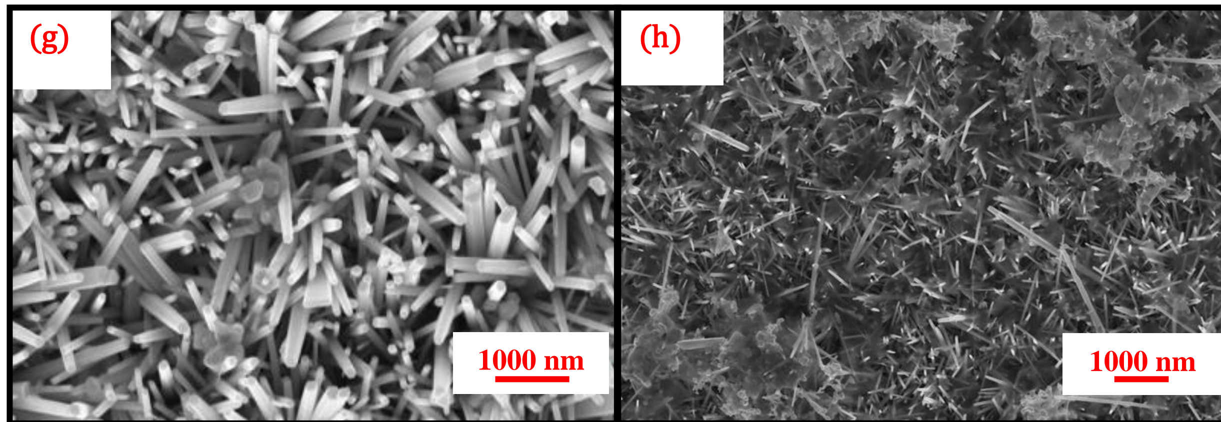

Figure 4.3.SEM images for (a) intrinsic ZnO nanowires, (b) 200 % Li doped, (c) 300 %Li doped, (d) 1 % Al doped, (e) 3 % Al doped, (f) 0.5 % Ag/Al co-doped, (g) 1 % Ag/Al co-doped, (h)3% Ag/Al co-doped ZnO nanowires.

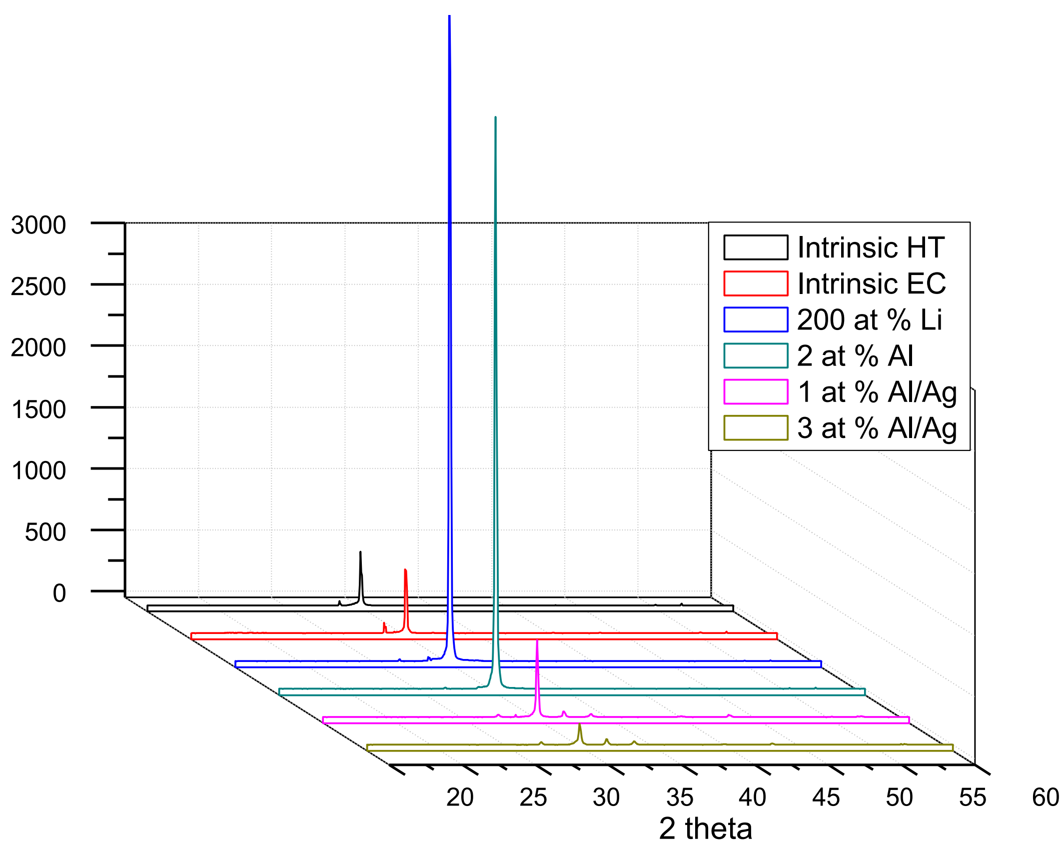

Figure 4.4 X-ray diffraction diagrams for intrinsic and doped ZnO nanowires with Li, Al and Al/Ag, through hydrothermal (HT) or electrochemical deposition method (EC).

Figure 4.4 show typical XRD spectra of intrinsic ZnO nanowires grown by the hydrothermal method (HT) without electric field applied and with electric field (EC), as well as nanowires doped with 200 % Li, 2 % Al, 1 % and 3 % Ag/Al through electrochemical deposition. For all samples, the main peaks are at 34.6^o (2θ) representing the growth along (002) plane of ZnO crystal, which means the nanowires growth along (002) plane is highly preferred. Also, the XRD shows well-oriented vertical ZnO nanowires with respect to the substrate. It is obvious that, (002) peaks for 200 % doped and 2 % Al doped ZnO nanowires have significantly higher intensity compared with other samples, which may be due to the high quality of the crystal structure with less defects or stain. However, refer to SEM images of Al doped ZnO nanowires, explanation for high (002) peaks for Al doped should be the long length of the nanowires. As observed from experiments, long nanowire growth time does favor high-quality crystal structure. Compare the rate of intensity of (100) peak located at 33.2^o and (002) peak, the 200 % doped nanowires has relatively lower intensity for (100) peak than intrinsic and Ag/Al co-doped nanowires, which suggests the ability of Li to improve nanowire quality, supporting the SEM characterization. Multiple XRD peaks for Ag/Al co-doped ZnO nanowires indicate significant multiple growth directions which also agrees well with the ZnO morphology characterized by SEM.

4.4. Post-growth Annealing

Post-growth annealing processes are wildly applied in materials science to improve material crystal structure quality so as optical and/or electrical properties

Post-growth annealing for ZnO nanowires has the following benefits:

- Post-growth annealing at high temperature allows lithium at interstitial sites in the ZnO crystal to migrate into the crystal lattice due to thermal diffusion, resulting in a perfect crystal periodicity.
- During post-growth annealing with oxygen, oxygen atoms can substitute oxygen vacancies suppressing the n-type property of ZnO nanowires.
- Post-growth annealing at high temperature can lead to immigration of atoms in ZnO crystal reducing intrinsic strain and defects.
- Post-growth annealing can reduce defect distribution in the structure of ZnO nanowires.

4.4.1 Process Conditions

In this study, post-growth annealing processes for intrinsic and doped ZnO nanowires were applied. Specifically, samples were annealed in AJA plasma sputtering deposition chamber at 500 ^{o}C for 30 minutes, and oxygen flow at the rate of 20 sccm was supplied. During the process, a vacuum of 5 mTorr was kept. A 10 minute ramp up was needed for the temperature to reach 500 ^{o}C, after which the system was maintained at 500 ^{o}C. Annealing influences was first examined by SEM; no obvious transitions of the ZnO nanowire structure were observed.

The photoluminescence measurements were done by Dr. Qi Wang in Prof. Zetian Mi's research group at McGill University.

4.4.2 Characterization and Discussion

After annealing, a blue shift of near the band edge emission was found through photoluminescence spectroscopy, as shown in Fig. 4.5 (a). In addition, the FWHM (full width at

half maximum intensity of a peak) increased after annealing, and new sharp peaks related to green emission due to oxygen vacancies cased defect states appeared.

Different models have been developed to explain the blue shift of energy band gap with post-growth annealing, while for different fabrication systems and annealing processes, the origin mechanism differs. One main mechanism is diffusion, so the interdiffusion of the atoms in the crystal causes the blue shift of band gap. For our cases, the shift should be due to atomic rearrangement of ZnO crystal and the reduction of oxygen vacancy defects. Before annealing, nanowires grown through solution bath will be featured with point defects including oxygen vacancies, Zn interstitials and hydrogen atoms merged in the crystal structure, and all of these lead to high local stains. This can be supported by XRD diagram for ZnO nanowires before and after annealing, as shown in Fig. 4.5 (b), after annealing, the (002) peak shift from 34.64^{o} to lower 2 theta position 34.55^{o}. As d-spacing is inversely propositional to 2 theta ($2d_{hkl}\sin\theta=\lambda$), so d-spacing is bigger after annealing. Smaller d-spacing is caused by local strains from defects. During post-growth annealing, the amount of defects, especially oxygen vacancies, generated in low temperature solution growth processes were reduced, as the movement of atoms in high temperature and the supplied oxygen will substitute the vacancies, therefore the crystal structure was improved as well as local strain released (leading to larger d-spacings). Sharper peaks of band edge emission and appearance of new emission peaks are also evidence of structure charge. This improvement of ZnO crystal structure also narrows the energy distribution of defect states, therefore, resulting in the sharp green emission peak, rather than the broad emission for nanowires before annealing.

Reconstruction of the ZnO nanostructure crystal can also be detected from Raman spectroscopy, as shown in Fig. 4.6. ZnO with the wurtzite structure has C_{6V} point group system, in which,

according to the group theory, active Raman vibration modes include E_2(low), E_2(high), A_1(LO), A_1(TO), E_1(LO) and E_1(TO). In addition, when the incident measuring incident light is normal to the sample surface, only E_2 modes and the A_1(LO) modes are observable, the others are hidden by the Raman selection rules [154]. Figure 4.6 (a) shows the Raman spectra of the intrinsic ZnO nanowires before and after annealing; the peak located around 300 cm^{-1} is caused by Si. A new peak at 433 cm^{-1} appears due to E_2^{high} mode of ZnO hexagonal structure. The appearance of E_2^{high} peak means improved hexagonal structure of ZnO suggesting the structure has structure re-crystalized and the concentration of oxygen vacancies was reduced by the high temperature anneal. Re-crystallization and elimination of oxygen vacancies also occur for Al and Li doped ZnO nanowires with the evidence that relatively high E_2^{high} mode peaks after annealing compared with that before annealing, as shown in Figs. 4.6 (b) and (c), respectively. These results from Raman spectroscopy are consistent with the SEM, PL and XRD analysis.

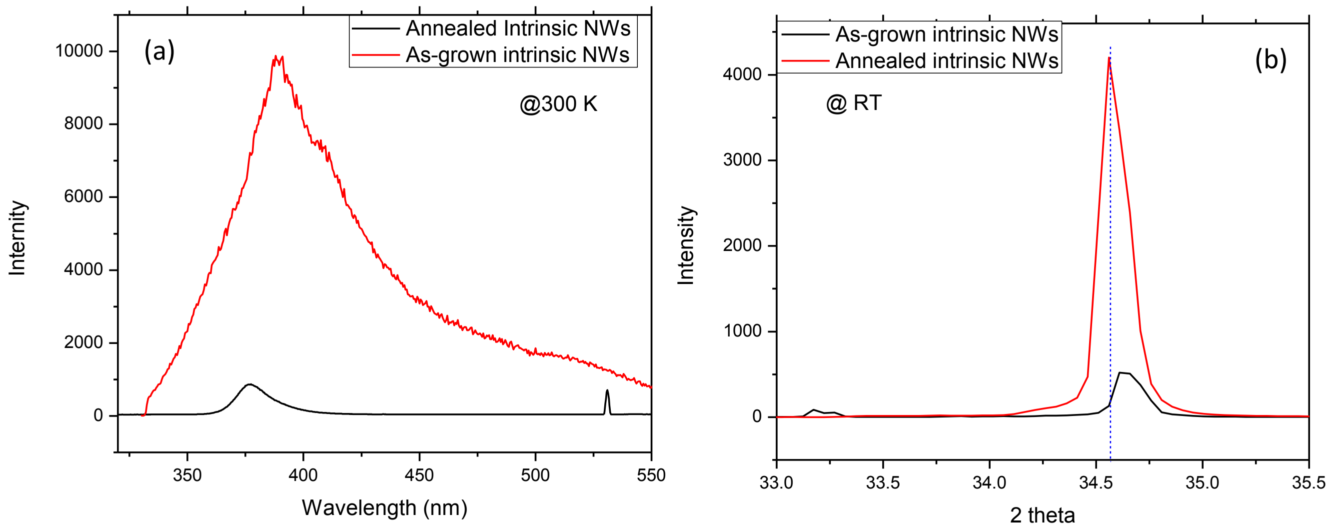

Figure 4.5 (a) Photoluminescence diagram for intrinsic ZnO nanowires with or without annealing processes at 500 ^{o}C for 30 minutes in the presence of O_2, measured at 300 K; (b) XRD diagram for intrinsic ZnO nanowires with or without annealing processes measured at room temperature.

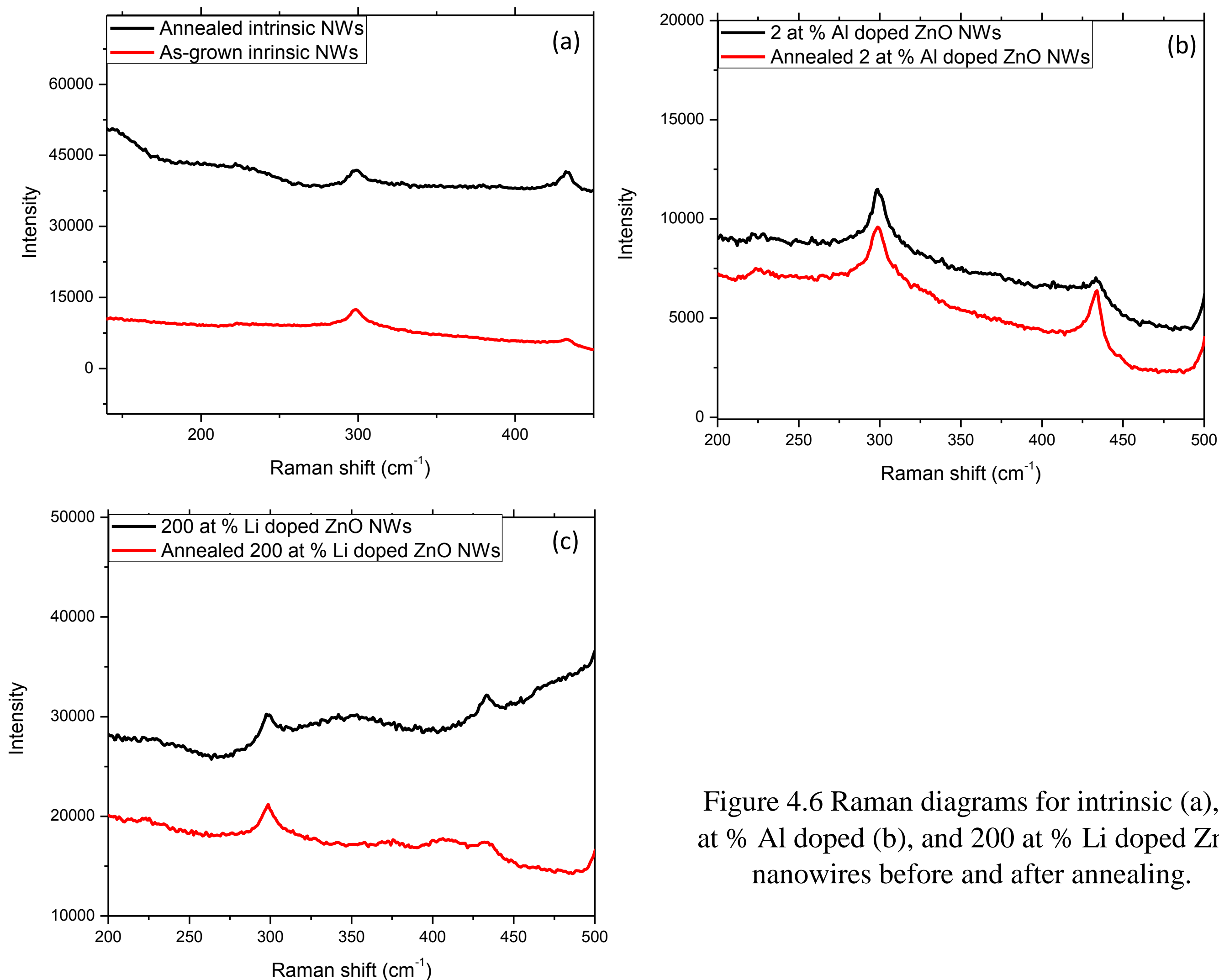

Figure 4.6 Raman diagrams for intrinsic (a), 2 at % Al doped (b), and 200 at % Li doped ZnO nanowires before and after annealing.

4.5. Photoluminescence of Li-doped ZnO nanowires

Energy band gap (E_g) and defect induced states of intrinsic and Li doped ZnO nanowires (Li-doped ZnO) are investigated by photoluminescence spectroscopy (PL) at room temperature and low temperature. The wavelength of the lase excitation was 266 nm (4.66 eV).

4.5.1. Emission Peaks

Figure 4.7 shows PL diagram for intrinsic ZnO nanowires and 50 %, 200 % doped nanowires tested at different temperature. For all measurements, there is a sharp peak located from 374.8 nm to 368.6 nm (or from 3.29 eV to 3.68 eV), which is due to the near band-edge emission of the ZnO semiconductor materials. Therefore, at room temperature, for as-grown intrinsic ZnO nanowires, the energy band gap is 3.29 eV. It is 3.30 eV for the 50 % Li sample and 3.29 eV for 200 % Li doped sample.

From Fig. 4.7, for all samples, it was observed that with the decrease of temperature from 300 K to 20 K, the band gap related emission peak moved to higher energy (blue shift). Therefore, energy band gap of ZnO decreases with the increase of temperature. This shift can be explained as the increase of thermal energy, the amplitude of the atomic vibration increases so as to increase the interatomic spacing. This effect is due to the linear coefficient of a material [155], where an increased interatomic spacing will decrease the potential felt by electrons so as to decrease the energy band gap. Similar trends occur when interatomic spacing is decreased by high compressive (or increased by tensile) stress, the band gap will increase (or decrease). These temperature dependence changes of band gap can be modeled by the following equation (3):

$$E_g(T) = E_g(0) - \frac{\alpha T^2}{T+\beta} \quad (3)$$

where $E_g(0)$, α and β are parameters to fit. These parameters for intrinsic, 50 % and 200 % Li doped ZnO nanowires are listed in the table below:

Table 2 fitting parameters for equations of temperature dependent band gap.

	Intrinsic	50 % Li doped	200 % Li doped
$E_g(0)$ (eV)	3.371	3.372	3.376
α (eV/K)	4.7×10^{-4}	1×10^{-3}	1×10^{-3}
β (K)	260	800	760

From the table we can inspect the influence of Li on ZnO band gap with the observation of big changes of parameter β (from 260 to 800 and 760) and α (one order of magnitude increase).

In addition to the near band-edge energy emission, there is another sharp peak located at the wavelength of 531 nm (2.34 eV), corresponding to green-light emission. Green emission obtained in the PL characterization is related to the oxygen vacancies caused n-type defect states, which has also been studied by Ajay Kushwaha and his colleagues [156]. Ionized oxygen vacancies act as trap states for recombination of electrons and holes.

As shown in Fig. 4.7, there is a doping dependent broad peak from 400 nm to 500 nm. The more impurities incorporated into the ZnO nanowires, the more mismatch of the crystal lattice. Incorporation of Li increases defects in ZnO crystal that leads to trap states in the band gap. Intensity of the broad peak increases with the decrease of temperature. This change can be understood when the temperature is sufficiently low, thermal energy cannot de-trap electrons from these defect states. If these trapped electrons recombine with holes radiatively, an emission will be detected. If they are de-trapped by thermal energy at high measurement temperature, electrons will then convert their energy by various vibrations to phonons. The broad peak demonstrates that defect states distribute in a broad energy range in the band gap. If these states

are close to the conduction band they can act as donor states and are radiative. If close to the valence band, they are called acceptor states. If they are close to neither conduction band nor valence band, they function as trap states in the band gap, which can cause tunneling current that cause current leakage in the study of conductivity property with different contacts as discussed in the next section.

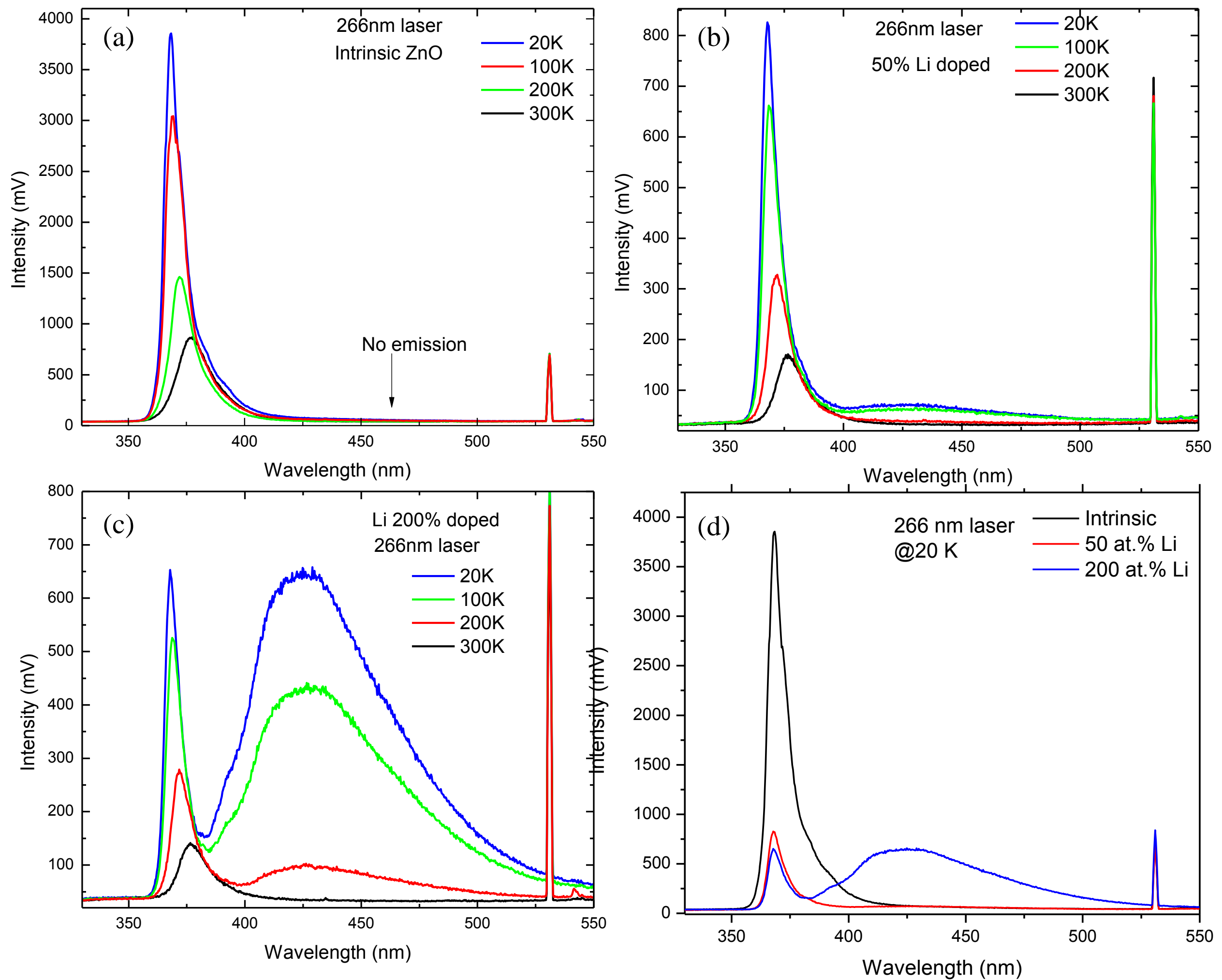

Figure 4.7 photoluminescence diagrams of Li doped and intrinsic ZnO nanowires measured at low and room temperature.

4.5.2. Band Energy Structure of Li-doped ZnO Nanowires

As expected, Li atoms will substitute Zn atoms in ZnO crystal acting as acceptors. For 200 % Li doped ZnO nanowires, using the PL diagram, measured at 20 K with 266 nm laser, we can calculate the energy level of the acceptor states (hypothetically). As shown in Fig. 4.8 (b), near band emission splits into two peaks: neutral donor-bound exciton peak (D^oX) and neutral acceptor-bound exciton peak (A^oX). And the broad green-emission peak (FA) is assigned to be free electron to acceptor transition peak. Therefore acceptor energy level can be expressed by the following equation (4):

$$E_A = E_g - E_{FA} + \frac{k_B T}{2} \quad (4)$$

where E_A is the acceptor energy, Eg the band gap of ZnO, k_B the Boltzmann constant, T the measurement temperature. At the temperature of 20 K, thermal energy is negligible. Therefore E_A can be obtained when take E_g = 3.37 eV, and E_{FA} =2.92 eV from Fig. 4.8 (a), so E_A = 450 meV. However, compared with other analyses for p-type ZnO nanowires with N-doped (170-200 meV), P-doped (127 meV), As doped (115-164 meV) [157, 158], indicates Li dopants lead to deep states in the band gap instead of acceptor states. Thus, as shown in the energy band level diagram of 200 % Li doped ZnO nanowires in Fig. 4.9, Li doped ZnO nanowires have wide distribution of defect states centered at 450 meV (deep level acceptor) with respect to the valence band. Meanwhile, oxygen vacancies induced donor states (about 1.03 eV away from conduction band, obtained from PL characterization) still exist contributing to n-type conductivity of ZnO nanowires. For shallow acceptor states, the emission peak of FA should be very close to near band edge emission.

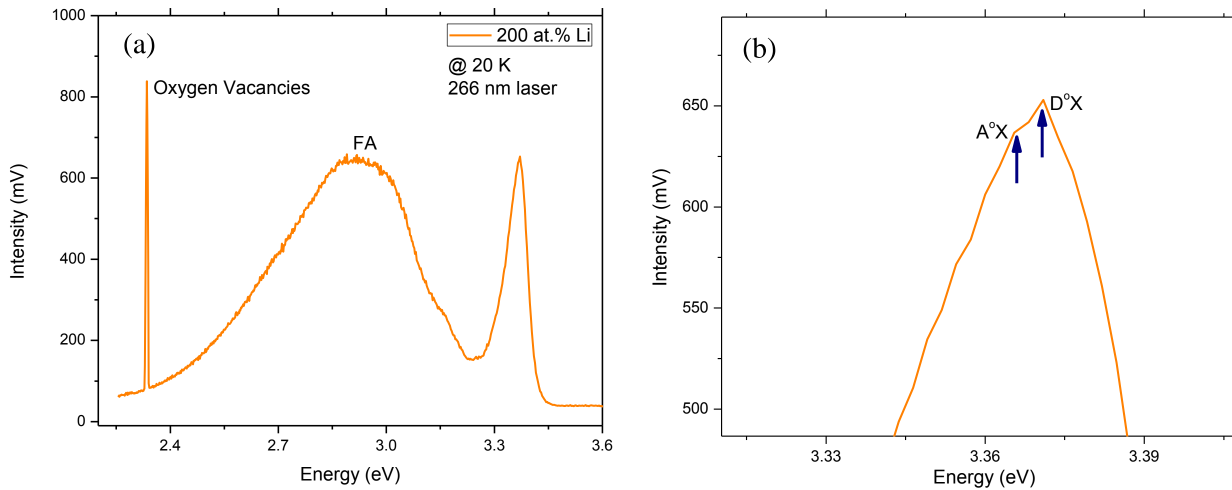

Figure 4.8 photoluminescence diagrams for 200 % Li doped ZnO nanowires (a), and (b) is the magnification of (a) in the band edge emission region.

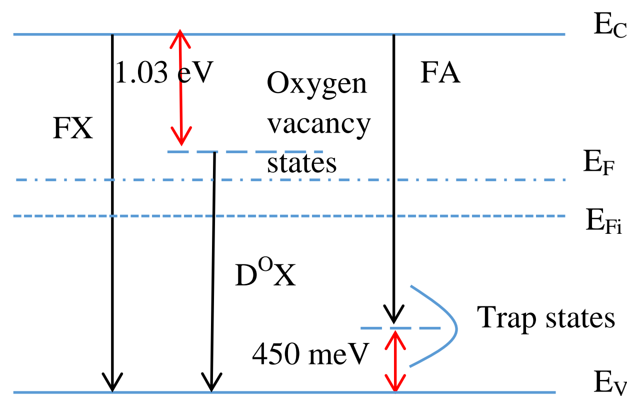

Figure 4.9 energy band diagram of Li doped ZnO nanowires. Arch figure represents the distribution of Li induced trap states; FX is free exciton transition; D^{O}X is neutral donor-bound exciton transition; FA is free electron to acceptor (actually trap states in this study) transition.

4.6. Electrical Characterization

Recently, ZnO nanowires have been of interest used in fabricating devices such as light emitting devices (LEDs), laser diodes, UV detectors and solar cells. High quality ZnO nanostructures

based homo-junctions have proven elusive as the difficulties of p-type ZnO nanowires. Conversely, interest has moved to the fabrication of hetero-junctions and Schottky contacts on n-type ZnO nanostructure to realize the fabrication of electronic devices. Schottky diodes are the simplest devices but with high technological importance. Furthermore, the understanding of Schottky-barrier formation on interfaces between metal and ZnO nanostructure is therefore of great interest. Thus, this subsection studies current-voltage property of different contacts between Li doped ZnO (Li-doped ZnO) nanowires and different metals: Al, Cr and Au, to investigate surface defects of nanowires and the energy barriers at interfaces.

4.6.1. Introduction to Contacts

Metal and semiconductor can form two categories of contacts: Ohmic and Schottky contacts. An Ohmic contact is a contact that has no barrier for the transfer of majority charge carriers from one material to another, i.e. there is no barrier for the current. Two ways are generally used to achieve an Ohmic contact. First, a semiconductor can be degenerately doped to form a tunneling contact; secondly, carefully choose a metal and semiconductor combination so the work functions of the metal ϕ_M and semiconductor ϕ_s match well to reduce the energy barrier between metal and semiconductor. For the first case, the condition for tunneling requires the depletion width on the semiconductor side less than 5 nm. Tunneling can then occurs in both directions, i.e. from metal to semiconductor and from semiconductor to metal. Therefore the approximate doping concentration is in the order of 10^{19}/cm^{-3}, which is a really easy value to achieve. For the second case, a good match of metal and semiconductor working function is that $\phi_M < \phi_s$ for n-type semiconductor and $\phi_M > \phi_s$ for p-type semiconductor. However, in this case, the Ohmic contact can only be achieved whenever there are no surface states in a semiconductor, which is

not easy and impossible for Li-doped ZnO nanowires in this study. Therefore, even for an n-type semiconductor, when $\phi_M < \phi_s$, Ohmic contact is formed, due to existing surface states, resistance to current flow still exists. In practice, surface states and metal and semiconductor work function are all taken into consideration. Surface states pins the Fermi level E_F at E_{CNL}. Surface states at the nanowire surface dominate the properties of the semiconductor. Some of the states are acceptor-like and may be neutral or negative, while others may be donor-like and may be neutral or positive. There is an energy level at which the dominant character of the interface states is neutral, i.e. the point energy level changes from donor-like to acceptor-like, and this energy level is labeled as E_{CNL} (This is quite similar with semiconductor/solution contact as discussed in chapter 2). When the density of surface states is high enough, it is able to pin the Fermi level at some level close to E_{CNL}.

Schottky contacts are very important in the realization of ZnO nanoelectronics. The formation of high quality rectifying contact is crucial for many optoelectronic applications and remains to be a challenge despite numerous recent investigations [159]. However, the influences of interface states, the surface morphology, hydroxide surface contamination, and subsurface defects prevent the realization of high quality Schottky contacts and affects electrical properties of devices [160]. In recent years, many investigations of Schottky contacts have been developed, but the main issues still remain to be the barrier height and ideality factors that are influenced by effects of asymmetric contacts, influences of interfacial layers, and/or surface states. Furthermore, nanomaterials like nanowires and nanorods have abundant surface states, which play very important roles in high-performance devices in optoelectronic, high temperature, high-frequency, and power applications. Schottky diodes are the simplest devices and also the most important, especially for applications as detectors, sensors and microwave diodes. Therefore, the

investigation of current-voltage (I-V) characteristics of Schottky contacts at room temperature is necessary. So this section will address current-voltage characteristics of Schottky contacts with nanowires using different contact metals. With nanomaterials, Schottky barrier height depends not only on the work function of metals, but also on the pinning of Fermi level caused by surface states, image-force lowering, field penetration, and the existence of an interfacial insulting layer, these influences mainly dominate the changes of current values at low bias by lowing Schottky barrier height. For nanomaterials, Schottky barrier is dominated by surface states, which has been investigated in reference [161] by changing measurement temperature.

This section will start from the view of studying contacts with different contact metals to explore Fermi level pinning phenomenon caused by surface states and applying tunneling mechanism to explain high current leakage at low bias.

4.6.2. Contact Fabrication Processes

Li doped ZnO nanowires were grown by previously discussed electrochemical deposition method on glass substrate pre-coated with conductive materials such as AZO and Cr. After growth processes, nanowires were rinsed by deionized water to remove debris and dried with an air gun. Annealing in vacuum at 500 ^{o}C with the presence of oxygen was applied for the relaxation and reconstruction of the ZnO crystals. The duration was 30 minutes. Before being coated with contacts, dielectric material PMMA was spin-coated on the top of ZnO nanowires. PMMA was deposited between nanowires to avoid any short-circuit, at the speed of 3000 rpm for 60 seconds, after which the sample was baked at 120 ^{o}C for 20 minutes. To ensure that no PMMA was on the top of the ZnO nanorods, oxygen plasma cleaning was performed. Al and Cr were coated through a magnetron sputtering deposition system, and Au was deposited via

thermal evaporation deposition technique. Depositions of metals were helped by Dr Czang-Ho Lee (Al and Cr) and Sibi Sutty (Au). Figure 4.10 depicts the schematic diagram of metal/Li-doped ZnO nanowire contacts. Scanning electron microscopy was used to characterize the morphology of as grown and coated ZnO nanowires and I-V characteristics were performed with a current-voltage probe station.

As shown in Figure 4.11, as-grown ZnO nanowires were found to be aligned vertically and distributed uniformly on the substrate. The inset shows nanowires coated with PMMA after soft baking and plasma etching.

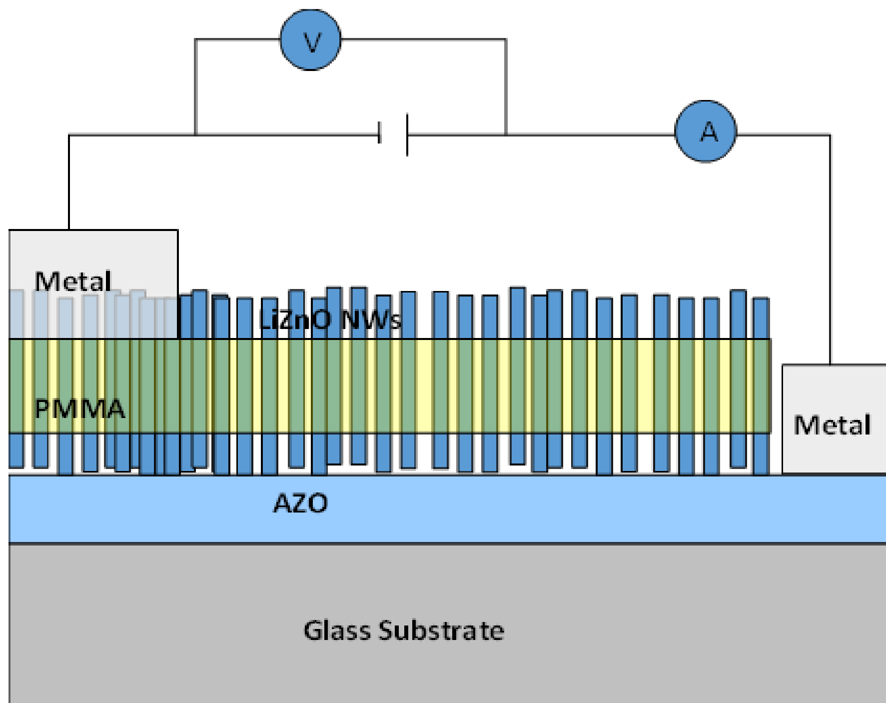

Figure 4.10 a schematic diagram of metal/Li-doped ZnO nanowire contacts

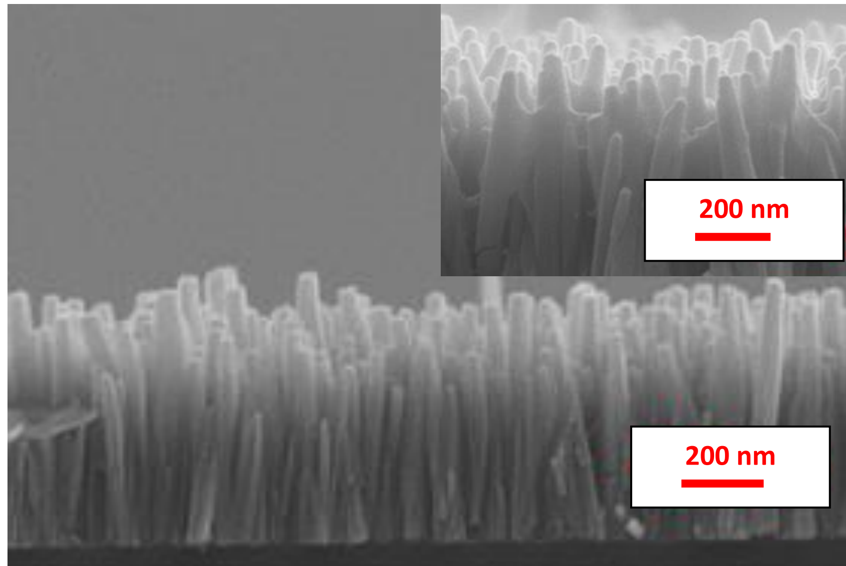

Figure 4.11 SEM images of as-grown ZnO nanowires with the presence of electric field at an electrical potential of -0.8 V. The inset shows nanowires coated with PMMA after soft baking and plasma etching.

4.6.3. I-V Characterization and Band Energy Structure

Generally, total current measured in I-V characteristics is related to both a thermionic emission and tunneling component. Thermionic emission is the temperature dependent flow of charge carriers from a surface or over a potential-energy barrier. This occurs because thermal energy provides charge with enough energy to overcome a binding potential, which is also known as working function of the metal. If we ignore the tunneling component contributing to the total current, the current caused by thermionic emission can be expressed in the discussed equations of this section.

Figure 4.12 shows the I-V characterization measured using contacts formed with Cr, Al (a) and Au (a) and (b), from which we can see a partly linear curve at high bias and nonlinear curve at

relative low bias. Current at very low bias is due to electron transfer over energy barrier through a tunneling mechanism, when the applied voltage increases, the energy barrier decreases, suppressed by the electric field, and therefore series resistance dominate the current flow.

Figure 4.13 shows the band-energy diagrams of metal/Li-doped ZnO NW contacts before and after contacting at an ideal situation without surface state influences. As shown in diagram (a), the work functions for Al and Cr are 4.2 eV and 4.4 eV, respectively, which is lower than ZnO electron affinity $e\chi$ of 4.5 eV, thus the Fermi energy E_F of ZnO must be larger than working functions of Al and Cr. Therefore, the energy level diagram after contact should be Fig. 4.13 (b), in which, if electrons flow from Li-doped ZnO to metal, there are no energy barriers for the transition, and this contact acts as an Ohmic contact. However, if electrons flow from metal to semiconductor Li-doped ZnO, this contact is a Schottky contact and electrons need enough bias to overcome the energy barrier carrying charges for conduction. I-V diagram as illustrated in Fig. 4.12 (a) shows properties of current flow from Li-doped ZnO to metal. However, working function of Au is 5.1 eV that is larger than electron affinity of Li-doped ZnO but no enough supporting information to determine whether it is larger than Fermi level of Li-doped ZnO (maybe 5.53 eV $< e\phi_s <$ 6.19 eV, from PL characterization). Thus, after contact, the energy barrier should be (c) when metal $\phi_M < \phi_S$ or (d) when $\phi_M > \phi_S$. Energy barriers $e\phi_{Bn}$ for (b) and (c) are the same as E_C-E_{Fs}. In comparison, in (d), the energy barrier is E_M-E_{FS} + $(E_C$-$E_{FS})$, which is $(E_M$-$E_{FS})$ higher than that for (b) and (c), correspondingly, thus the current should be smaller at the same biases. Figure 4.12 shows I-V diagram for Al, Cr or Au/Li-doped ZnO contact when under electric field with metal negatively charged and current for Au/Li-doped ZnO is much lower than the others; therefore energy diagram of Au/Li-doped ZnO can be identified to be figure 4.13 (d) with $\phi_M > \phi_S$.

Current measured with Cr/Li-doped ZnO contact is slightly larger than that measured with Al/Li-doped ZnO contact that should be attributed to experimental errors. In addition, in this study, energy barriers in contact between metal and AZO (Al doped ZnO) and contact between AZO and Li-doped ZnO are negligible due to the degenerated AZO semiconductor, compared with barriers in the metal/Li-doped ZnO contacts.

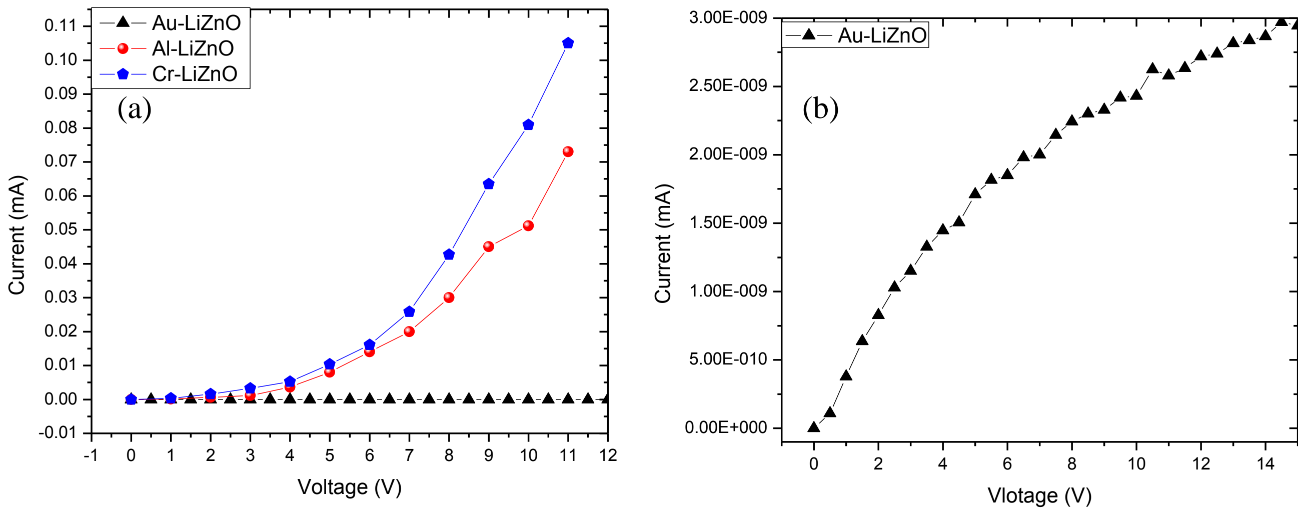

Figure 4.12 Current versus voltage diagram of contacts between Cr, Al and Au with Li-doped ZnO nanowires.

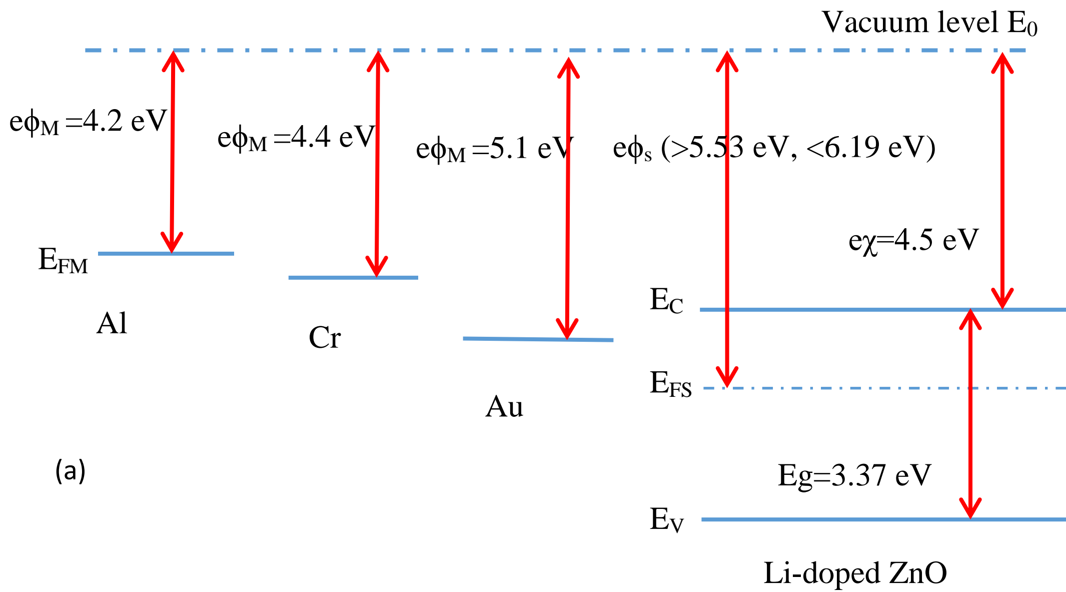

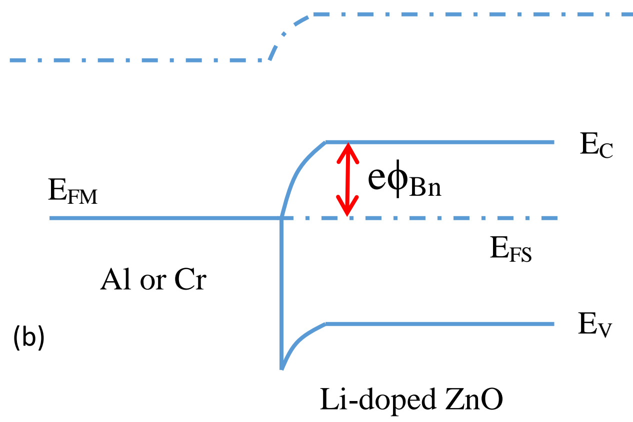
E_C
E_{FM}
$e\phi_{Bn}$
E_{FS}
Al or Cr
E_V
(b)
Li-doped ZnO

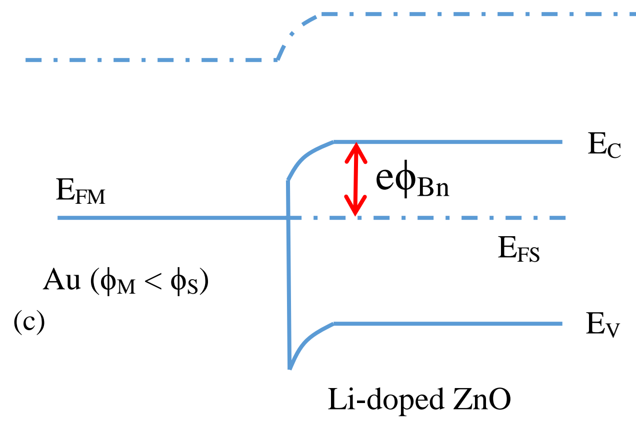
E_C
E_{FM}
$e\phi_{Bn}$
E_{FS}
Au ($\phi_M < \phi_S$)
(c)
E_V
Li-doped ZnO

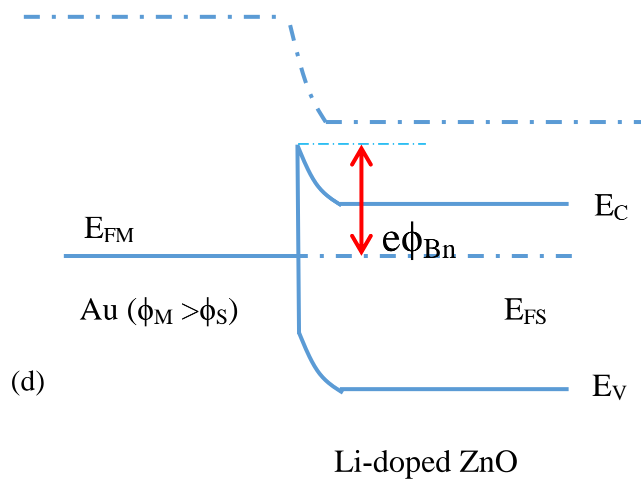
E_C
E_{FM}
$e\phi_{Bn}$
Au ($\phi_M > \phi_S$)
E_{FS}
(d)
E_V
Li-doped ZnO

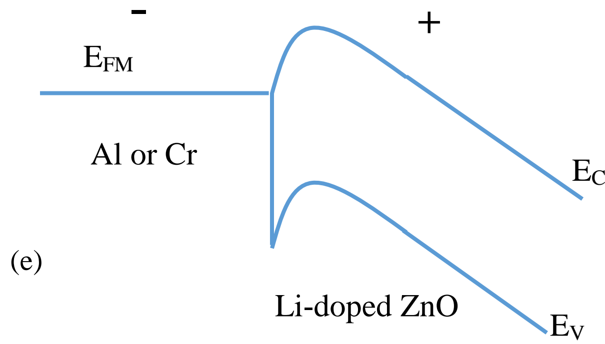

Figurer 4.13 Schematic diagrams of energy band. Before contacting (a); (b) after contacting formed Al or Cr/ Li-doped ZnO contacts, Possible Au/Li-doped ZnO contact diagram (c) and (d) formed when $\phi_M < \phi_S$ and $\phi_M > \phi_S$, respectively; and (e) is Al or Cr / Li-doped ZnO contact biased with electric field (metal is negative charged).

4.6.4. Model Fitting and Analysis

However, the above described situations are ideal metal-semiconductor contact models without the consideration of surface states. In actual practice, especially for ZnO nanowires grown in solution bath at low temperature, surface states or defects often dominate observed current characteristics. Therefore, there are many trap states in ZnO nanowires and they are spread across energy band gap as discussed above. Some of these states are acceptor-like and may be neutral or negative and others are donor-like and may be neutral or positive. The energy level at which the dominant character of the interface states changes from donor-like to acceptor-like is called charge neutrality level E_{CNL}. As a result, a high density of energy states in the band gap at the metal-semiconductor interface pins E_f to a narrow range near E_{CNL}. For instance, for Si, it was found that $E_{CNL} \approx E_v + 1/3E_g$, $\phi_{Bn} \approx 2/3\ E_g$ and $V_{bi} \approx 2/3E_g-(E_C-E_F)$. In practice, predicting E_{CNL} is very difficult theoretically (which depends on the technology), ϕ_B is usually measured experimentally. Few data about ZnO Fermi level pinning has been reported.

Without the consideration of tunneling induced current, thermionic emission dominated current can be expressed in equation (5) as a function of voltage and temperature.

$$I = I_S[\exp\left(\frac{q(V-IR_S)}{nkT}\right) - 1] \quad (5)$$

Where q is the charge of an electron, I_s the saturated current, V the voltage applied, R_s the resistance, n ideality factor, k Plank constant and T the temperature. Ideality factor can be obtained from the slope of the plot of *ln(I)* vs. *V*. Through extrapolating linear part of the *ln(I)* vs. *V* curve to zero applied voltage the saturation current I_s can be calculated.

I_s can be expressed in the following equation (6):

$$I_s = AA^{*}\exp(-\frac{q\phi_{Bn}}{kT}) \quad (6)$$

Where A^* is effective Richardson constant, A the diode area, ϕ_{Bn} the barrier height. For an ideal diode, ideality factor n should be equal to 1. For ZnO nanowires based contacts, n deviates from 1, influenced by resistance and surface states. In addition, the bottom contact material, Al doped ZnO thin film, will lead to inherent difficulties, which results in the considerable resistance resulting in a voltage drop across the junction. All of these will cause an increase of the ideality factor n and the calculated barrier height will also deviate from its real height.

Figure 4.14 shows linear fits of ln(I)-V characteristics using equation (7) derived from equation (5):

$$\ln(I) = \ln(I_S) + \frac{qV}{nkT} \quad (7)$$

for Al and Cr/Li-doped ZnO contacts; Table 3 shows parameters for the simulation results. From Table 4.3, we can see the high value of ideality factor n, which are 5.75, 7.13 and 18.43 for Al,

Cr and Au/Li-doped ZnO contacts, respectively. I_s (Al) is 3.83×10^{-8} mA, while it is 2.75×10^{-9} mA for I_s (Cr) and 6.46×10^{-22} mA for I_s (Au). Large deviation of ideality factors form 1 further proves the poor contact quality and significant influences of surface states of ZnO nanostructures. In contrast, even higher ideal factor for Au/Li-doped nanowires, indicating bad contact behavior that suggests more significant influences of surface defects on high energy barrier contacts.

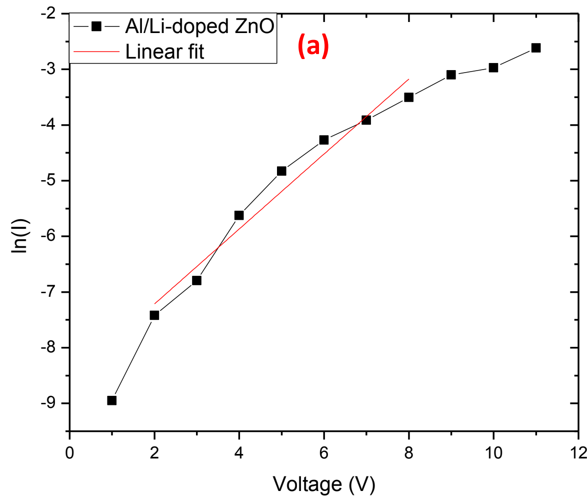

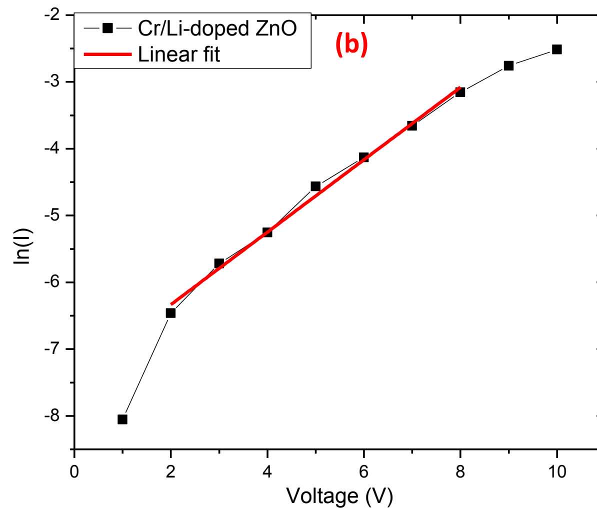

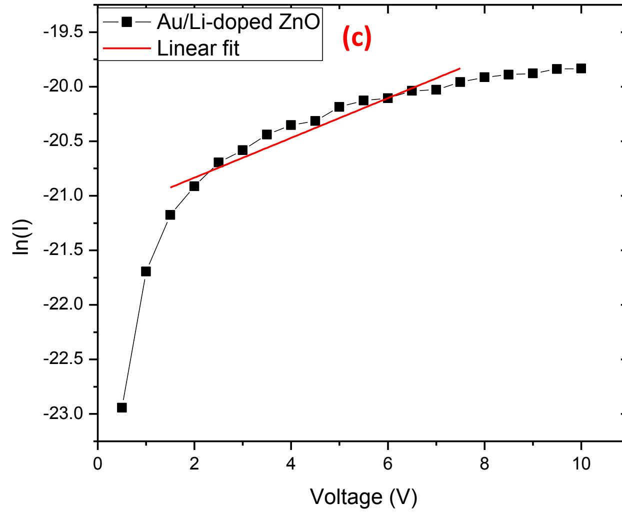

Figure 4.14 original and simulated I-V characteristics of Al (a), Cr (b) and Au (c)/Li-doped ZnO contacts

Table 4.3 Simulation parameters for I-V characteristics of different metal/Li-doped ZnO contacts.

Contact meatl	$I_s\,(mA)$	n
Al	3.83×10^{-8}	5.75
Cr	2.75×10^{-9}	7.13
Au	6.46×10^{-22}	18.43

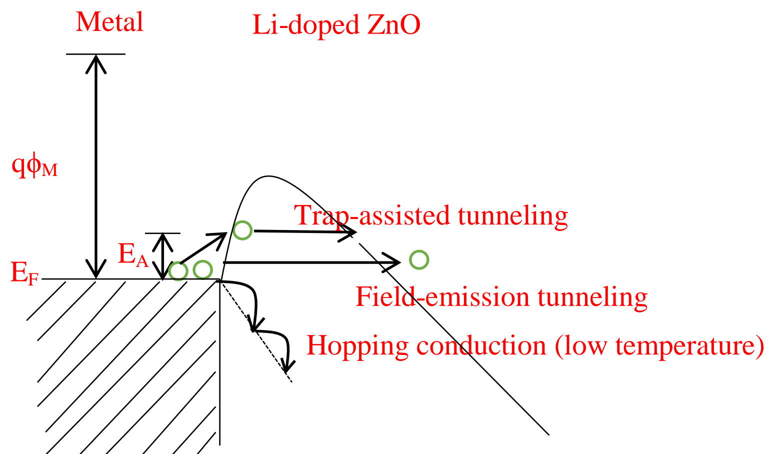

Figure 4.15 a schematic diagram of possible tunneling conduction mechanisms responsible for Al and Cr/Li-doped ZnO contacts under low bias.

In addition, surface states may also induce significant leakage current at low bias. For nanomaterials based contacts, there are two dominating mechanisms responsible for current leakage. Firstly, field emission tunneling, which is pronounced at room temperature with current from metal to semiconductor; secondly, dislocation or interface surface states induced trap-assisted one-dimensional variable-range-hopping conduction. Figure 4.15 shows the schematic diagram of the above discussed tunneling conduction mechanism. In the model of trap-assisted tunneling conduction, electrons in metals could be thermally activated to a trap state at the metal semiconductor interface and then tunnel into the semiconductor with the help of the electric field.

According to literature [162], due to surface defects such as oxygen vacancies, ZnO nanomaterials have many donors distributed in the surface; at sufficiently low temperature, most free electrons will be captured by donors. As a result, electrons can hop directly from one donor to another donor and free-electron band conduction will become less important. Hopping conduction is very important for devices acting as sensors used in extremely low temperature when band conduction decreases significantly and hopping conduction dominate the current. In hopping conduction, electron will jump from one occupied donor to an empty one, which means the concentration of empty donors is very important. Hopping probability between impurity sites governs hopping conductivity.

To summarize, large current leakage at low bias is mainly contributed by surface defects related trap-assisted tunneling and field emission tunneling. If tested at low temperature, hopping tunneling may dominate the current leakage. Further research is necessary to discover surface states induced current leakage of metal/Li-doped ZnO contacts.

4.7. Conclusions

This chapter introduces backgrounds and theories of doping semiconductor materials. Specifically, ZnO crystal structure was analyzed from the view of electron orbit hybridization, as well as doping mechanism of ZnO. Experimentally, n- and p-type ZnO nanowires were studied using dopants Al, Ag/Al and Li. SEM and XRD analysis shows dopants of Al and Ag/Al have critically influenced ZnO nanowire structure, while Li can improve quality of ZnO nanowire structure with a given concentration. Band energy level and defect states of intrinsic and doped ZnO nanowires were studied by PL characterization, and it was found that band gap of intrinsic and Li doped ZnO nanowires is 3.29 eV, closed to bulk ZnO semiconductor. Furthermore, band energy diagram of Li doped ZnO nanowire was achieved based on PL analysis, from which we found Li doped ZnO nanowire has wide distribution of defect states centered at 450 meV (deep level acceptor) with respect to valence band. Meanwhile, oxygen vacancies induced donor states still exist contributing to n-type conductivity of ZnO nanowire. Donor energy and acceptor energy level were also calculated.

Post-growth annealing process caused blue shift of near band edge emission was observed and explained through mechanisms of crystal rearrangement and elimination of oxygen vacancies. Conductivity of Li doped nanowires was also studied by current-voltage measurement through different contacts: Al, Cr and Au. No significant current was gained for Au/Li-doped ZnO contact because of the higher energy barrier. However, similar current property was measured for Al or Cr/Li-doped ZnO contacts; while high ideality factors of 5.75 and 7.13 were due to the high concentration of surface states. At last, surface defects induced trap-assisted tunneling and electric field-emission tunneling conductivity, as well as hopping tunneling current was discussed.

Chapter 5

Conclusions for Completed Studies

The aim to better understand ZnO semiconductors for applications in electronic, optoelectronic, electromechanical and electrochemical devices, was studied through electrochemical deposition of ZnO nanowire, doping and conductivity of ZnO nanowires, and characterization of the optical, electrical properties of ZnO thin film.

As for electrochemical deposition of the ZnO nanowires, this thesis first compares a hydrothermal fabrication technique without applying electric field through analyzing influences of the growth parameters to realize optimized conditions for the desired nanowire structure. In comparison, electrochemical deposition was found to result in higher quality ZnO nanowires with higher growth rate. Possible mechanisms were proposed for electrochemical deposition and doping by introducing the study of interface science and a charge transfer model. To have better understanding and control of electrochemical deposition, explicit efforts should focus on the study of ion effects, the semiconductor/solution contact model, nucleation mechanism and monitoring electric field through voltage or current. Conductivity and energy states of as-grown or doped ZnO nanowires where engineered by the growth parameters.

For the study of doping ZnO nanowires and conductivity characterization, this thesis firstly tried to dope p-type ZnO nanowires with electrochemical deposition technique that with much simpler and cheaper fabrication equipment compared with others, and interpreted the energy band diagram of Li doped ZnO nanowires, emphasizing defect states resulting from oxygen vacancies and Li incorporation, through photoluminescence properties. Li dopants turned out to be deep level acceptor (or trap) states in the band gap. In addition, Al, Cr or Au/Li-doped ZnO contacts

were formed to measure conductivity of Li-doped ZnO nanowires, through simulation, large ideality factors and large leakage current at low bias was formed due to surface states and its related tunneling mechanisms. Realization of p-type conductivity of ZnO still needs more efforts such as different dopants and annealing processes, and better manipulation of contact fabrication will be necessary for future studies.

However, core issues in controlling the ZnO nanowire semiconductor materials quality were determined. Fundamental knowledge of physical properties of ZnO nanowire should be addressed for their wide applications as sensors, field emitters, light-emitting diodes, photocatalysts, nanogenerators, and nanopizotronics. Near-term research of ZnO nanowires should focus on the following. 1. Complete understanding of growth kinetic, a high level of defects are formed in ZnO crystals due to low temperature growth processes at rather complex environments consisting of many molecules and ions. To improve the crystal quality, we can choose proper electric field potential, optimized growth parameters and post-growth annealing at high temperature. 2. Morphologically, structurally, and dimensionally controlled synthesis keep be the intensive research projects, and this relies on the above structure controlled growth. 3. Realization of p-type conductivity of ZnO nanowires, especially for the case of solution based low temperature growth condition, group V and/or I doping is feasible but very challenging. For electrochemical deposition, precise control of applied electric field, through adjusting current and voltage, and better understanding of ion immigration rate influences are very important. 4. ZnO nanowire based 1-D nano-electronic devices. This can be achieved by using advanced lithography techniques or other deposition and etching techniques.

For specific lab experimental researches, for example, the following are very interesting: First, grow long and removable nanowires and transfer them to a second substrate for nanoelectronic

fabrication. Secondly, nanowire growth on patterned seed layer or grow patterned ZnO nanowires on large scale substrates. Thirdly, devices based on piezoelectricity of ZnO semiconductor materials, which are realizable with low-temperature grown nanowires on original substrates.

Hopefully, this project is helpful for future ZnO materials related research.

References:

1. K.L. Chopra, S. Major, D.K. Pandya, Thin Solid Films 102, 1–46 (1982)
2. T. Minami, H. Sato, K. Ohashi, T. Tomofuji, S. Takata, J. Cryst. Growth 117, 370–374 (1992)
3. Brubaker DG, Fuller ML (1945) J Appl Phys 16:128
4. Klingshirn C, Hauschild R, Priller H, Zeller J, Decker M, Kalt H. Adv Spectrosc Lasers Sens 231:277 (2006)
5. Ozgur, U.; Alivov, Y. I.; Liu, C.; Teke, A.; Reshchikov, M. A.; Dogan, S.; Avrutin, V.; Cho, S. J.; Morkoc, H. J. Appl. Phys. 2005, 98, 041301.
6. Look, D. C. Mat. Sci. Eng. B-.Adv. 2001, 80, 383–387
7. Heo, Y. W.; Norton, D. P.; Tien, L. C.; Kwon, Y.; Kang, B. S.; Ren, F.; Pearton, S. J.; LaRoche, J. R. Mat. Sci. Eng. R 2004, 47, 1–47.
8. Yi, G. C.; Wang, C. R.; Park, W. I. Semicond. Sci. Technol. 2005, 20, S22–S34.
9. Wang, Z. L. J. Nanosci. Nanotechnol. 2008, 8, 27–55.
10. Wang, Z. L. ACS Nano 2008, 2, 1987–1992.
11. Wang, Z. L. Mat. Sci. Eng. R 2009, 64, 33–71.
12. Wang, Z. L. Chinese Sci. Bull. 2009, 54, 4021–4034.
13. Law, M.; Greene, L. E.; Johnson, J. C.; Saykally, R.; Yang, P. D. Nat. Mater. 2005, 4, 455–459.
14. Levy-Clement, C.; Tena-Zaera, R.; Ryan, M. A.; Katty, A.; Hodes, G. Adv. Mater. 2005, 17, 1512–1515.
15. Weintraub, B.; Wei, Y. G.; Wang, Z. L. Angew. Chem. Int. Ed. 2009, 48, 8981–8985.
16. Wei, Y. G.; Xu, C.; Xu, S.; Li, C.; Wu, W. Z.; Wang, Z. L. Nano Lett. 2010, 10, 2092–2096
17. Mao, D. S.; Wang, X.; Li, W.; Liu, X. H.; Li, Q.; Xu, J. F. J. Vac. Sci. Technol. B 2002, 20, 278–281.
18. Zhu, Y. W.; Zhang, H. Z.; Sun, X. C.; Feng, S. Q.; Xu, J.; Zhao, Q.; Xiang, B.; Wang, R. M.; Yu, D. P. Appl. Phys. Lett. 2003, 83, 144–146.
19. Wang, W. Z.; Zeng, B. Q.; Yang, J.; Poudel, B.; Huang, J. Y.; Naughton, M. J.; Ren, Z. F. Adv. Mater. 2006, 18, 3275–3278
20. Wei, T. Y.; Yeh, P. H.; Lu, S. Y.; Wang, Z. L. J. Am. Chem. Soc. 2009, 131, 17690–17695.

21. Yeh, P. H.; Li, Z.; Wang, Z. L. Schottky-gated probe-free ZnO nanowire biosensor. Adv. Mater. 2009, 21, 4975–4978.
22. Zhou, J.; Gu, Y. D.; Hu, Y. F.; Mai, W. J.; Yeh, P. H.; Bao, G.; Sood, A. K.; Polla, D. L.; Wang, Z. L. Appl. Phys. Lett. 2009, 94, 191103.
23. Huang, M. H.; Mao, S.; Feick, H.; Yan, H. Q.; Wu, Y. Y.; Kind, H.; Weber, E.; Russo, R.; Yang, P. D. Science 2001, 292, 1897–1899.
24. Govender, K.; Boyle, D. S.; O'Brien, P.; Binks, D.; West, D.; Coleman, D. Adv. Mater. 2002, 14, 1221–1224
25. Park, W. I.; Yi, G. C. Adv. Mater. 2004, 16, 87–90.
26. Wang, Z. L.; Song, J. H. Science 2006, 312, 242–246.
27. Wang, X. D.; Song, J. H.; Liu, J.; Wang, Z. L. Science 2007, 316, 102–105.
28. Yang, R. S.; Qin, Y.; Dai, L. M.; Wang, Z. L. 2009, 4, 34–39.
29. Wang, Z. L. Mater.Today 2007, 10, 20–28.
30. Wang, Z. L. Adv. Mater. 2007, 19, 889– 892.
31. Wang, Z. L. Adv. Funct. Mater. 2008, 18, 3553–3567.
32. Leung V, K o F Polym Adv Technol 22:350 (2011).
33. Nambiar S, Yeow JTW Biosens Bioelectron 26:1825 (2011).
34. Castro Neto AH, Guinea F, Peres NMR, Novoselov KS, Geim AK (2009) Rev Modern Phys 81:109.
35. Chen XM, Wu GH, Jiang YQ, Wang YR, Chen X (2011) Analyst 136:4631.
36. Artiles MS, Rout CS, Fisher TS (2011) Adv Drug Deliv Rev 63:1352.
37. Geim AK (2011) Rev Mod Phys 83:851.
38. Jorge L. Gomez • Onur Tigli, J Mater Sci (2013) 48:612–624
39. Laudise, R. A.; Ballman, A. A. J. Phys. Chem. 1960, 64, 688–691.
40. Verges, M. A.; Mifsud, A.; Serna, C. J. J. Chem. Soc., Faraday Trans. 1990, 86, 959–963.
41. Vayssieres, L.; Keis, K.; Lindquist, S. E.; Hagfeldt, A. J. Phys. Chem. B 2001, 105, 3350–3352.
42. Heo, Y. W.; Varadarajan, V.; Kaufman, M.; Kim, K.; Norton, D. P.; Ren, F.; Fleming, P. H. Appl. Phys. Lett. 2002, 81, 3046–3048.
43. Chiou, W. T.; Wu, W. Y.; Ting, J. M. Diam. Relat. Mater. 2003, 12, 1841–1844.
44. Xu, C. K.; Xu, G. D.; Liu, Y. K.; Wang, G. H. Solid State Commun. 2002, 122, 175–179

45. Pan, Z. W.; Dai, Z. R.; Wang, Z. L. Nanobelts of semiconducting oxides. Science 2001, 291, 1947–1949.
46. Huang, M. H.; Wu, Y. Y.; Feick, H.; Tran, N.; Weber, E.; Yang, P. D. Adv. Mater. 2001, 13, 113–116.
47. Yao, B. D.; Chan, Y. F.; Wang, N. Appl. Phys. Lett. 2002, 81, 757–759.
48. Park, W. I.; Yi, G. C.; Kim, M. Y.; Pennycook, S. J. Adv. Mater. 2002, 14, 1841–1843.
49. Park, W. I.; Kim, D. H.; Jung, S. W.; Yi, G. C. Appl. Phys. Lett. 2002, 80, 4232–4234.
50. Yuan, H.; Zhang, Y. J. Cryst. Growth 2004, 263, 119–124.
51. Sun, Y.; Fuge, G. M.; Ashfold, M. N. R. Chem. Phys. Lett. 2004, 396, 21–26.
52. Hong, J. I.; Bae, J.; Wang, Z. L.; Snyder, R. L. Nanotechnology 2009, 20, 085609.
53. Chiou, W. T.; Wu, W. Y.; Ting, J. M. Diam. Relat. Mater. 2003, 12, 1841–1844.
54. Lin, D. D.; Pan, W.; Wu, H. J. Am. Ceram. Soc. 2007, 90, 71–76.
55. Lin, D.; Wu, H.; Pan, W. Adv. Mater. 2007, 19, 3968–3972.
56. Sui, X. M.; Shao, C. L.; Liu, Y. C. Appl. Phys. Lett. 2005, 87, 113115.
57. Wu, J. J.; Wen, H. I.; Tseng, C. H.; Liu, S. C. Adv. Funct. Mater. 2004, 14, 806–810.
58. Zhang, H.; Yang, D. R.; Ma, X. Y.; Du, N.; Wu, J. B.; Que, D. L. J. Phys. Chem. B 2006, 110, 827–830.
59. Chang, P. C.; Lu, J. G. IEEE T. Electron Dev. 2008, 55, 2977–2987.
60. Xu, S.; Wei, Y.; Kirkham, M.; Liu, J.; Mai, W.; Davidovic, D.; Snyder, R. L.; Wang, Z. L. J. Am. Chem. Soc. 2008, 130, 14958–14959.
61. Govender, K.; Boyle, D. S.; Kenway, P. B.; O'Brien, P. J. Mater. Chem. 2004, 14, 2575–2591.
62. Xu, S.; Adiga, N.; Ba, S.; Dasgupta, T.; Wu, C. F. J.; Wang, Z. L. ACS Nano 2009, 3, 1803–1812.
63. Vayssieres, L. AdV. Mater. 2003, 15, 464. (15)
64. Greene, L. E.; Law, M.; Goldberger, J.; Kim, F.; Johnson, J. C.; Zhang, Y. F.; Saykally, R. J.; Yang, P. D. Angew. Chem., Int. Ed. 2003, 42, 3031.
65. Tian, Z. R.; Voigt, J. A.; Liu, J.; Mckenzie, B.; Mcdermott, M. J.; Rodriguez, M. A.; Konishi, H.; Xu, H. F. Nat. Mater. 2003, 2, 821.
66. Cui, J. B.; Daglian, C. P.; Gibson, U. J.; Puesche, R.; Geithner, P.; Ley, L. J. Appl. Phys. 2005, 97, 044315.

67. Vayssieres, L.; Keis, K.; Hagfeldt, A.; Lindquist, S.-E. Chem. Mater. 2001, 13, 4395.
68. Jingbiao Cui and Ursula J.Gibson, J.Phys.Chem. B 2005, 109, 22074-22077.
69. Zeng, H. B.; Cui, J. B.; Cao, B. Q.; Gibson, U.; Bando, Y.; Golberg, D. Sci. Adv. Mater. 2010, 2, 336–358.
70. Izaki, M.; Watanabe, M.; Aritomo, H.; Yamaguchi, I.; Asahina, S.; Shinagawa, T.; Chigane, M.; Inaba, M.; Tasaka, A. Cryst. Growth Des. 2008, 8, 1418–1421.
71. Yu, L. G.; Zhang, G. M.; Li, S. Q.; Xi, Z. H.; Guo, D. Z. J. Cryst. Growth 2007, 299, 184–188.].
72. Yu, L. G.; Zhang, G. M.; Li, S. Q.; Xi, Z. H.; Guo, D. Z. J. Cryst. Growth 2007, 299, 184–188.
73. Konenkamp, R.; Boedecker, K.; Lux-Steiner, M. C.; Poschenrieder, M.; Zenia, F.; Levy-Clement, C.; Wagner, S. Appl. Phys. Lett. 2000, 77, 2575–2577.
74. Cui, J. B.; Soo, Y. C.; Chen, T. P.; Gibson, U. J. J. Phys. Chem. C 2008, 112, 4475–4479.
75. Cui, J. B.; Gibson, U. J. Appl. Phys. Lett. 2005, 87, 133108.
76. Zhang, D. F.; Sun, L. D.; Yin, J. L.; Yan, C. H.; Wang, R. M. J. Phys. Chem. B 2005, 109, 8786–8790.
77. Xi, Y.; Hu, C. G.; Han, X. Y.; Xiong, Y. F.; Gao, P. X.; Liu, G. B. Solid State Commun. 2007, 141, 506–509.
78. Yang, J. H.; Liu, G. M.; Lu, J.; Qiu, Y. F.; Yang, S. H. Appl. Phys. Lett. 2007, 90, 103109.
79. Vayssieres, L.; Keis, K.; Hagfeldt, A.; Lindquist, S. E. Chem. Mater. 2001, 13, 4395–4398.
80. Zhang, J.; Sun, L. D.; Liao, C. S.; Yan, C. H. Chem. Commun. 2002, 262–263.
81. She, G. W.; Zhang, X. H.; Shi, W. S.; Fan, X.; Chang, J. C. Electrochem. Commun. 2007, 9, 2784–2788.
82. Sun, Y.; Fuge, G. M.; Fox, N. A.; Riley, D. J.; Ashfold, M. N. R. Adv. Mater. 2005, 17, 2477–2481.
83. Jiang, H.; Hu, J.; Gu, F.; Li, C. J. Alloys Compd. 2009, 478, 550–553.
84. Wang, Z.; Qian, X. F.; Yin, J.; Zhu, Z. K. Langmuir 2004, 20, 3441–3448.
85. Boyle, D. S.; Govender, K.; O'Brien, P. Chem. Commun. 2002, 80–81.
86. Zhou, Z. Z.; Deng, Y. L. J. Phys. Chem. C 2009, 113, 19853– 19858.
87. Oner, M.; Norwig, J.; Meyer, W. H.; Wegner, G. Chem. Mater. 1998, 10, 460–463.
88. Taubert, A.; Kubel, C.; Martin, D. C. J. Phys. Chem. B 2003, 107, 2660– 2666.

89. Zhang, S.; Shen, Y.; Fang, H.; Xu, S.; Song, J. H.; Wang, Z. L. J. Mater. Chem. 2010, 20, 10606–10610.
90. Mo, M.; Yu, J. C.; Zhang, L. Z.; Li, S. K. A. Adv. Mater. 2005, 17, 756–760.
91. Liu, B.; Zeng, H. C. Chem. Mater. 2007, 19, 5824–5826.
92. Tang, Y. W.; Hu, X. Y.; Chen, M. J.; Luo, L. J.; Li, B. H.; Zhang, L. Electrochim. Acta 2009, 54, 2742–2747.
93. Hao, Y. Z.; Pei, J.; Wei, Y.; Cao, Y. H.; Jiao, S. H.; Zhu, F.; Li, J. J.; Xu, D. H. J. Phys. Chem. C 2010, 114, 8622–8625.
94. Wang, X. N.; Zhu, H. J.; Xu, Y. M.; Wang, H.; Tao, Y.; Hark, S.; Xiao, X. D.; Li, Q. A. ACS Nano 2010, 4, 3302–3308.
95. Sounart, T. L.; Liu, J.; Voigt, J. A.; Hsu, J. W. P.; Spoerke, E. D.; Tian, Z.; Jiang, Y. B. Adv. Funct. Mater. 2006, 16, 335–344.
96. Shi, L.; Xu, Y. M.; Hark, S. K.; Liu, Y.; Wang, S.; Peng, L. M.; Wong, K. W.; Li, Q. Nano Lett. 2007, 7, 3559–3563.
97. Plank, N. O. V.; Snaith, H. J.; Ducati, C.; Bendall, J. S.; Schmidt-Mende, L.; Welland, M. E. Nanotechnology 2008, 19, 465603.
98. Plank, N. O. V.; Howard, I.; Rao, A.; Wilson, M. W. B.; Ducati, C.; Mane, R. S.; Bendall, J. S.; Louca, R. R. M.; Greenham, N. C.; Miura, H.; Friend, R. H.; Snaith, H. J.; Welland, M. E. J. Phys. Chem. C 2009, 113, 18515–18522.
99. Tak, Y.; Yong, K. J. Phys. Chem. C 2008, 112, 74–79.
100. Wang, Z.; Qian, X. F.; Li, Y.; Yin, J.; Zhu, Z. K. J. Solid State Chem. 2005, 178, 1589–1594.
101. Panda, S. K.; Dev, A.; Chaudhuri, S. J. Phys. Chem. C 2007, 111, 5039–5043.
102. ECE730 T10 course note, Siva Sivoththaman, section 3 thin film, page 22.
103. Timothy H.Gfroerer, John Wiley & Sons Ltd, Chichester, 2000.
104. J. S. Lee, et al., J. Cryst. Growth 254, 423 (2002)
105. G Oskam, J F Long, A Natarajan and P C Searson, J. Phys. D: Appl. Phys. 31 (1998) 1927-1949. Printed in the UK.
106. Budevski E B 1983 Comprehensive Treatise of Electrochemistry vol 7, ed B E Conway et al (New York: Plenum) p 339

107. Staikov G, Budevski E, Hopfner M, Obretenov, Juttner K and Lorenz W J 1993 surf. Sci. 248 234

108. Sonnenfeld R 1986 Appl.Phys.Lett.49 1172.

109. Gao X, Hamelin A and Weaver M J 1991 Phys. Rev. Lett. 67 618.

110. Manne S, Hansma P K, Massie J, Elings V B and Gewirth A A 1991 Science 251 183

111. Magnussen O M, Hotlos J, Nichols R J, Kolb D M and Behm R J 1990 Phys. Rev. Lett. 64 2929

112. D.C. look: Mater.Sci.Eng.B80 (2001) 383; Y.Chen, D.Bagnall, and T.Yao: Mater.Sci.Eng.B 75 (2000) 190.

113. Y. Li, F. Qian, J. Xiang, and C.M.Lieber: Mater.Today 9 [10] (2006) 18.

114. H. Kind, H.Yan, B. Messer, M. Law, and P. Yang: Adv. Matter. 14 (2002) 158.

115. W. Liu, F. Xiu, K, Sun, Y.H. Xie, K.L. Wang, J.Zou, Z.Yang, and J.Liu: J. Am. Chem. Soc. 132 (2010) 2498.

116. B.Xiang, P.Wang, X. Zhang, S.A.Dayeh, D.P.R. Aplin, C. Soci, D. Yu, and D.Wang: Nano Lett. 7 (2007) 323.

117. G. Wang, S.Chu, N.Zhan, Y.Lin, L. Chernyak, and J.Liu: Appl. PhYS. Lett. 98 (2011) 041107.

118. W. Liu, F. Xiu, K, Sun, Y.H. Xie, K.L. Wang, J.Zou, Z.Yang, and J.Liu: J. Am. Chem. Soc. 132 (2010) 2498.

119. J.S.lee, S. N.Cha, J.M. Kim,H.W.Nam, S.H.Lee, W.B.Ko, K.L.Wang,J.G.Park, and J. P. Hong: Adv. Mater. 23 (2011)4183.

120. Y.W.Song,K.W. Kim, J.P.Ahn, G. E. Jang, and S.Y. Lee: Nano technology 20 92009] 275606.

121. A. Cavalho, A.Alkauskas,A. Pasquarello, A.K. Tangantsev, and N.Setter: Phys. Rev. B 80 (2009) 195205.

122. O.Volnianska, P. Boguslawki, J.Kaczkowski, P.Jackubas, A.Jezierski, and E.Kaminska:Phys.Rev.B 80 92009） 245212.

123. Sang. Hyo Lee, Jun Seok Lee, Won Bae Ko, Jung Inn Sohn, Seung Nam Cha, Jong Min Kim, Young Jun Park, and Jin Pyo Hong: Applied Physics xpress 5 (2012) 095002.

124. Y.J.Zeng, Z.Z. Ye,J.G.Lu, W.Z.Xu, L.P. Zhu, B. H. Zhao, and Sukit Limpijumnong: Applied Physics Letters 89, 042106 (2006).

125. M.A.Thomas and J.B.Cui: J. Phys.Chem. Lett. 2010,1,1090-1094.
126. Tzu-Hsuan Kao, Jui-Yuan Chen, Chung-Hua Chiu, Chun-Wei Huang, and Wen-wei Wu: Applied Physics Letters 104, 111909 (2014).
127. Zhang SB, Wei SH, Zunger A. Phys Rev B 2001, 63:075205.
128. F. A. Kroger, The Chemistry of Imperfect Crystals ~North- Holland, Amsterdam, 1964, p. 691.
129. K. I. Hagemark, J. Solid State Chem. 16, 293 ~1976.
130. E. Ziegler, A. Heinrich, H. Oppermann, and G. Stover, Phys. Status Solidi A 66, 635 ~1981.
131. V. A. Nikitenko, S. A. Stenli, and N. K. Morozova, Izv. Akad. Nauk. SSSR, Neorg. Mater. 24, 1830 ~1988.
132. J. C. Simpson and J. F. Cordaro, J. Appl. Phys. 67, 6760 ~1990.
133. R. M. de la Cruz, R. Pareja, R. Gonzalez, L. A. Boatner, and Y. Chen, Phys. Rev. B 45, 6581 ~1992.
134. D. C. Look, J. W. Hemsky, and J. R. Sizelove, Phys. Rev. Lett. 82, 2552 ~1999.
135. R. G. Gordon, AIP Conference Proceedings 394, 39 ~1997.
136. Joseph M, Tabata H, Saeki H, Ueda K, Kawai T. Physica B 2001, 302:140.
137. Bian JM, Li XM, Gao XD, Yu WD, Chen LD. Appl Phys Lett 2004, 84:541.
138. Lu JG, Ye ZZ, Zhuge F, Zeng YJ, Zhao BH, Zhu LP. Appl Phys Lett 2004, 85:3134.
139. H. Wang, S. Baek, J. Song, J. Lee, S. Lim, Nanotechnology 19 (2008) 075607
140. C. Xu, M. Kim, J. Chun, D. Kim, Appl. Phys. Lett. 86 (2005) 133107.
141. S.Y. Bae, C.W. Na, J.H. Kang, J. Park, J. Phys. Chem. B109 (2005) 2526.
142. Y.J. Li, M.Y. Lu, C.W. Wang, K.M. Li, L.J. Chen, J. Appl. Phys. Lett. 88 (2006) 143102.
143. S.Y. Li, P. Lin, C.Y. Lee, T.Y. Tseng, C.J. Huang, J. Phys. D. Appl. Phys. 37 (2004) 2274.
144. J.J. Liu, M.H. Yu, W.L. Zhou, Appl. Phys. Lett. 87 (2005) 172505.
145. L. Zhu, M. Zhi, Z. Ye, B. Zhao, Appl. Phys. Lett. 88 (2006) 113106.
146. C. Xu, J. Chun, D. Kim, J.-J. Kim, B. Chon, T. Joo, Appl. Phys. Lett. 90 (2007) 083113.
147. R.-C. Wang, C.-P. Liu, J.-L. Huang, S.-J. Chen, Appl. Phys. Lett. 88 (2006) 023111.
148. X.Y. Xue, L.M. Li, H.C. Yu, Y.J. Chen, Y.G. Wang, T.H. Wang, Appl. Phys. Lett. 89 (2006) 043118.

149. X. Qu, D. Jia, Mater. Lett. 63 (2009) 412.
150. S. Suwanboon, P. Amornpitoksuk, A. Haidoux, J.C. Tedenac, J. Alloy Compd. 462 (2008) 335.
151. S. Suwanboon, P. Amornpitoksuk, A. Haidoux, J.C. Tedenac, J. Alloy Compd. 462 (2008) 335
152. C.L. Hsu, S.J. Chang, H.C. Hung, Y.R. Lin, C.J. Huang, Y.K. Tseng, I.C. Chen, J. Electrochem. Soc. 152 (2005) G378.
153. IEEE Micro Electro Mechanical Systems Workshop,Jan-Feb 1991,Nara, Japan, p.118.
154. Yuantao Zhang, Guotong Du, Xiaotian Yang, Baijun Zhao, Yan Ma, Tianpeng Yang, H C Ong, Dali Liu and Shuren Yang, Semicond. Sci. Technol. 19 (2004) 755–758.
155. http://ecee.colorado.edu/~bart/book/eband5.htm.
156. Ajay Kushaha, Hemmen Kalita and M.Aslam, World Academy of Science, Engineering and Technology Vol: 7 2013-02-27.
157. D.C.Look, D.C.Reynolds, C.W.Litton, R.L.Jones,D.B.Eason, and G.Cantwell: Appl. Phys.Lett. 81 92002)1830.
158. D.K.Hwang, H.S.Kim,J.H.Lim,J.Y.Oh,J.H. Yang,S.J.Park,K.K.Kim, D.C.Look,and Y.S.Park: Appl.Phys.Lett.86 (2005)151917
159. H.L.Mosbacker,Y.M.Strzhemechny. and B.D. White, Appl.Phys.Lett.91(5),053512(2007); S.J. Pearton,D.P. Norton, K. Ip, Y.W.Heo, and T.Steiner, Prog.Mater. Sci.50 293 (2005).
160. I.Hussain, M.Y. Soomro,N.Bano,O.Nur, and M.Willander,J.Appl.Phys.112,064506 (2012).
161. Hussain et al.J.Appl.Phys.113, 234509 (2013).
162. Jianping Han, Mingrong Shen, Wenwu Cao, A.M. Senos and P. Q. Mnatas, Appl.Phys. let. 82, 67 (2003).